Near-field mediated Enhancement Effects on Plasmonic Nanostructures

Dissertation
zur Erlangung des Grades
Doktor der Naturwissenschaften
im Promotionsfach Chemie

am Fachbereich Chemie, Pharmazie und Geowissenschaften
der Johannes Gutenberg-Universität in Mainz

Janina Fischer

geboren in Mainz

Mainz, 2010

Die vorliegende Arbeit wurde unter der Betreuung von Prof. Dr. XXX in der Zeit von Januar 2008 bis Dezember 2010 am Max-Planck-Institut für Polymerforschung in Mainz angefertigt.

Dekan:
Erster Berichterstatter:
Zweiter Berichterstatter:

Tag der mündlichen Prüfung:

Abstract

The interaction of an electromagnetic wave with metal particles may induce an oscillation of the conduction electrons of the metal, usually referred to as plasmon. If the frequency of the incident electromagnetic wave matches the eigenfrequency of the electron oscillation, the plasmon is effectively excited and a strong optical response arises. In case of noble metal nanoparticles, the plasmon resonance typically lays in the optical range. The exact spectral position of the resonance depends on the size, shape, composition, and local dielectric environment of the nanoparticle.

When a particle plasmon is exited, the intense oscillations of the electrons may induce high local charge accumulations and, thus, strong enhancement of the electromagnetic field in the proximity of the particle. These enhanced near-fields are spatially confined close to the particle and can thus be used as strong, sub-diffraction radiation sources.
Due to these unique properties, metallic nanoparticles have been intensively studied in the past decades, especially for their application in fluorescence and Raman scattering enhancement, near field lithography, and sensing of biological probes. The nanosciences has hence become a big research area in the past decades, combining chemistry, physics, biotechnology and the material sciences.

The work presented in this thesis is focused on the design, fabrication, and characterization of novel noble metal nanostructures that offer unique optical properties. Furthermore, a detailed investigation and optimization of the enhancement of two-photon induced fluorescence of organic chromophores in proximity to plasmonic nanostructures has been realized. Such enhancement is of high significance for high resolution fluorescence microscopy and single molecule spectroscopy studies.
Two-photon excited fluorescence offers many advantages over the one-photon equivalent. The absorption transition probability P_{exc} for two-photon absorption scales to the power of 4 with the electrical field E ($P_{exc} \sim |E|^4$). Hence, the absorption process is confined to a small fraction of the focal volume and, moreover, the sensitivity is highly enhanced compared to a one-photon experiment where $P_{exc} \sim |E|^2$.
Combining this reduced focal volume resulting from the nonlinear absorption process with the localized electrical near-field of plasmonic nanostructures results in an even

stronger reduction of the excitation volume, well below the diffraction limit. This localized excitation is highly advantageous as it allows for monitoring only selected chromophores down to the single molecule level.

In this thesis, the enhancement of the two-photon induced fluorescence of organic chromophores next to plasmonic nanostructures is investigated. Using a nanosphere lithography process, a well-defined sample geometry with a high reproducability is obtained. By means of a polyelectrolyte multilayer spacer consisting of polystyrene sulfonate and poly(allylamine) hydrochloride, the dyes are placed at a defined distance from the metal surface. Covalent labeling of the top polymer layer with the dye allows for an even distribution of the dye on the sample surface and an accurate adjustment of its concentration to avoid dye aggregates. Theoretical calculations prove that the dye layer is positioned within the near-field regime of the nanostructure. An enhancement of the fluorescence signal by a factor of almost 30 for dyes in the near-field of an elliptical nanostructure compared to those dye molecules which are positioned outside the near-field regime is detected. When the plasmon resonances do not coincide with the excitation laser wavelength, no fluorescence enhancement is detected.
Elliptical particles with dimensions of 500 nm or more can be well resolved as they are bigger than the resolution limit of a standard confocal microscope. In case of these particles, double-spot fluorescence patterns at the edges can be resolved. This pattern matches the shape of the electrical near-field of elliptical nanostructures. Hence, it is assumed that this is a direct visualization of the electrical near-field.

Structures with sharp tips, such as crescent-shaped nanoparticles, are compared to roundish structures, such as ellipses. It is shown that gold crescents induce a fluorescence enhancement of 120, a fivefold higher factor than obtained for gold ellipses. This confirms that the strength of the fluorescence enhancement crucially depends on the electrical near-field of the nanostructure, as the crescents exhibit a six times stronger electrical near-field than ellipses. Hence, the higher the electrical near-field, the stronger the two-photon excited fluorescence enhancement.
Furthermore, the fluorescence enhancement depends on the material of the nanostructure. It is found that silver ellipses lead to a fluorescence enhancement factor of 45, which is a 1.5 times stronger fluorescence enhancement than obtained by identical gold particles.

The two-photon induced fluorescence enhancement is maximized at a structure-specific distance to the metal particle. For ellipses, this distance amounts to approximately 8 nm, whereas for crescent-shaped nanoparticles, the maximum fluorescence

enhancement is found at a distance of 12 nm to the metal. In close proximity to the metal, the dye underlies a strong quenching, which competes with the enhancement process, leading to a low net enhancement in all investigated structures.

This thesis also presents novel sophisticated nanostructures prepared by colloidal lithography. Stacked crescent-dimer structures with an exact vertical alignment and a separation distance of approximately 10 nm are fabricated. The polarization dependent optical properties of the nanostructures are investigated in detail and compared to single crescents. The close proximity of the individual crescents leads to a coupling process that gives rise to new optical resonances which can be described as linear superpositions of the individual crescents' plasmonic modes. A plasmon hybridization model is adapted to explain the spectral differences of all polarization dependent resonances. Theoretical calculations are performed to support the hybridization model and extend it to higher order resonances not resolved experimentally.

Opposing crescent-dimer structures in one layer are constructed by advanced nanolithography. As a modified fabrication process is applied, precise adjustment of the shape of the individual crescents is feasible. This allows for fine tuning of the plasmon resonance. Moreover, the fundamental understanding of plasmon resonances is extended, as the shape-induced shifts are correlated with the geometric data of the nanoparticles. The proposed models are supported by computer simulations.
When the individual crescents are brought in close proximity, their electrical near-fields undergo a coupling process which leads to shifted optical resonances. To assign the coupling-induced shifts, the resonances are first corrected by the shape-induced shifts. A plasmon hybridization model is adapted to explain the striking spectral differences.

List of Abbreviations

λ_{ex}	excitation wavelength
$\mathring{A}$	*Å*ngström
ν	vibronic state or frequency
τ	fluorescence correlation time
h	Planck's constant
n	refractive index
ABS	absorption
E	energy
e.g.	*exempli gratia*; for example
FCS	fluorescence correlation spectroscopy
Fig.	figure
FL	fluorescence
I	intensity
i.e.	*id est*; that is
IC	internal conversion
IX	intersystem crossing
M_W	molecular weight
N.A.	numerical aperture
NHS	*N*-hydroxysuccinimide
PAH	poly(allylamine) hydrochloride
PH	phosphorescence
PSS	polystyrene sulfonate sodium salt
Q	quenching
S	singulet
SEM	scanning electron microscope
SERS	surface enhanced Raman spectroscopy
SPR	surface plasmon resonance
T	triplet
Ti:Sa	titanium:sapphire laser
UV/vis-NIR	ultraviolet/visible-near infrared
vol. %	volume percent
wt. %	weight percent

Contents

Chapter 1

Introduction

The term *nano* derives from the old Greek word *νάννος*. Albeit literally translated it denotes a dwarf, nowadays it stands for a whole research area: the nanosciences. It is an overlapping field of chemistry, physics, material science, and even biotechnology. The main aims of nanotechnology are to produce and to understand materials with dimensions in the nanometer range (typically 0.1 – 100 nm), chemically spoken in the atomic or molecular size regime. Nanoparticles show many different properties compared to their bulk material, e.g. in their response to a plane electromagnetic light wave. Especially noble metal nanoparticles exhibit a strong response, as the free electrons in the conduction band can be excited to a collective oscillation, termed plasmon. This plasmon resonance arises when the frequency of the light coincides with the eigenfrequency of the electron oscillation. Although this phenomenon was not understood, yet in ancient times metallic particles were used to stain glasses. Probably the most famous example is the Lycurgus Cup from Roman times, which can be found in the British Museum in London. This cup appears opaque green upon reflected light, but the color turns into a translucent red when light shines through it. This impressive color change can be ascribed to the tiny amounts of colloidal gold and silver in the glass.

Figure 1: Lycurgus Cup in the British Museum in London (© Trustees of the British Museum). It appears opaque green upon reflected light and red upon transmission.

The first scientific publication on the optical properties of metal particles dates back to Michael Faraday in 1857; still, he failed to give a qualitative explanation. [1] Few years later, in 1908, the German physicist Gustav Mie succeeded in solving the Maxwell equations for the scattering of electromagnetic radiation by spherical particles. [2] This publication was the first to give a convincing explanation. The theory was extended to spheroidal particles by Richard Gans. [3] By then, the optical properties with respect to the dimensions of the particles could be explained and predicted. This was a prerequisite for tuning the plasmon resonance to any desired wavelength. Up to now, almost the whole range of the visible spectrum is experimentally covered. [4]

When a plasmon resonance is excited, a strong near-field is generated whose strength is increased by orders of magnitude over the incident electrical field. This energy confinement to the close proximity of the nanostructure can dramatically influence the properties of adjacent molecules. The first part of this thesis deals with the influence of plasmonic nanostructures on the fluorescence of nearby dye molecules. In Chapter 4, the two-photon induced fluorescence is investigated on a static system. It is shown how the autofluorescence of the metal contributes to the emission signal, and how it can be separated from the dye fluorescence. In Chapter 5, the two-photon excited fluorescence intensity at distinct separation distances to various nanostructures is investigated. Chapter 6 deals with a semi-dynamic system. Here, the linear fluorescence of dyes on plasmonic nanostructures is studied by fluorescence correlation spectroscopy.

The second part of this thesis deals with novel sophisticated nanostructures. Chapter 7 introduces stacked double crescent structures fabricated by colloidal lithography. A precise vertical alignment is achieved, resulting in quasi three-dimensional structures which could be interesting as metamaterials. A hybridization model is adapted which explains the experimental findings and the theoretical calculations.
In Chapter 8, another double crescent structure is introduced where the two crescents are aligned in plane, having the tips facing each other. By applying a novel fabrication procedure, the crescents' inherent plasmon resonances can be tuned precisely. The overlap of the electrical near-fields of the individual structures leads to denaturation of the resonances, which can be explained with the hybridization model.

Chapter 2

Theory

2.1 Optical Spectroscopy

By absorbing a photon with a certain energy E, an electron in a system with discrete energy levels can be elevated from the ground state to an excited state. [5] The energy of the photon is quantized and can only hold certain values, given by Planck's law:

$$E = h \cdot \nu, \tag{1}$$

h: Planck's constant, ν: frequency.

Thus, the electron is excited exactly by such an amount of energy, usually resulting in an excited vibrational level of a higher electronic state. One reason is that the density of states is clearly higher for elevated vibronic levels than for the particular vibronic ground state. [6] The transition probability of the electron depends on the electric transition dipole (Fermi's golden rule) :

$$\Gamma_{i\to f} = \frac{dP(t)}{dt} = \frac{\pi}{2\hbar} \left| \vec{E}_0 \, \langle \psi_f | \, \vec{\hat{\mu}} \, | \psi_i \rangle \right|^2 \rho_f^{\epsilon}(\bar{\epsilon}_f), \tag{2}$$

$\Gamma_{i\to f}$: transition rate between the states i and f,
P(t): transition probability,
$\vec{E}_0$: amplitude of the electromagnetic field of light,
$\langle \psi_f | \, \vec{\hat{\mu}} \, | \psi_i \rangle$: overlap integrals,
$\rho_f^{\epsilon}(\bar{\epsilon}_f)$: density of states in terms of the mean energy (photonic mode density).

In a first approximation, the electric transition dipole is determined by the overlap integrals and the specific transition dipole of the involved electronic states. Fermi's golden rule features the square of the transition dipole; thus, the squares of the overlap integrals, usually referred to as Franck-Condon factors[i], are necessary likewise to obtain the transition probability. They represent the relative transition probability between two electronic states. A graphic representation allows for a qualitative estimation of

[i] named after the German-American physicist James Franck and the American physicist Edward Condon

the Franck-Condon factors (Fig. 2).

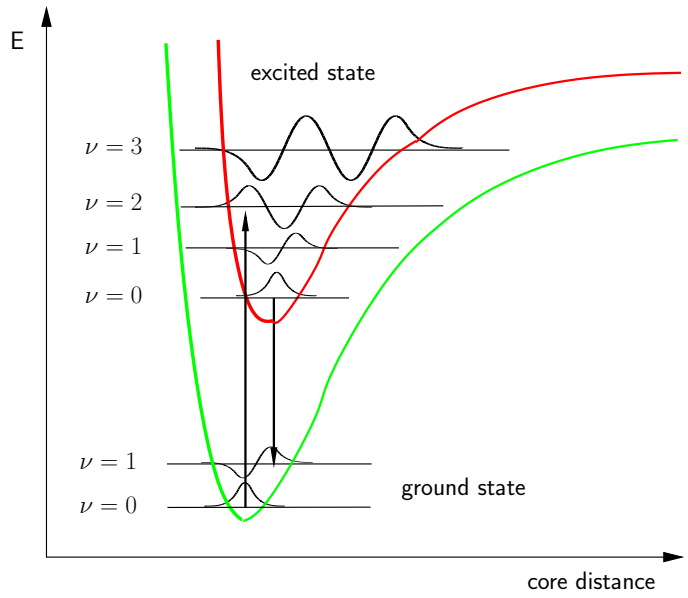

Figure 2: Lennard-Jones potential curves of the ground and the excited state.

Generally, the potential of the excited state is shifted to higher core distances, as this state usually features a more antibinding character. Due to the Boltzmann distribution, the absorption processes normally begin from the vibronic ground state of the electronic ground state. The overlap integrals should be as big as possible to make a transition possible. This is the case if the amplitudes of the vibrational state functions show a high overlap and have the same algebraic sign over the whole integration area. Thus, it becomes apparent why usually an excited vibronic level of the higher electronic state is reached after the absorption of a photon: here the Franck-Condon factors are maximized (Fig. 2). [6,7]

2.1.1 Jablonski diagram

An excited electron can return to the electronic ground state along different paths. All options have distinct time scales resulting in different probabilities. To discuss the diverse relaxation processes it is convenient to employ the so-called Jablonski diagram[ii] (Fig. 3). [7]

In the scheme, the electronic ground state S_0, and three excited states, S_1, S_2,

[ii] named after the Polish physicist Alexander Jablonski

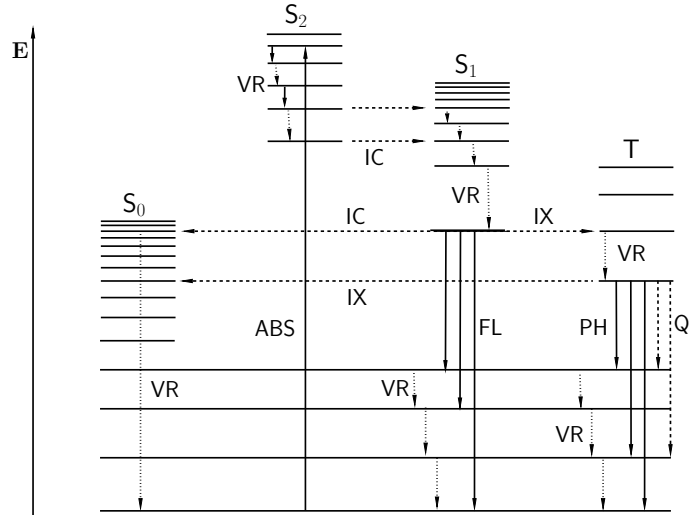

Figure 3: Jablonski diagram.

and T are depicted.[iii] After the electron has been excited, two competing processes are possible: vibrational relaxation (VR), and internal conversion (IC). Vibrational relaxation is a non-radiative transition to a lower vibronic state of the same electronic level. The released energy is transferred to the environment, e.g. as kinetic energy to the solvent. Internal conversion denotes an isoenergetic, thus radiationless transition to an electronic state with the same multiplicity. Both processes show rate constants between 10^{11} s^{-1} and 10^{13} s^{-1}. Hence, it depends on the substance which of the processes dominates.

Once the vibronic ground state ν_n of any excited state is reached, besides internal conversion, two rivaling processes exist: fluorescence (FL), and intersystem crossing (IX). Fluorescence is the transition to an energetically lower electronic state of equal multiplicity. During this process energy is released as light. Intersystem crossing is an isoenergetic, radiationless transition between states with different multiplicities. For fluorescence and intersystem crossing the rate constants lie between 10^7 s^{-1} and 10^{10} s^{-1}. However, as the transitions between states of distinct multiplicities are symmetry-forbidden, they are more unlikely.

Radiative transitions to energetically lower states with different multiplicity are termed phosphorescence (PH). The relatively low rate constants for these transitions (usually 10^{-1} s^{-1} to 10^4 s^{-1}) can be explained by the fact that the process is quantum mechanically forbidden as it requires spin inversion. Due to the spin-orbit coup-

[iii] It is common to denote singlet states (total spin=0, multiplicity=1) with a capital S, and triplet states (total spin=1, multiplicity=3) with a capital T.

ling, however, it is weakly allowed. Hence, the phosphorescence processes occur with marginal probability.

As a result of the high lifetime of the triplet state, often non-radiative quenching processes occur. Molecules in the surrounding usually act as quenchers, e.g. molecular oxygen. The quencher absorbs the energy of the excited molecules, e.g. via kinetic energy transfer by collision. The excited quencher itself returns to the ground state via non-radiative processes. [6,7]

$$ {}^3X + Q \rightarrow {}^1X + Q^* \underset{-E}{\longrightarrow} {}^1X + Q, \tag{3} $$

^3X: substance X in its triplet state,
^1X: substance X in its singlet state,
Q: quencher molecule,
Q^*: excited quencher molecule.

Usually the fluorescence is shifted to higher wavelengths compared to the absorption (Stokes shift). As the fluorescence mainly originates from the vibronic ground state of the excited state (Kasha rule), it is obvious that after the absorption, energy must have been released by means of radiationless relaxation processes. As a result, less energy is emitted than had been absorbed, visible in the redshift of the emission wavelength compared to the absorption maximum (Fig. 4).

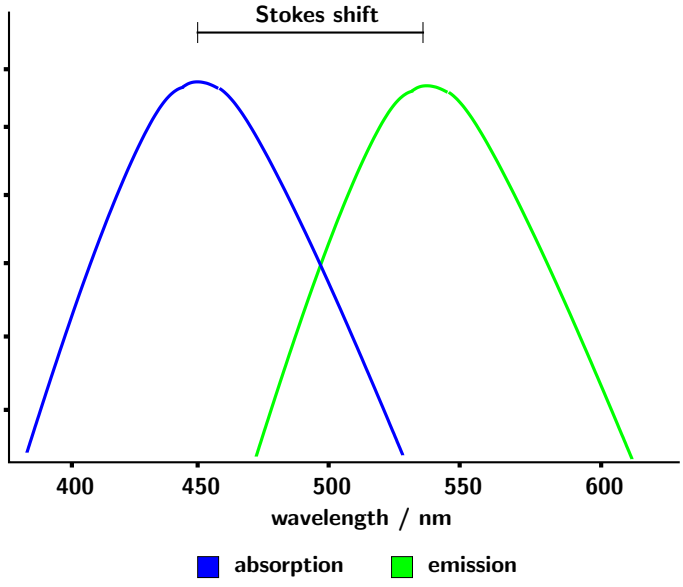

Figure 4: Schematic illustration of the Stokes shift.

2.1.2 Two-photon excitation

In a one-photon process, a single photon elevates the fluorophore to the excited state. However, an electron can also be excited by simultaneous absorption of two or more photons. Though already predicted by Maria Göppert-Mayer in 1931 [8,9], it could only be verified experimentally thirty years later [10]. Multiphoton microscopy was introduced in 1990 [11] and has become a widespread tool especially for cell imaging (for details of two-photon excitation microscopy see Chapter 3.6.1). [12–14]

Usually, two-photon excitation is achieved using long wavelength excitation sources. Hence, two photons are necessary to reach the same energy level as accomplished by one-photon absorption at a lower wavelength.[iv] Fig. 5 is a schematic Jablonski diagram for one- and two-photon excitation.

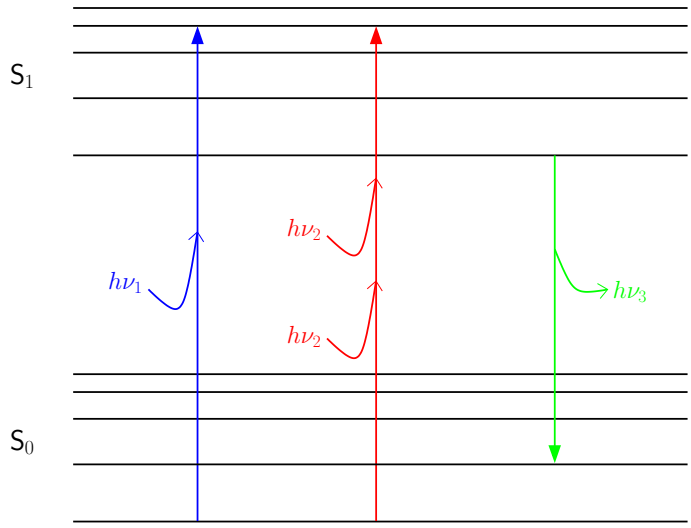

Figure 5: Jablonski diagram for one- and two-photon excitation.

On the left, a one-photon process is depicted. The energy of the photon matches the size of the energy gap and the electron can thus be elevated to the excited state. The right part of the scheme shows a two-photon process. Here, two photons are necessary for excitation, because one single photon does not deliver sufficient energy to overcome the energy gap.[v]

Some selection rules for optical transitions are different for one- and two-photon ab-

[iv] Theoretically, the two photons can have different energies if their sum fits the resonance condition. In practice, usually only one excitation source is used and, therefore, the two photons possess the same energy.

[v] It should be noted that the photons are not absorbed sequentially by means of an intermediate state.

sorption. [15] Therefore, the excited electron is elevated to different electronic states. As the fluorophores emit from the same excited state, namely the vibrational ground state of the first excited state (see Chapter 2.1.1), the emission process is mainly identical for one- and two-photon induced fluorescence.

Multiphoton excitation in general is a nonlinear process, which is a favorable property for optical imaging. In a one-photon process, the absorbed light in any plane of the excitation beam path is proportional to the incident intensity. As the total amount of light which passes the sample does not change, the emission intensity is constant at all positions in the beam path (Fig. 6 upper part). Using a confocal pinhole eliminates the background signals, nevertheless, bleaching takes place along the whole beam path. In contrast, the amount of absorbed light in a two-photon process shows a quadratic dependence on the incident intensity. As focusing the beam increases its intensity, in this case the amount of absorbed light is highest at the focal plane (Fig. 6 lower part). [16] This leads to strongly localized excitation, which is advantageous as to reduced photobleaching and less background fluorescence and scattering signals. Although the two-photon absorption does not readily exhibit an improved resolution[vi], the excitation confinement to the focal plane offers the big benefit of a real spatial selectivity. This is an essential prerequisite for systematic distance-dependent studies of the fluorescence intensity.

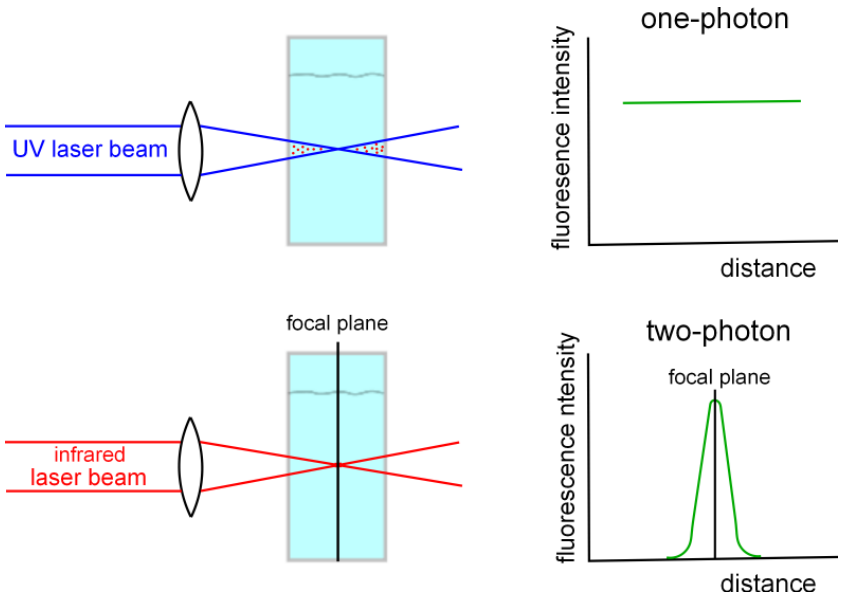

Figure 6: Schematic comparison of one- and two-photon excitation.

[vi]The resolution is the shortest distance between two objects that can still be distinguished. It is proportional to the wavelength λ. Hence, for high wavelengths, the shortest resolvable distance between two points increases.

2.2 Metal Optics – The Drude model

The optical properties of metals strongly differ from those of non-conductors. While dielectrics usually appear transparent and reflect light weakly, metals are highly absorbing and reflect light at visible and infrared wavelengths. A simple model to explain the optical characteristics of metals was established by Drude. It is based on the kinetic gas theory and treats electrons as a gas of independent, point-like charges. The electrons move freely until they suffer an instantaneous scattering process. The probability for a collision per time unit is given by $1/\tau$, with τ being the electron relaxation time (also known as mean free time). Each collision causes a complete loss of directional information and an abrupt change in velocity. Under the influence of an external field, Newton's laws apply. Thus, the electrons are accelerated in between the collisions, resulting in a drift motion. [17–19]

This surprisingly simple model leads to astonishing good results to predict many properties of real metals, inter alia the optical properties of metals described by the dielectric wavefunction $\epsilon(\omega)$. Applying the Drude model, the dielectric function under the influence of a harmonic field with the frequency ω results as

$$\epsilon(\omega) = 1 - \frac{\omega_p^2}{\omega^2 + i \cdot \frac{\omega}{\tau}}, \tag{4}$$

with the plasma frequency ω_p:

$$\omega_p = \sqrt{\frac{n_e \cdot e^2}{\epsilon_0 \cdot m_e}}$$

,

n_e: electron density,	ϵ_0: permittivity in vacuum,
e: electron charge,	m_e: effective electron mass.

Equation (4) implies that the optical properties of a metal are given by the plasma frequency ω_p and the relaxation time τ.

2.3 Metal Nanostructures

Metallic structures with dimensions in the range of the wavelength of light or below may support optical resonances. [20] The research area investigating the optical properties of metal nanoparticles is a rapidly growing field. [4,20] It has been termed *plasmonics*, due

to the so-called plasmon resonances of metal nanoparticles. A plasmon is a collective oscillation of the free electrons in a metal. This oscillation can be excited by an incident electromagnetic wave. If the frequency of the light matches the eigenfrequency of the electron oscillation, a strong optical response arises. For noble metals, the resonance wavelengths lie in the visible regime of the spectrum and can directly be observed.

To understand these striking optical phenomena of nanoparticles upon incident light, a theoretical description is necessary. Generally, light can interact with a particle in two different ways: either it is scattered or absorbed by the particle. The amounts of scattered and absorbed light, I_{sca} and I_{abs}, respectively, depend on the particular cross-sections C_{sca} and C_{abs} in the following way:

$$I_{sca} = \frac{I_0}{A} \cdot C_{sca}, \tag{5a}$$

$$I_{abs} = \frac{I_0}{A} \cdot C_{abs}, \tag{5b}$$

with the incident light intensity I_0, and the illuminated area A. The sum of I_{sca} and I_{abs} is also denoted as extinction.

2.3.1 Quasi-static Approximation – Rayleigh theory

The first calculations of the optical properties of particles were performed by Lord Rayleigh. He used a quasi-static model – a crude approximation that the electromagnetic phase is constant throughout the whole particle. This only holds for particles much smaller than the wavelength of the incident light. However, for particles with diameters up to 40 nm this is a reasonable simplification which yields good results by using simple electrostatic descriptions. [21,22] To derive definitions for the scattering and absorption cross-sections, some considerations on the polarizability α of the particle have to be made. In the following, the underlying idea and the basic steps are presented. Further details can be found in literature. [23]

In the solid state, the polarization of a lattice atom is influenced by adjacent atoms. Thus, the electric polarization does not only depend on the external field, but also on an additional field induced by the polarization of the neighbor atoms. Hence, an individual atom experiences a local field $\vec{E}_{loc}$ which consists of three contributions:

$$\vec{E}_{loc} = \vec{E}_{ext} + \vec{E}_{int} + \vec{E}_{Lorentz}, \tag{6}$$

namely the external electric field, $\vec{E}_{ext}$, the internal electric field, $\vec{E}_{int}$, and the so-called Lorentz field, $\vec{E}_{Lorentz}$. The internal electric field arises due to electrostatic interactions between adjacent atoms and depends on the crystal structure. For simplification, a cubic structure is assumed where all individual dipole moments of the atoms are arranged in the direction of the external field. In this case, it can be shown that the individual contributions cancel out and, thus, $\vec{E}_{int} = 0$. [23–25]

The Lorentz field is the contribution due to the polarizations of the vicinal atoms. For the calculation of $\vec{E}_{Lorentz}$, a spherical volume around a single atom is considered (Fig. 7). The dipoles outside this volume shall be arranged continuously. This induces charges on the surface of the imaginary sphere, which lead to an effective electric field at the regarded atom.

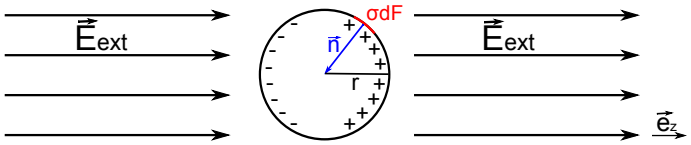

Figure 7: Quasi-static model for particle plasmons.

The parallel polarization $\vec{P}$ caused by the external field creates the following surface charge density on the surface of the spherical volume:

$$\sigma = \vec{P} \cdot \vec{n} = -P \cdot \cos(\theta), \tag{7}$$

$\vec{n}$: normal vector of the surface element pointing to the center,
θ : angle between the surface element and the direction of the external field.

In a small part of the surface dF the charge q equals σdF, and its electric field is given by Coulomb's law:

$$E = \frac{q}{4\pi\,\epsilon_0\,r^2} = \frac{\sigma dF}{4\pi\,\epsilon_0\,r^2}, \tag{8}$$

r: radius of the spherical volume.

Thus, the part in direction of the external field is

$$\vec{E} = \frac{\sigma dF}{4\pi\,\epsilon_0\,r^2} \cdot \cos(\theta) \cdot \vec{e}_z, \tag{9}$$

with the unit vector $\vec{e}_z$ in direction of the external electric field $\vec{E}_{ext}$.

Integrating around the whole surface and using Equation (7) leads to a definition for $\vec{E}_{Lorentz}$:

$$\vec{E}_{Lorentz} = \frac{1}{3\,\epsilon_0} \cdot P \cdot \vec{e}_z. \tag{10}$$

With

$$\vec{P} = N \cdot \alpha \cdot \vec{E}_{Lorentz}, \tag{11}$$

N: number of dipoles per volume,

and sundry rearrangements one obtains the following definition for α :

$$\alpha = 3\,\epsilon_0\, V \cdot \frac{\epsilon_r - 1}{\epsilon_r + 2}\,, \tag{12}$$

ϵ_r: dielectric function relative to the medium,

V: volume.

Equation (12) is also known as Clausius-Mossotti relation.

The scattering and absorption cross-sections are then given by:

$$C_{sca} = \frac{k^4}{6\pi} \cdot 3\,V^2 \cdot \frac{(\epsilon_r' - 1)^2 + \epsilon_r''^2}{(2 + \epsilon_r\prime)^2 + \epsilon_r''^2}, \tag{13a}$$

$$C_{abs} = 3\,kV \cdot \frac{3\epsilon_r''}{(2 + \epsilon_r\prime)^2 + \epsilon_r''^2}, \tag{13b}$$

with the wavenumber k.

2.3.2 Mie theory

For bigger particles, the quasi-static approximation is not reasonable as the electric field in the particle cannot be regarded constant any longer. Thus, retardation effects take place, which cause separation of charges in the particle. As the speed of light is finite, the electromagnetic field in the particle differs locally. Consequently, the oscillation of the electrons in big particles are phase shifted between front and back. This lowers the energy and becomes apparent in a redshift of the resonance. Together with the reduced field due to the limited penetration depth of light into metal, the redshift increases with the particle size. [19]

An analytical calculation of the optical response of spherical particles was done by Gustav Mie. [2] Although simultaneously developed by Debye [26] in another context, Mie was the first to apply the theory to understand the optical properties of metal particles.

Mie calculated the optical response by solving Maxwell's equations [27] in polar coordinates. Thus, he obtained corrected scattering and absorption cross-sections, and a definition for the polarizability that includes the retardation effects. [23] However, the Mie theory can only be applied to spherical particles. In 1912, Richard Gans extended the theory to spheroidal particles by introducing a geometrical factor in the definition for the polarizability α. [3]

2.3.3 Surface enhanced luminescence

When a plasmon resonance is excited, the electrical near-field is strongly enhanced and spatially confined. The presence of the electrical near-field can have a dramatic effect on both the excitation and emission of molecules placed in this region. [20,28,29] One well-known surface enhanced process is the surface enhanced Raman scattering (SERS). [30,31] During the past decades it has become an ultrasensitive spectroscopic technique with single molecule sensitivity. [32,33] The fluorescence of a dye can also be altered by the presence of a metal nanostructure. Early publications describe an enhanced fluorescence of dyes on metal islands. [34–36]

Although discovered decades ago, the mechanisms of surface enhanced processes have not been understood for a long time. This can be mainly ascribed to the undefined geometries employed in early studies. Modern experimental techniques, such as electron beam lithography, atomic force microscopy, confocal microscopy, and other recent advances in nanotechnology allow for defined sample geometry design. Nowadays, the model explained by Barnes is widely accepted as explanation for surface enhanced processes. [28] In the following, this model will be adapted to surface enhanced fluorescence, as this is the key process investigated in this thesis.

As elaborated in Chapter 2.1, the probability of emission is given by Fermi's golden rule (Equation (2)). Assuming the simple case of one single emitter close to a metal interface, the interface can influence the transition rate as it can modify two parameters: the matrix elements determined by the wavefunctions of the respective electronic states, $\langle\psi_f|\,\vec{\tilde{\mu}}\,|\psi_i\rangle$, and the photonic mode density $\rho_f^{\epsilon}(\bar{\epsilon}_f)$, that is the density of states

of the excited state f in terms of the mean energy.[vii]
The matrix elements can be influenced by an interface at distances characteristic for the wavefunctions, i.e. approximately 1 Å. Thus, if the emitter and an atom of the interface are nearest neighbors, the wavefunction of the emitter can be perturbed. The photonic mode density, however, is modified at distances in the dimension of the wavelength of light. [28] The basic mechanism can be understood if one considers an emitter close to a plane interface. The electric field of the emitted light is reflected by the interface and thus interferes with the emitter. Depending on the distance between the emitter and the interface, the reflected light is either in phase or out of phase with the original field. This leads to an oscillating fluorescence signal, which has been experimentally proven by Drexhage et al. [37,38]

Due to this effect, surface enhanced luminescence may occur. The explanation reveals the reason why it is a substance-specific effect: as the photonic mode density differs for various substances, the effect of a nearby interface is different for each species.

2.3.4 Surface induced quenching mechanisms

In literature, a quenching of the fluorescence of a dye very close to a metal interface has been described. This quenching can occur due to different reasons and, thus, follows distinct mechanisms.

For very small distances, i.e. a few Ångström, the molecular orbitals of the dye can overlap with the d-bands of the metal and, thus, the excited electron can experience a radiationless transition, using the energy levels of the metal.
For bigger separations of the dye and the interface, this quenching mechanism is negligible as the effective orbital-band overlap is insufficient for larger distances. Here, non-radiative de-excitation rates are important. Every fluorophore has an intrinsic non-radiative de-excition rate Γ_{nr}^{i} due to its intramolecular relaxation pathways (e.g. internal conversion from S_1 to a high vibronic level of S_0 followed by vibrational relaxation to the vibronic ground state of S_0). Furthermore, the interface is able to introduce additional non-radiative decay channels, e.g. direct energy transfer. Hence, the fluorophore also experiences an electromagnetic non-radiative de-excitation rate Γ_{nr}^{em}. Due to these two factors, the radiative fraction of the de-excitation is diminished. Thus, the

[vii] In literature definitions using the frequency-dependent photonic mode density is also common. As energy and frequency are proportional, the qualitative outcome is identical.

detectable fraction of the de-excitation can be expressed as:

$$\Gamma_{de-exc}^{det} = \frac{\Gamma_r}{\Gamma_r + \Gamma_{nr}}\,, \tag{14}$$

Γ_r: total radiative de-excitation rates of the molecule,

Γ_{nr}: total non-radiative de-excitation rates of the molecule.

Including the fluorescence excitation rate Γ_{exc} and the detection efficiency η, the total detectable fluorescence intensity emitted by a single molecule can be described by Equation (15).[viii]

$$I = \Gamma_{exc} \cdot \eta \cdot \frac{\Gamma_r}{\Gamma_r + \Gamma_{nr}}\,. \tag{15}$$

2.4 Fluorescence Correlation Spectroscopy

Fluorescence correlation spectroscopy was developed in the 1970s by Elson and Madge. [39–41] They adapted the theory of dynamic light scattering to fluorescent probes. Hence, in FCS the temporal fluctuations of the fluorescence signal are measured and analyzed.

Fig. 8 shows the conceptual basis of FCS. The fluorescent species diffuse in and out of the observation volume of a confocal microscope. This causes fluctuations of the fluorescence signal.

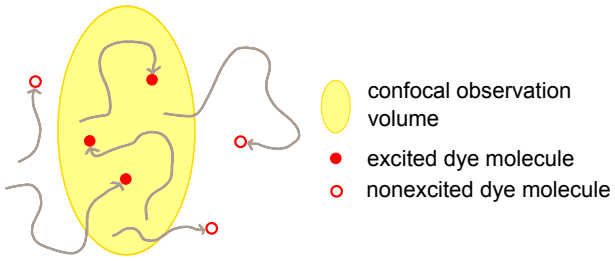

Figure 8: Fluorescent molecules moving in and out of the focal volume causing fluorescence fluctuations.

A schematic signal is depicted in Fig. 9 a. The close-up shows an exemplary fluorescence fluctuation pulse. The duration of the pulse contains information about the

[viii] This equation neglects the effect of triplet blinking.

time a fluorescent particle needs to cross the observation volume. A possible motion of the particle corresponding to the time trace is illustrated in Fig. 9 b.

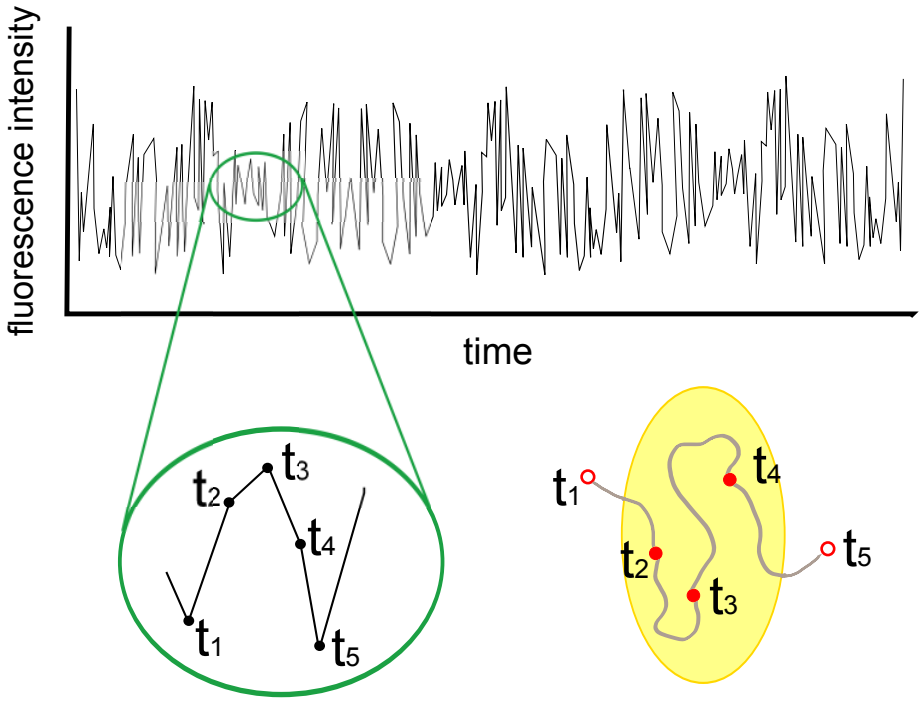

Figure 9: a. Exemplary fluorescence time trace with close-up. b. Corresponding motion of the fluorescent species.

The data obtained from FCS experiments are analyzed by the normalized autocorrelation function $G(\tau)$:

$$G(\tau) = \frac{\langle \delta I(t) \cdot \delta(I(t+\tau) \rangle}{\langle I(t) \rangle^2}, \tag{16}$$

with the time t at which the signal is recorded, the lag time τ, the fluorescence intensity $I(t)$, and its fluctuations $\delta I(t)$. The angular brackets indicate the time average over the fluorescence signal.

It has been shown theoretically that for an ensemble of m freely diffusing fluorescent species, $G(\tau)$ has the following analytical form:

$$G(\tau) = 1 + \frac{f_T}{1 - f_T} \frac{1}{N} \sum_{i=1}^{m} \frac{f_i}{[1 + \frac{1}{\tau_{D_i}}] \sqrt{1 + \frac{t}{S^2 \tau_{D_i}}}}, \tag{17}$$

where N is the average number of fluorescent species in the observation volume,

f_T the fraction of the triplet state with the decay time τ_T, f_i is the fraction of the component i with the diffusion time τ_{D_i}, and S is the structural paramater, which is given by the axial and the radial dimensions of the confocal volume, z_0 and r_0, respectively, by the equation $S = z_0/r_0$.

In general, autocorrelation is the cross-correlation of a signal with itself. Hence, it reveals the self-similarity as a function of the time span. For small time spans, the datapoints are correlated with each other, whereas for bigger time spans, it is more unlikely that the signal is correlated to the signal time t_0 (Fig. 10).

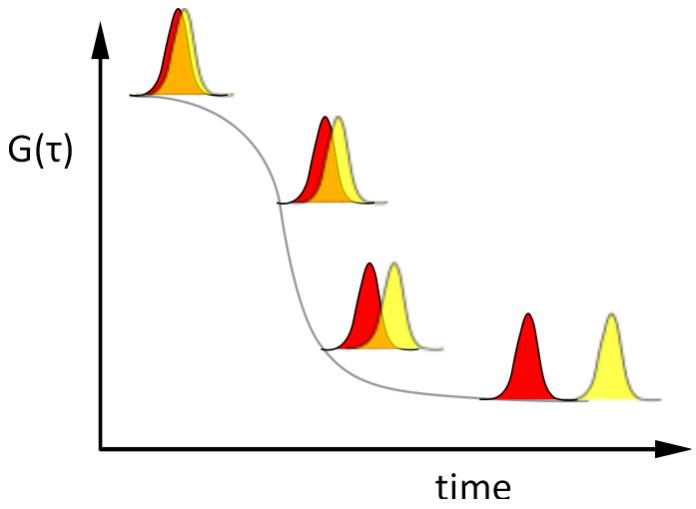

Figure 10: Schematic explanation of the autocorrelation method.

As the fluctuations arise from physical processes, a variety of physical data can be obtained from an FCS experiment. The diffusion coefficient, for example, is a typical constant gained from FCS. It is related to the diffusion time τ_D. The longer the correlations persists, the slower the diffusion. Fig. 11 shows autocorrelation curves for three different fluorescent particles with specific diffusion times.

It can directly be seen from the graphic representation that species 1 with the correlation time τ_1 exhibits the fastest diffusion, and species 3 the slowest.

Other physical data extracted from FCS measurements are the hydrodynamic radius, the number of fluorescent species in the confocal volume and, hence, the concentration, or the brightness of single molecules, amongst others.

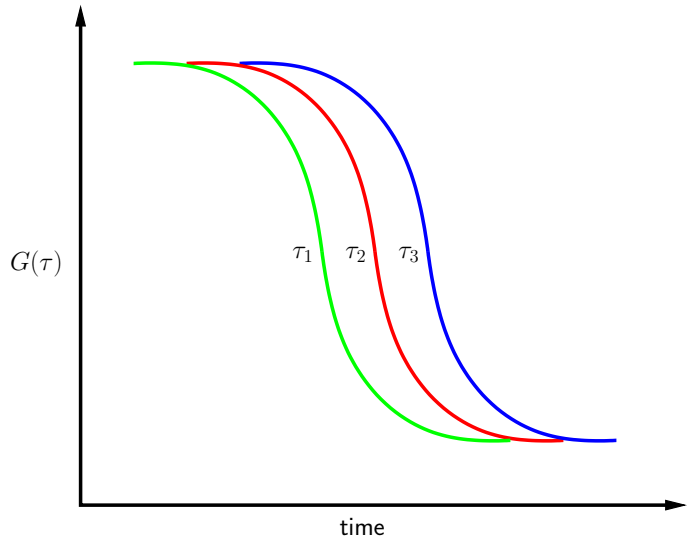

Figure 11: Autocorrelation curves for three different species with specific diffusion times.

Chapter 3

Materials & Methods

3.1 Nanostructure Fabrication by Colloidal Lithography

3.1.1 Ellipses and Disks

Elliptical gold and silver nanoparticles were prepared according to a nanosphere lithographic process similar to the method for nanodisk fabrication described by Hanarp et. al. [42] Glass coverslips (25 mm diameter, Menzel Gläser, Braunschweig, Germany) were cleaned with a 2 vol. % detergent solution (Hellmanex® II, Hellma GmbH & Co. KG, Mühlheim, Germany) in an ultrasonic bath for 20 minutes twice. The samples were thoroughly rinsed with ultrapure water and dried in a nitrogen stream followed by a treatment with oxygen plasma (300 mW, 5 minutes; Plasmacleaner 200-G, Technics Plasma GmbH, Kirchheim, Germany). A 2 nm chromium and a 40 nm gold or silver layer, respectively, were evaporated on the glass substrate (Auto 306, Edwards, Sussex, United Kingdom). After the metal deposition, the substrates were directly immersed in a 3 mM solution of 3-mercapto propionic acid for one hour. Subsequently, the samples were rinsed with ultrapure water and a suspension of polystyrene nanospheres (Polystyrene Nanobeads: NIST, Polysciences, Warrington, USA; the original suspension was diluted 1:100 in ethanol) with the desired diameter were randomly dispersed on the surface via spincoating (1500 rpm, Headway Research, Inc., Garland, USA). The samples were etched with an argon ion beam (RR-I SQ76, Roth & Rau, Wüstenbrand, Hohenstein-Ernstthal, Germany), having the surface normal tilted by 65° relative to the ion source during the exposure for fabrication of ellipses, or perpendicular to the surface normal for the disks. After the etching process, the colloidal mask was removed mechanically with an adhesive tape (Scotch® Magic™ Tape 810: 19 mm × 33 m, 3M, Neuss, Germany). The fabrication process is depicted in Fig. 12.

3.1.2 Crescent-shaped Nanoparticles

Gold crescent-shaped nanoparticles were prepared following a procedure described by Shumaker-Parry et al. [43] After cleaning with the detergent solution (Hellmanex® II,

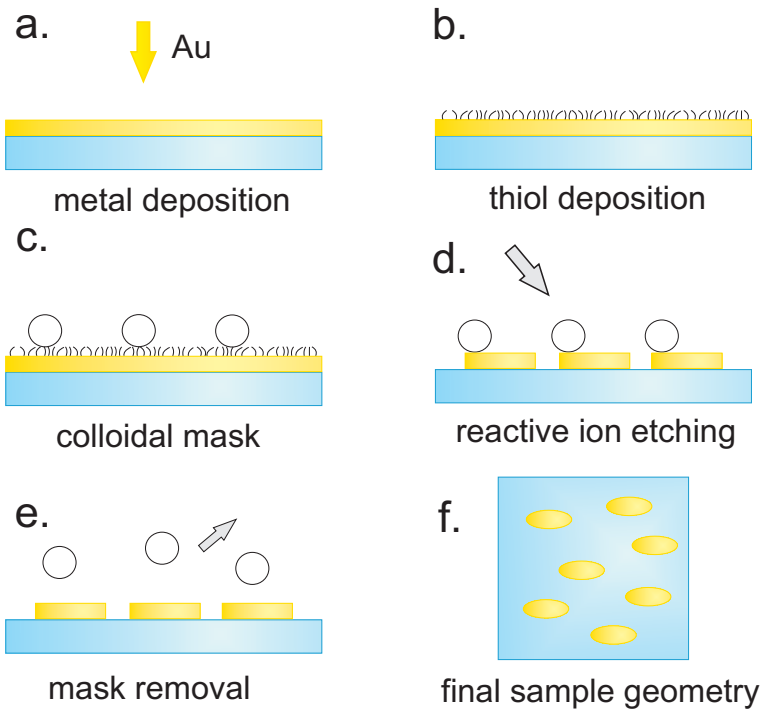

Figure 12: Schematic illustration of the fabrication of elliptical nanostructures.

Hellma GmbH & Co. KG, Mühlheim, Germany) and oxygen plasma (300 mW, 5 minutes; Plasmacleaner 200-G, Technics Plasma GmbH, Kirchheim, Germany), polystyrene nanospheres (Polystyrene Nanobeads: NIST, Polysciences, Warrington, USA; 100 nm in diameter; the original suspension was diluted 1:1,000 in ethanol) were deposited onto the glass coverslips by drop-coating. Subsequently, 0.5 nm chromium and 40 nm gold were evaporated on the substrate (Auto 306, Edwards, Sussex, United Kingdom), having the surface normal tilted by an angle of 30° relative to the metal source. Reactive ion beam etching perpendicular to the surface was performed (RR-I SQ76, Roth & Rau, Wüstenbrand, Hohenstein-Ernstthal, Germany), using argon as etching gas. The colloidal mask was removed by means of an adhesive tape (Scotch® Magic™ Tape 810: 19 mm × 33 m, 3M, Neuss, France).

3.1.3 Stacked Double Crescents

Glass slides (Objektträger, approximately 20 × 25 mm, Menzel Gläser, Braunschweig, Germany) were cleaned with a 2 vol. % detergent solution (Hellmanex® II, Hellma GmbH & Co. KG, Mühlheim, Germany) in an ultrasonic bath for 15 minutes twice, followed by ultrasonication with ultrapure water and ethanol. 50 µL of a 0.001 wt. % ethanolic suspension of polystyrene colloids with a diameter of 400 nm were deposited

onto the glass substrates by drop-coating.[ix] The solvent was evaporated with a gentle nitrogen stream, resulting in a surface coverage of approximately 0.15 objects/µm^2. Subsequently, a 1.5 nm chromium and a 25 nm gold layer were evaporated under an angle of 30° of the surface normal with regard to the metal source (Balzers PLS500, evaporation rate 0.03 nm/s). Afterwards, the sample was rotated by 180°, and 20 nm silicon dioxide (Balzers PLS500, evaporation of silicon monoxide at a rate of 0.1 nm/s with an oxygen partial pressure of $1 \cdot 10^{-4}$ mbar to form silicon dioxide at the sample surface), 1.5 nm chromium and 25 nm gold were deposited under an angle of -30°. The samples were etched with a reactive ion beam, using a gas mixture of argon and CF_4 (RR-I SQ76, Roth & Rau, Wüstenbrand, Hohenstein-Ernstthal, Germany). The colloidal mask was removed with rubber glue (Fixogum, Marabu GmbH & Co. KG, Tamm, Germany) that was applied onto the sample surface, hardened for twelve hours at room temperature and then removed mechanically. Fig. 13 illustrates the experimental procedure.

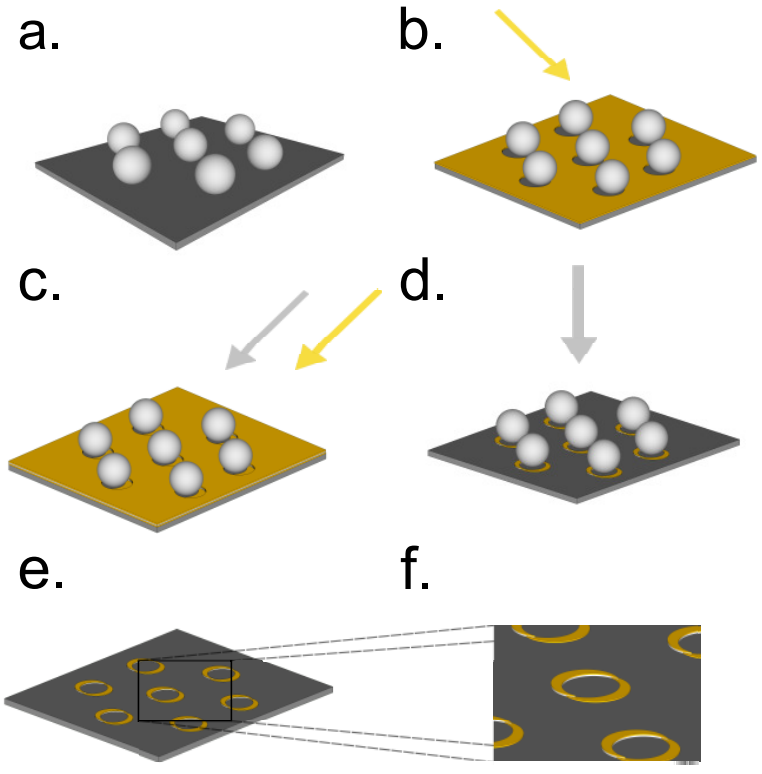

Figure 13: Fabrication scheme for stacked double crescent structures.

[ix] The colloids were prepared by surfactant free emulsion polymerization of styrene with acrylic acid as co-monomer (2.5 wt. % with respect to styrene). The synthesis was carried out by XXX.

3.1.4 Arrays of Stacked Double Crescents

The double and single crescent structures were also produced in highly ordered two-dimensional arrays.[x] Therefore, a hexagonally close-packed monolayer of polystyrene colloids with a diameter of 550 nm[xi] was assembled on a glass substrate by a process described by Retsch et al. [44] The sample was subjected to oxygen plasma (10 sccm flow rate, 50 W power; Femto, Diener Electronic GmbH & Co. KG, Ebhausen, Germany), and etched for 13 minutes, leading to uniform shrinking of the colloids and, thus, forming a non-close-packed monolayer with size-reduced colloids of 400 nm. Using this substrate as mask for the patterning process, large areas of highly ordered stacked double crescents can be obtained. The total lateral extension of the array is determined by the colloidal monolayer, accomplishing several square centimeters.

3.1.5 Rings

Gold rings were fabricated analogously to the procedure applied for the double crescents described in Chapter 3.1.3, only leaving out the separating silicon dioxide layer before depositing of the second metal layer under the -30° angle.
In detail, 50 µL of a 0.001 wt. % ethanolic suspension of polystyrene colloids with a diameter of 400 nm were dropped onto clean glass slides (Objektträger, approximately 20 × 25 mm, Menzel Gläser, Braunschweig, Germany). The solvent was evaporated with a gentle nitrogen stream. Subsequently, a 1.5 nm chromium and a 25 nm gold layer were evaporated under an angle of 30° with regard to the metal source. Afterwards, the sample was rotated by 180°, and 1.5 nm chromium and 25 nm gold were deposited under an angle of -30°. The samples were etched with a reactive ion beam process, using a gas mixture of argon and CF_4. The colloidal mask was removed with an adhesive tape (Scotch® Magic™ Tape 810: 19 mm × 33 m, 3M, France).

3.1.6 Opposing Double Crescents

Glass slides (Objektträger, approximately 20 × 25 mm, 1 mm thick, Menzel Gläser, Braunschweig, Germany) were cleaned with a 2 vol. % detergent solution (Hellmanex® II, Hellma GmbH & Co. KG, Mühlheim, Germany) in an ultrasonic bath for 20 minutes

[x] This procedure was experimentally realized by XXX.
[xi] The colloids were prepared by surfactant free emulsion polymerization of styrene with acrylic acid as co-monomer (2.5 wt. % with respect to styrene). The synthesis was carried out by XXX.

twice. The samples were thoroughly rinsed with ultrapure water and dried in a nitrogen stream. Polystyrene nanospheres, 400 nm in diameter, were randomly dispersed on the substrate by drop-coating.[xii] The solvent was evaporated with a gentle nitrogen stream. An 80 nm gold layer was evaporated on the glass substrate (Auto 306, Edwards, Sussex, United Kingdom), the surface normal perpendicular to the metal source. The samples were etched with an argon ion beam (RR-I SQ76, Roth & Rau, Wüstenbrand, Hohenstein-Ernstthal, Germany), having the surface normal tilted by different angles between 45° and 65° relative to the ion source during the exposure. The etching process was performed in two steps: in the first step, 40 nm of the gold layer were etched away, then the sample was rotated by 180°, and the remaining 40 nm of the gold layer were exposed to the ion beam. This yields the two opposing crescent structures. After the etching process, the colloidal mask was removed mechanically with an adhesive tape (Scotch® Magic™ Tape 810: 19 mm × 33 m, 3M, Neuss, France). Fig. 14 shows a sketch of the sample fabrication.

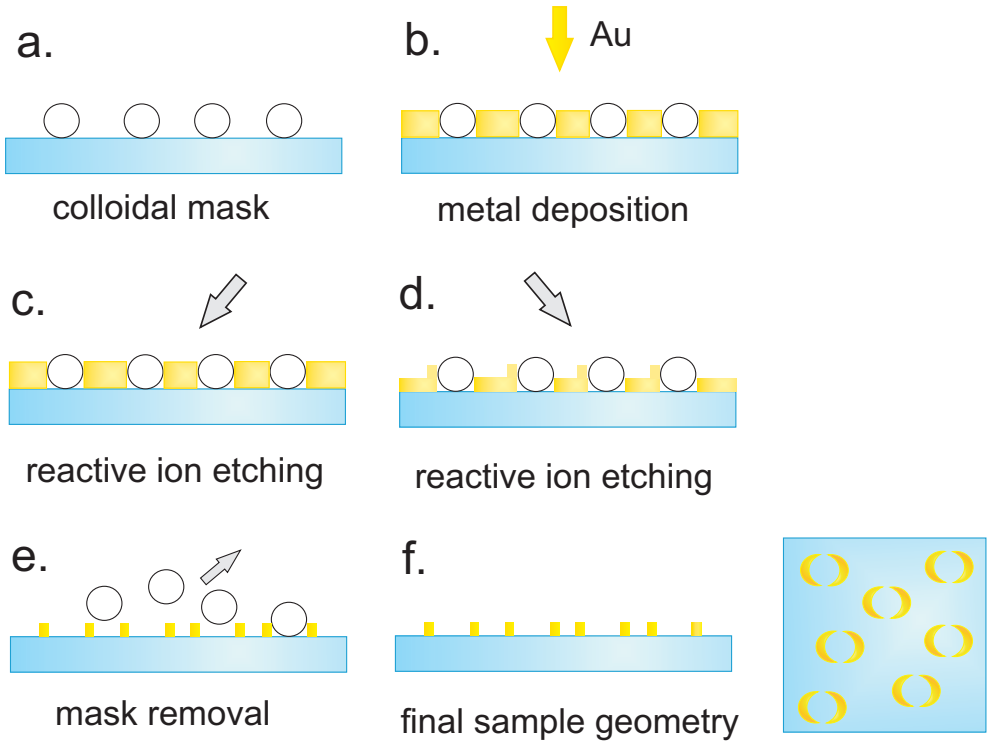

Figure 14: Fabrication scheme for opposing double crescent structures.

[xii] The colloids were prepared by surfactant free emulsion polymerization of styrene with acrylic acid as co-monomer (2.5 wt. % with respect to styrene). The synthesis was carried out by XXX.

3.2 Dye-Labeling of the polymer spacer

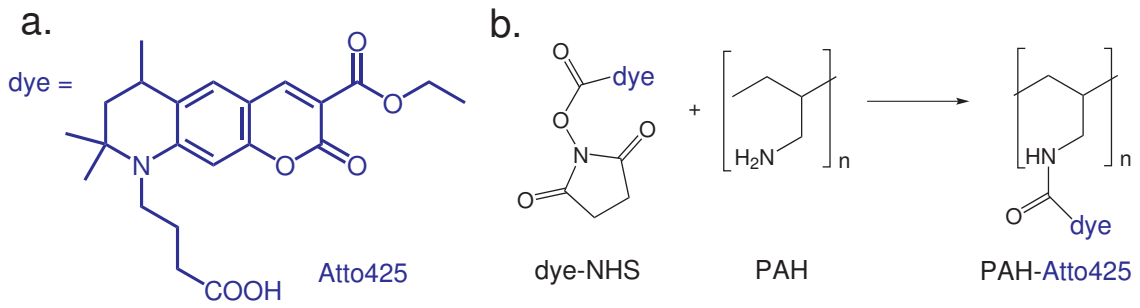

Figure 15: a. Structure of the dye Atto425. b. General reaction equation for a dye-NHS ester with the polymer spacer poly(allylamine) hydrochloride (PAH).

Batch:	196 mg	poly(allylamine) hydrochloride (PAH)
	1 mg	Atto425
	0.21 g	$NaHCO_3$
	50 mL	water
	10.1 mL	dimethylformamide
	400 mL	acetone

The PAH is diluted in 32 mL of a 50 mM solution of $NaHCO_3$ in water. The dye is completely dissolved in 100 mL of DMF. 25 µL of this stock solution are diluted with 10 mL DMF to yield a final concentration of $5.02 \cdot 10^{-5}$ mol/L. This solution is added dropwise to the PAH-solution. The mixture is stirred in the dark at room temperature for one hour. Subsequently, the reaction mixture is poured dropwise under continuous stirring to 400 mL acetone. The precipitated polymer is washed and dried in high vacuum.

This procedure gives rise to the statistical ratio of functionalized amino groups to free amino groups in the PAH of 1:10,000. This dye concentration should avoid aggregation effects.

Yield: 155 mg (80 % of theory), yellow powder

3.3 Nanostructure Functionalization

Silanization

The sample slides were treated with 3-aminopropyl(triethoxy)silane (Alfa Aesar, Karlsruhe, Germany) via a gaseous phase deposition. Therefore, the glass slides were put in a closed glass container together with a small vial containing a few drops of 3-aminopropyl(triethoxy)silane. The container was then heated for three hours at 120 °C. The silane serves as linker for the following polyelectrolyte spacer attachment.

Polyelectrolyte attachment

After rinsing with ultrapure water, alternating polyelectrolyte layers were deposited on the samples via dip-coating according to the method of Decher et al. [45] This process makes use of the electrostatic attraction forces between polycations and polyanions. In this thesis, poly(allylamine) hydrochloride (PAH, Sigma Aldrich, M_W=15 kDa) and polystyrene sulfonate sodium salt (PSS, Sigma Aldrich, M_W=70 kDa) were employed as polycation and polyanion, respectively. The polymers were dissolved in aqueous saline solutions to enhance the ionic strength of the solutions, and, moreover, to enforce enlongation and straightening of the polymer chains in order to form a flat surface coverage. The final concentrations were 0.02 M for the polyelectrolytes (in monomer units), 0.5 M $MnCl_2$ (PSS solution) and 2 M NaBr (PAH solution). The samples were immersed alternatingly for 20 minutes in the particular solution, starting with PSS. After each step, the samples were rinsed with ultrapure water. Before deposition of the last PAH layer, the polymer was functionalized with the ester-activated fluorophore Atto425 (Atto425-NHS ester, Attotec, Germany), following the reaction scheme given in Chapter 3.2. Once the desired number of bilayers was reached, the samples were dried in a nitrogen stream.

3.4 Standard Sample Characterization Methods

The scanning electron microscope images were recorded on a LEO instrument, Gemini 1520.

Polarization-dependent UV-visible-NIR spectra of nanostructure ensembles were recorded on a Perkin Elmer Lambda 900 spectrometer.

Surface plasmon resonance spectroscopy experiments were carried out on a self-built setup. [46]

Atomic force microscopy was done on a JPK Nanowizard instrument.

3.5 Data Processing and Computer Simulations

The confocal microscope images were exported as tif files with the Zeiss software LSM Image Browser (version 4.2.0.121). Further image processing was done with Igor Pro (version 5.0.2.0) and ImageJ (version 1.40g). The analysis of the intensities was performed with Igor Pro (version 5.0.2.0), and Matlab (version 7.5.0.342, R2007b), using self-written procedures.

The computer simulations[xiii] were executed using the commercial package JCMwave which is based on a finite element method. [47] The software was operated with Matlab (version 7.5.0.342, R2007b), which constructs the geometry, calls the solver and performs the post processing. Three-dimensional finite element simulations were performed, and a perfectly matched layer method was used to truncate the simulation domain. Tetrahedral adaptive meshes were applied to discretize the computational domain, and second order interpolation functions were used on elements. The refractive index of the glass substrate was always set to 1.5. The permittivity of gold was taken from the Drude model [23], fitted to the data of Johnson and Christy. [48]

3.6 Confocal Microscopy

In a fluorescence microscope, the excitation light is effectively separated by the fluorescent light by means of optical filters and dichroic mirrors. In a confocal microscope, the exciting laser beam is focused in the object plane. Additionally, a confocal pinhole is placed in the intermediate image plane. Hence, only light from the focal volume can pass the pinhole and reaches the detector. Fig. 16 shows a sheme of a confocal fluorescence microscope.[xiv]

In this thesis, all microscope images were recorded on a commercial confocal laser scanning microscope (Zeiss, Göttingen, Germany) consisting of the module LSM 510 and an inverted microscope model Axiovert 200. [49] In all experiments, a water immersion objective (C-Apochromat 40/1.2 W Corr., N.A. 1.2, working distance 0.29 mm, Zeiss, Göttingen, Germany) was employed. The samples were mounted in an Attofluor cell chamber.

[xiii] The computational simulations presented in this thesis were carried out by XXX and XXX. See according chapters for further specification.

[xiv] The image is taken from a Zeiss product brochure. It can be found on the company's website www.zeiss.de.

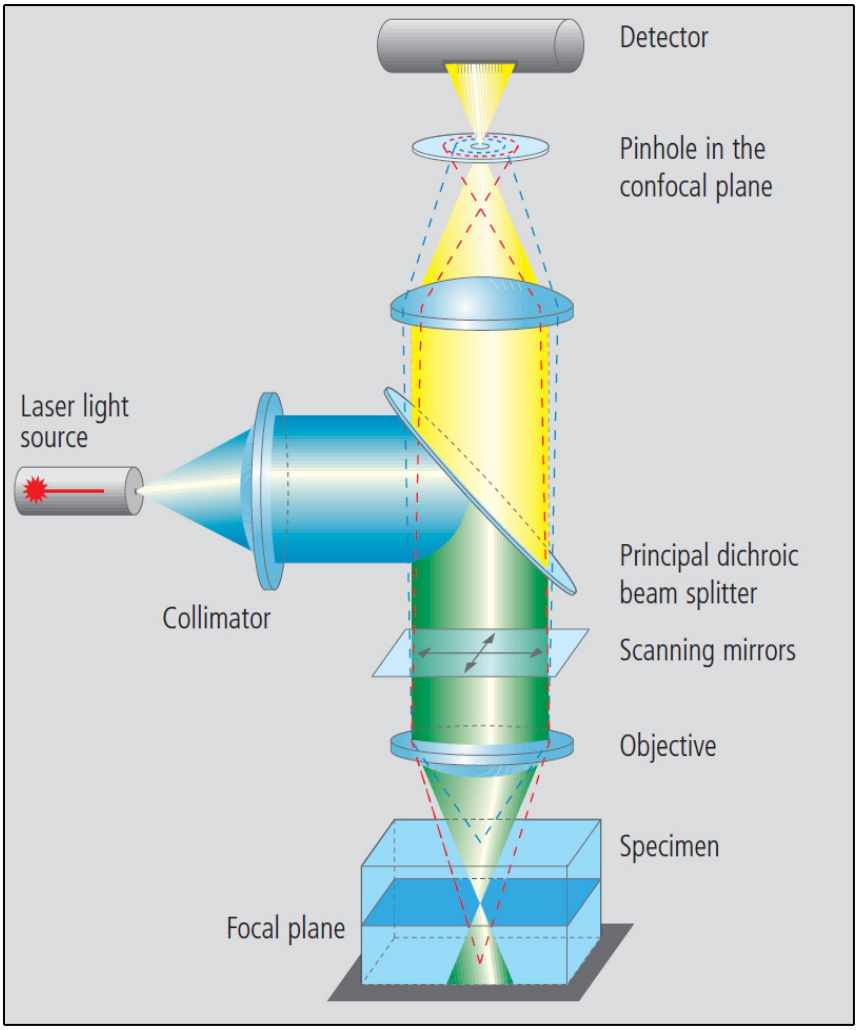

Figure 16: Schematic illustration of an inverted confocal microscope for light and fluorescence microscopy.[xiv]

The reflectivity images were obtained using the strongly attenuated (0.1 %[xv]) 488 nm line of an Argon laser (Lasos Lasertechnik GmbH, Jena, Germany). A neutral density filter NT 80/20 and a short-pass filter KP 635 were employed as main dichroic beam splitter and emission filter, respectively, letting the reflected laser line go through. The pinhole was set to 90 µm (1 Airy unit). The scan speed was 1.60 µs/pixel.
The linear fluorescence images were obtained using the 458 nm line of the same Argon laser, after attenuation to 30 %. A main dichroic beam splitter HFT 458 and a long-pass LP 475 emission filter were employed. The pinhole was set to 72 µm (1 Airy unit).

[xv] As the relative change in the laser intensity can be determined with much higher accuracy than the absolute light intensity at the surface, only relative units (%) are stated in this thesis and used for further analysis. [50]

The scan speed was 1.60 µs/pixel.
The two-photon excited fluorescence images were obtained using a titanium:sapphire laser (pulsed femtosecond Ti:Sa laser, λ_{ex}=790 nm, repetition rate 80 MHz, MaiTai, Spectra-Physics, Berlin, Germany), attenuated to 1 % (this corresponds to an average power of 1 mW on the sample surface). A main dichroic beam splitter-short pass filter HFT-KP 700/543 and a band pass emission filter BP 435-485 IR were employed. The pinhole was fully opened (1000 µm). The scan speed was 1.60 µs/pixel.

3.6.1 Two-photon excitation

Two-photon microscopy was experimentally realized by Denk et al. While he worked in the group of Watt Webb, one of the pioneers of fluorescence correlation spectroscopy, he combined two-photon absorption and common laser scanning. This technology was patented by Denk, Strickler, and Webb. [11,51]

The use of an infrared laser, producing a high photon density, allows for a two-photon absorption process. As described in Chapter 2.1.2, multiphoton excitation is restricted to a small volume. Due to this localization, the confocal pinhole becomes useless and it is usually omitted in a multiphoton microscopy setup.

3.7 Fluorescence Correlation Spectroscopy

Fluorescence correlation spectroscopy (FCS) is nowadays almost solely performed on a confocal microscopy setup. A dilute fluorescent sample is illuminated with a focused laser beam. The fluorophores passing the focal volume are excited and emit light. This emitted light is collected by the objective; subsequently it passes the dichroic mirror, the emission filter, and the confocal pinhole before it reaches the detector (Fig. 16).
The combination of focused excitation and confocal detection results in an ellipsoidal observation volume with the main axes r and z, depicted in Fig. 17. With typical dimensions of r=0.25 µm and z=2 µm, extremely small detection volumes in the femtoliter range are yielded. When a molecule enters the focal volume, it starts to fluoresce. The characteristic timescales of the fluorophores are analyzed, e.g. how long the molecules reside in the observation volume. These data give valuable hints for physical constants such as the diffusion coefficient (details can be found in Chapter 2.4).

Since the early 1990s, a number of technical advances have been adopted to FCS, including confocal optics, high efficiency avalanche photodiode detectors, and stable

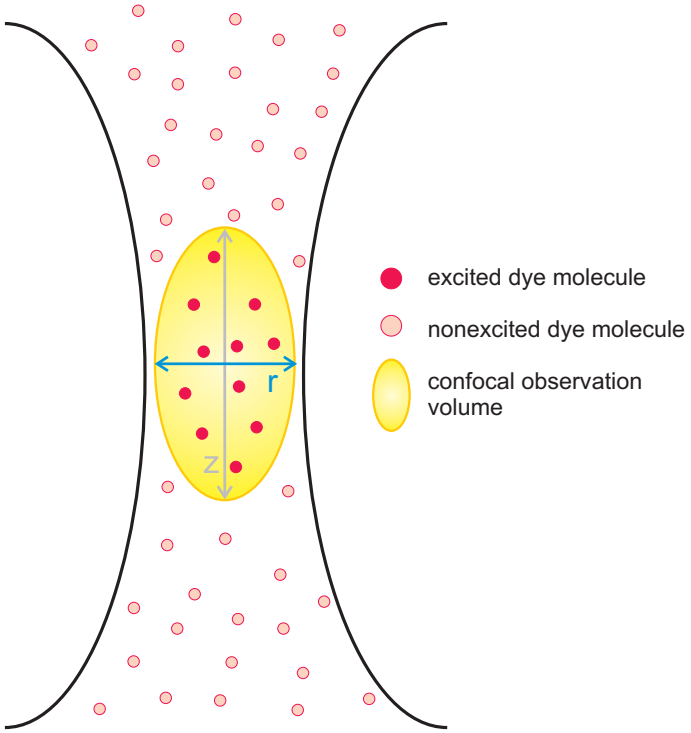

Figure 17: Scheme of the focal volume in fluorescence correlation spectroscopy. The dye molecules inside the ellipsoidal observation volume are excited.

lasers. [16] As a result, the number of applications of FCS has rapidly increased. Nowadays, it is a powerful standard method with high spatial resolution to investigate the diffusion of fluorescent species.

All measurements presented in this thesis were performed on an extended commercial FCS setup (Olympus, Hamburg, Germany) consisting of the module Fluoview™ FV300, an inverted microscope model Olympus IX70, equipped with a PicoQuant FCS extension consisting of a picosecond pulsed laser unit, an avalanche photo diode detector unit, and a fast aquisition card. A water immersion objective (UPLSAPO 60×W, N.A. 1.2, working distance 0.28 mm, Olympus, Hamburg, Germany) was employed. Both confocal laser scanning microscopy and FCS detection are available on the setup, using the same optical port. The FCS measurements were performed with a 468 nm pulsed diode laser, attenuated to approximately 20 %. A main dichroic beam splitter DM 570 and a long pass LP 505 emission filter were employed. The samples were mounted in an Attofluor® cell chamber. All correlations and lifetime corrections were executed with the PicoQuant software SymPhoTime® (version 5.1.2.0).

Chapter 4

Two-photon induced Fluorescence Enhancement on Plasmonic Nanostructures

4.1 Introduction

Fluorescence microscopy is a popular technique for imaging, for example of biological samples. To achieve a high resolution at short exposure times, high emission intensities and high signal-to-noise ratios are required. An elegant method to achieve high intensities from sub-diffraction volumes with low background is the fluorescence enhancement by noble metal nanostructures. The enhancement effect was demonstrated under one-photon excitation for a number of systems. Early publications report on an enhanced fluorescence intensity of dyes placed close to noble metal islands. [34–36] In recent years, structures with higher field enhancements have been investigated with optical near-field microscopy. Kramer et al. observed an enhancement of the fluorescence for a dye probed with a gold tip. [52] Nakamura et al. showed that gold nanospheres can enhance the fluorescence of the dye Rose Bengal, depending on their size. [53] Zhu et al. reported an enhanced fluorescence from Rhodamine B mixed with gold colloids under ultraviolet irradiation. [54] Great efforts have been made recently to obtain a quantitative description of these enhancement effects. Therefore, defined measurements with simple geometries as spheres were performed. Schneider et al. reported on a distance-dependent quenching of fluorescence by gold nanoparticles [55] and Anger et al. demonstrated the continuous transition from fluorescence enhancement to quenching as a function of the distance between the dye and a gold nanoparticle [56].

A two-photon excited fluorescence offers many advantages over the one-photon equivalent. The absorption transition probability P_{exc} for two-photon absorption scales quadratically with the incident intensity and, thus, it scales to the power of 4 with the electrical field E ($P_{exc} \sim |E|^4$). Hence, the absorption process is confined to a small fraction of the focal volume and, moreover, the sensitivity, namely the increase of detectable signal from the region of interest of the nonlinear measurement, is highly enhanced compared to an equivalent one-photon experiment where $P_{exc} \sim |E|^2$.
The fluorescence enhancement effect on metal nanoparticles has also been shown for two-photon induced fluorescence. Very early, Glass et al. observed a 150-fold en-

hancement of the fluorescence intensity from Rhodamine B adsorbed on silver metal islands compared to molecules in solution. [57] Cohanoschi et al. demonstrated a 480-fold enhancement of the dye Hoechst 33258 in aqueous solution containing gold colloids. [58] More recently, studies on more defined systems have been carried out by Tovmachenko et al., such as metal-core particles coated with spacer molecules and fluorescent dyes. [59]

Improving the approach of a defined geometry described by Tovmachenko et al., using more complex structures in a two-photon approach should allow for investigations on structures with much stronger electrical near-fields. The remaining challenges are to place a good two-photon active chromophore in optimal concentration in a defined position relative to the metal. The concentration should be as high as possible but low enough to avoid the formation of dye aggregates, which usually leads to reduced fluorescence lifetimes. [60–63] Moreover, it is of great importance to distinguish between the fluorescence signal of the dye and luminescence of other sources such as autoluminescence of the metal structure.

In this chapter, a high local enhancement of two-photon induced fluorescence by elliptic gold nanostructures is presented. Using a nanosphere lithography process, a well-defined geometry is obtained. By means of polyelectrolyte multilayers, dyes are placed at a defined distance from the metal surface. Covalent labeling of the top polymer layer with the dye allows for an even distribution of the dye on the sample surface and an accurate adjustment of its concentration to avoid dye aggregates. Additionally, this sample design guarantees a high reproducibility.

4.2 Results and Discussion

Gold elliptic nanostructures with average lateral dimensions of approximately 180 nm $\times$ 245 nm were prepared and investigated (Fig. 18).[xvi] A polymer spacer of 40 nm thickness defines the distance to the dye, which is covalently bound to the top layer (inset in Fig. 18). This chemical binding inhibits any diffusion of the dye in the polymer matrix. Due to the low concentration of the dye, the formation of aggregates is hindered, and an even distribution of the dye on the surface is established.

The decay length of the electrical near-field of the elliptic nanostructure is found by finite element simulations to be $\sim$ 50 nm. Hence, the dye is placed within the near-

[xvi] All scanning electron microscopy images shown in this chapter were taken by Marcus Schmelzeisen.

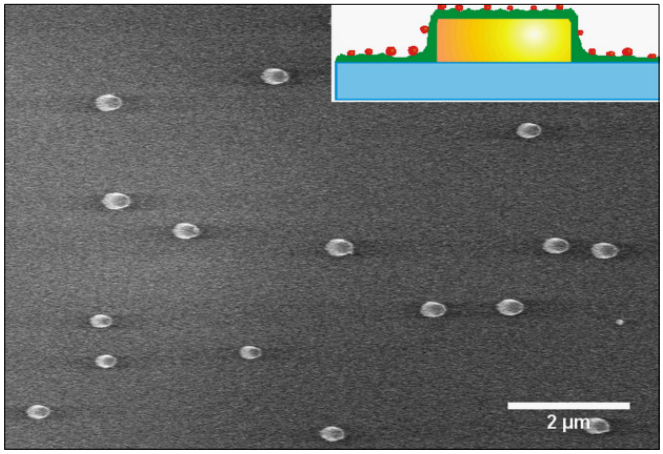

Figure 18: Scanning electron microscope image of bare gold ellipses. The inset shows a sketch of the sample geometry: the gold nanostructure (yellow) on top of a glass slide (blue) is covered with a silane and PSS/PAH-bilayers (green). The top layer is functionalized with the dye Atto425 (red).

field regime of the metal nanostructure. Fig. 19 shows the simulation of the scattering near-field of a gold ellipsis (Johnson Christy data [48]) with the dimensions 94 nm × 131 nm and a thickness of 30 nm on a glass substrate (n = 1.5).[xvii]

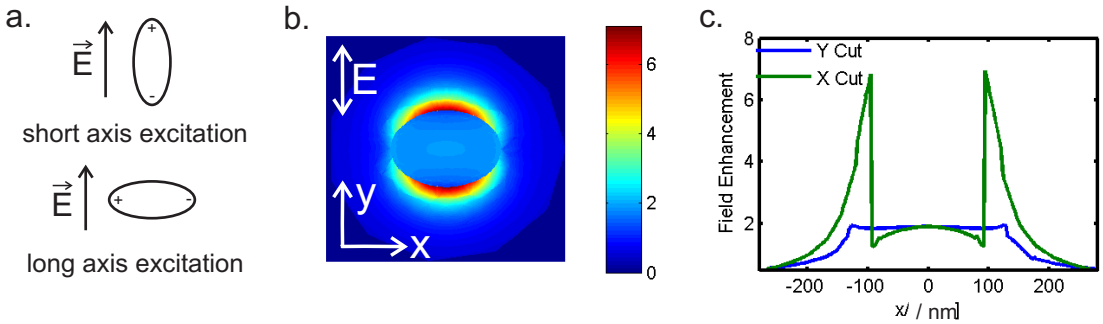

Figure 19: a. Simulation of the scattered near-field $|E|$ of a gold ellipsis, z-cut through particle center, relative to the incident field. b. cuts through x=0 and y=0, z-cut through particle center.

Elliptic nanostructures exhibit two plasmon resonances upon irradiation, corresponding to the excitation of the short and the long axes of the ellipses. They can be measured with UV/vis spectroscopy (Fig. 20). The bare gold structure shows resonances at 720 nm and 1080 nm, respectively. After coating with polyelectrolyte multilayers, maxima at 800 nm and 1300 nm can be identified.
As this structure occupies these two polarization-dependent resonances, it can be switched on and off by selective excitation using linear polarization of the incident laser light, an

[xvii] All theoretical calculations shown in this chapter were implemented by XXX.

essential feature for systematic measurements.

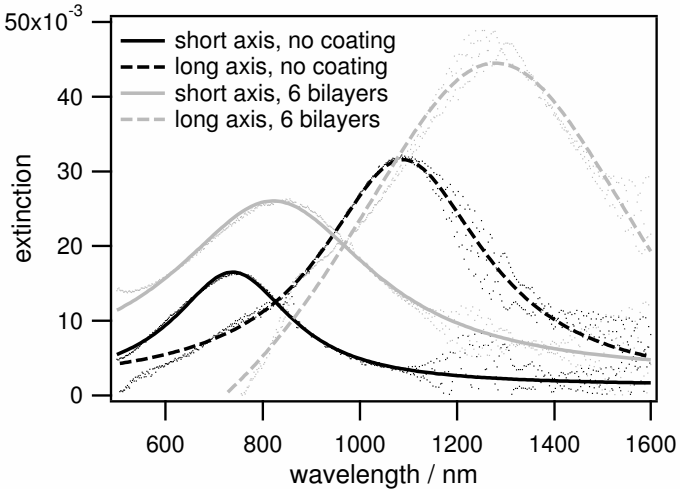

Figure 20: Extinction of gold ellipses before and after deposition of polyelectrolyte bilayers recorded with light polarized along the short (solid line) and the long axes (dashed line of the ellipses), respectively. The black curves show the extinction spectra of bare ellipses, the gray ones after coating with six polyelectrolyte bilayers. The curves are fitted with Lorentz functions.

4.2.1 Excitation of the short axes of 180 nm nanostructures

Fig. 21 shows the reflectivity (a.), the linear fluorescence (b.), the nonlinear fluorescence (c.) of the dye-covered sample and the signal of the gold structure without dye (d.). The light was polarized along the short axes of the ellipses in all images. Fig. 21 a., b. and c. show the same spot on the sample surface, whereas Fig. 21 d. was recorded before dye deposition and, thus, represents a different area of the sample. The data were taken from areas that have not been scanned before with the Ti:Sa laser to avoid any possible bleaching effects. Twenty different individuals were investigated, and the precision of the obtained mean values was determined by statistical analysis.
The ellipses' exact positions were determined with the reflectivity image. Afterwards, one- and two-photon induced fluorescence images were recorded of the same sector of the sample. The nanostructure quenches the linear fluorescence (Fig. 21 b.). A rough estimation yields a quenching of approximately 30 % on the nanostructure compared to the signal far away of the gold, that is, the linear excited fluorescence intensity is 30 % lower on the gold than on the glass. In two-photon excitation bright spots appear (Fig. 21 c.), although emission is quenched by the gold in a similar way as for linear excitation. Thus, the two-photon absorption process must be strongly enhanced, compensating the quenching and leading to a strong net enhancement. The little shifts

between the pictures a. and b. compared to c. of Fig. 21 are ascribed to the slight misalignment of the two different laser beams.
Additionally, an autoluminescence signal of the gold ellipses before dye coating is observed (Fig. 21 d.). The effect of linear photoluminescence of metals was first observed and discussed by Mooradian [64], later also multiphoton-induced luminescence spectra were described in literature, e.g. for surfaces [65] and for metal nanostructures [66]. It is widely accepted that at high intensities, detectable two-photon induced luminescence in the metal takes place. [67,68]

This gold autofluorescence overlays the measured signal in the experiments with the dye-covered substrates. For better visualization of the dye-induced part of the fluorescence signal, the beginning of the color scales in Fig. 21 c. and d. are set close to the average fluorescence intensity of the gold autoluminescence. Fig. 21 c. shows uniform bright spots of the dye fluorescence, whereas the spots Fig. 21 d. are less intense.
Before the calculation of the fluorescence enhancement factor and the correction of the measured fluorescence intensities are presented, a proof for the described two-photon process is shown in the following section.

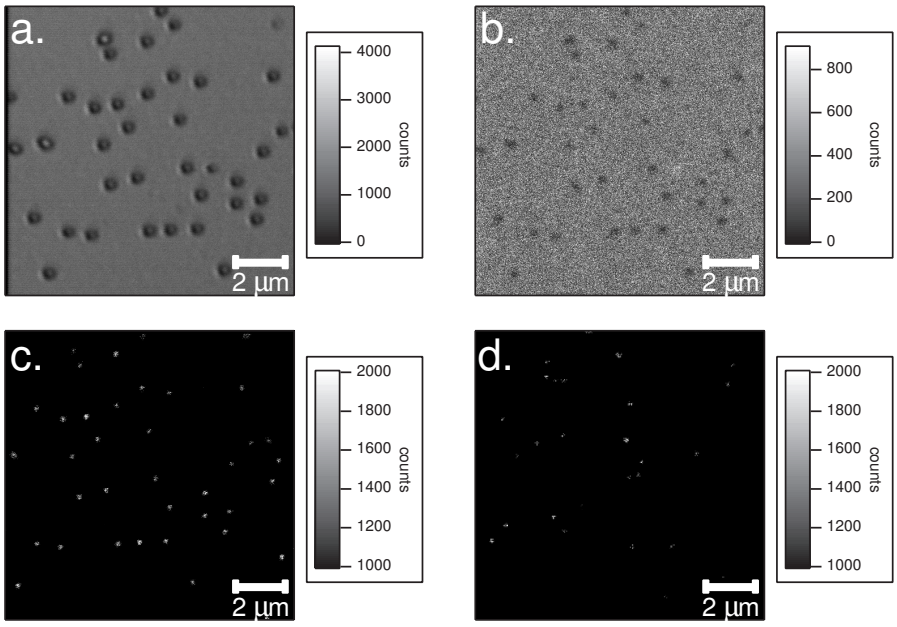

Figure 21: 180 nm gold ellipses: short axes: a. Reflectivity at λ_{ex}=488 nm, b. linear fluorescence at λ_{ex}=458 nm, and c. two-photon induced fluorescence at λ_{ex}=790 nm of one spot on the sample. d. Autoluminescence signal of the gold at λ_{ex}=790 nm on a different spot of the sample. The light is polarized along the short axes of the ellipses in all images.

Fluorescence intensity upon linear and nonlinear excitation

If a two-photon process is the underlying mechanism of the fluorescence, intensity should increase quadratically with the exciting laser power. Thus, the fluorescence intensity of the polymer-bound dye Atto425 was studied on a reference sample (glass slide with polyelectrolyte layers and covalently bound dye, as described in Chapter 3) and on a sample with the gold structure, the spacer polymer and the dye.

The procedure was as follows: For the reference sample, an overview image of the surface was performed to verify that the dye is uniformly distributed. Subsequently, the fluorescence intensities of eight different squares were measured, increasing the laser intensity from 0 % up to 5 % for the two-photon process, and up to 100 % for the linear process.[xviii]

For the sample with the gold structure, no overview image was taken to avoid bleaching. The fluorescence intensities of areas containing equal numbers of nanostructures were recorded at varying excitation intensities. As the background signal is negligible, the collected signal gave a mean fluorescence intensity on top of the gold. Due to strong bleaching effects at high intensities, it could only be measured at low laser powers (up to 1.7 % for the two-photon process, and up to 2.5 % for the one-photon process, respectively).

Fig. 22 a. shows the fluorescence intensity of the reference sample plotted versus the excitation intensity for the irradiation with laser light of 458 nm. The fluorescence intensity of the polymer-bound dye shows a linear dependence on excitation power, corresponding to a one-photon process. Fig. 22 b. shows the fluorescence intensity of the reference sample plotted versus the incident laser power for irradiation at 790 nm. The resulting power law given by the fit states a dependence to the power of 2.36 ± 0.15, which indicates a two-photon process. The slight discrepancy from the expected value 2.0 can be attributed to statistical errors, and impreciseness of the focusing process. The bottom row of Fig. 22 shows the fluorescence intensity on the gold structures. Fig. 22 c. reveals the linear dependence upon irradiation with 458 nm laser light, and Fig. 22 d. shows a quadratic dependence upon illumination with laser light of 790 nm. Here, the resulting intensity dependence goes to the power of 2.19 ± 1.13. The high error is a result of the low statistics. Still, all curves reveal the linear dependence upon irradiation with 458 nm laser light, and quadratic dependence upon illumination with laser light of

[xviii] The relative change in the laser intensity can be determined with much higher accuracy than the absolute light intensity at the surface. [50] Therefore, only relative units (%) are stated and used for further analysis. For the Ti:Sa laser at 790 nm, 1 % laser power corresponds to 1 mW on the sample; it increases linearly with the percentage values. The 458 nm line of the Argon laser features even less energy.

790 nm. This indicates that the dye can be excited via a two-photon process, regardless whether it is positioned on a nanostructure or far away of it.

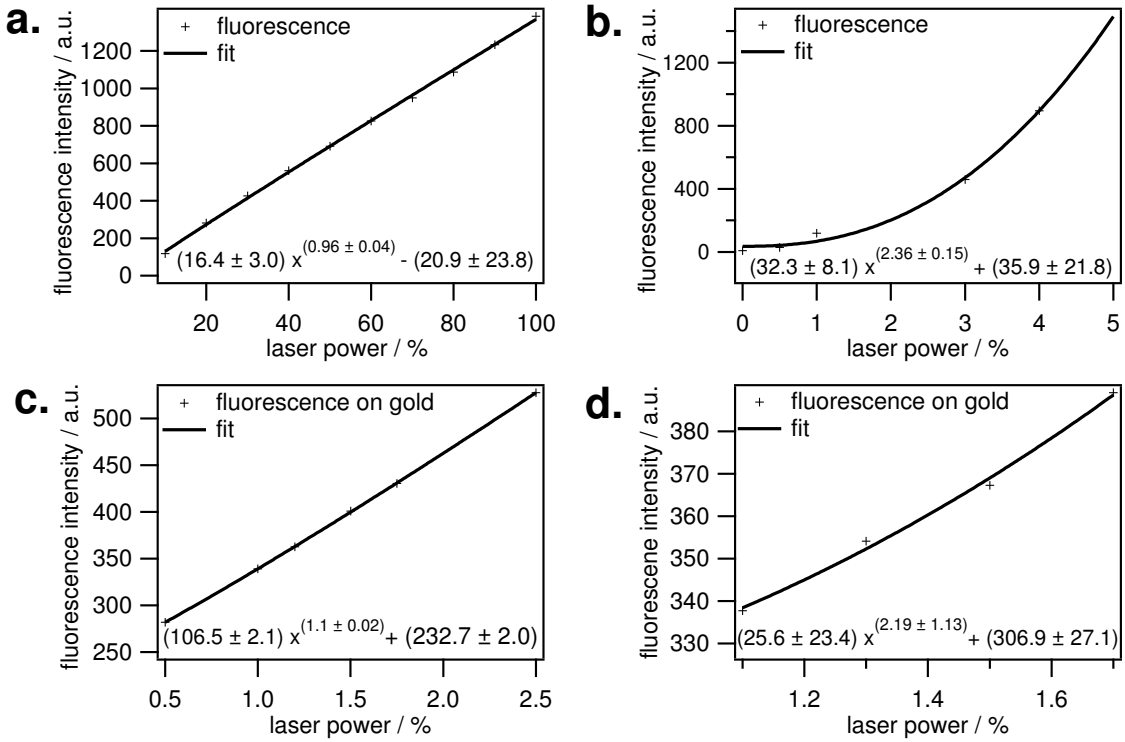

Figure 22: Top row: fluorescence signal of the reference sample upon irradiation with light of 458 nm (a.) and 790 nm (b.) with increasing excitation power. Bottom row: fluorescence signal on the gold upon irradiation with light of 458 nm (c.) and 790 nm (d.) with increasing excitation power.

Calculation of the fluorescence enhancement factor

In the following, a detailed derivation of the calculation of the fluorescence enhancement factor is given. The main idea is to divide the surface into two parts: first, the area without gold structure, where the fluorescence from nonenhanced dye molecules and the background (from glass and polymer spacer) contribute to the signal, and second, the area covered by the gold structures. Here, the fluorescence of the enhanced dyes, the gold autoluminescence, and the background are detected. All inhomogeneities within the fluorescence signal of the dyes close to the gold structures are neglected, that is, the crude assumption is made that all dyes within the geometrical dimension of the ellipses are enhanced by the same factor while the others far away from the gold are not. This provides a lower limit to the maximum enhancement experienced by some dye molecules, because theoretical calculations demonstrate that the field enhancement is localized at the edges of the elliptical nanostructure (Fig. 19). Moreover, as the quenching effect in the emission is not taken into account, the enhancement effect is

underestimated in double respect.

Let the experimental signal of the brightness on top of the dye-covered nanostructures be B_{dye}^{Au}. It is the integrated intensity of an area A_{sq} of the fluorescence micrograph, which is bigger than the gold nanostructure. The brightness B is defined as the signal from an area A_{sq} which can be divided in subregions A_n with different local intensities I_n:

$$B = I_{sq} \cdot A_{sq} = I_1 \cdot A_1 + I_2 \cdot A_2 + \cdots + I_n \cdot A_n \tag{18}$$

For both the dye-covered substrates (e.g. Fig. 22 c., p. 37) and the reference sample without dye (e.g. Fig. 22 d., p. 37), an area around the bright spots and an area far away from the gold structure were analyzed in each case. Fig. 23 shows a sketch of these analyzed squared areas A_{sq}.

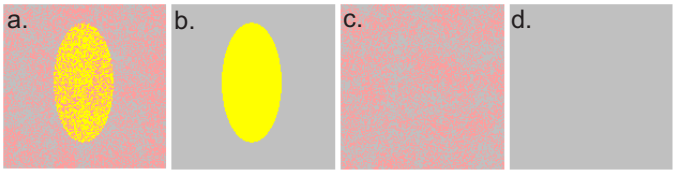

Figure 23: Schematic illustration of the parameters for the calculation of the fluorescence enhancement factor. The gold is depicted in yellow, the dye is red and the background is grey. a. B_{dye}^{Au} b. B_{nodye}^{Au} c. B_{dye}^{noAu} d. B_{bg}

Besides the desired fluorescence signal from the top of the gold structure, the measured brightness B_{dye}^{Au} also contains other contributions: the autoluminescence of the bare gold B_{nodye}^{Au}, the signal of the non-enhanced dye B_{dye}^{noAu}, and he background signal B_{bg}. In a first step, the signal of the gold B_{nodye}^{Au} is subtracted from the signal of the dye-covered gold B_{dye}^{Au}. This yields the amount of the contribution of the dye fluorescence on the total signal. The dye contribution consists of two parts: the signal of the dye on the gold and far away from the gold. Now the very crude assumption is made that all dyes within the geometrical projection of the ellipses are enhanced by the same factor while the others are not. This provides a lower limit to the maximum enhancement experienced by some dye molecules.
Thus, two different areas are introduced: A_{obj} is the area of the object, namely the gold ellipses (obtained by electron microscopy) and A_{sq} is the area of the analyzed square in the fluorescence micrograph (given by the fluorescence microscope software). The (possibly) enhanced intensity is ascribed to the area of the ellipses A_{obj} and the nonenhanced intensity to the area around the ellipses $A_{sq} - A_{obj}$. Now one arrives at

the following Equation (19):

$$(B_{dye}^{Au} - B_{nodye}^{Au}) = I_{enh} \cdot A_{obj} + I_{nonenh} \cdot (A_{sq} - A_{obj}) \tag{19}$$

If there was no gold structure, the overall intensity would equal I_{nonenh}, and the experimental signal would be B_{dye}^{noAu}. Rearranging (19), and identifying the term $I_{nonenh} \cdot A_{sq}$ as $B_{dye}^{noAu} - B_{bg}$ as by definition, I_{nonenh} determines the background-corrected signal of the dye, a definition for I_{nonenh} is obtained:

$$I_{nonenh} = \frac{B_{dye}^{noAu} - B_{bg}}{A_{sq}} \tag{20}$$

Thus, combining (19) and (20) and rearranging yields

$$(B_{dye}^{Au} - B_{nodye}^{Au} - B_{dye}^{noAu} + B_{bg}) = I_{enh} \cdot A_{obj} - I_{nonenh} \cdot A_{obj} \tag{21}$$

As already stated above, Equation (21) shows that the experimental signal B_{dye}^{Au} has to be corrected by the factors B_{nodye}^{Au} and B_{dye}^{noAu}, which also contribute to the measured signal. As the background is subtracted twice because both B_{nodye}^{Au} and B_{dye}^{noAu} include the background signal, it has to be added once to obtain the correct value. Rearranging (21) yields

$$\frac{I_{enh}}{I_{nonenh}} = 1 + \frac{(B_{dye}^{Au} - B_{nodye}^{Au} - B_{dye}^{noAu} + B_{bg})}{I_{nonenh} \cdot A_{obj}} \tag{22}$$

Again, Equation (20) is used, and, finally, one arrives at an expression for the quested ratio I_{enh}/I_{nonenh}:

$$\frac{I_{enh}}{I_{nonenh}} = 1 + \frac{(B_{dye}^{Au} - B_{nodye}^{Au} - B_{dye}^{noAu} + B_{bg}) \cdot A_{sq}}{(B_{dye}^{noAu} - B_{bg}) \cdot A_{obj}} \tag{23}$$

Equation (23) offers an easy way to compare the intensities of the dye on top of the gold with the dye far away from the gold. If the ratio $I_{enh}/I_{nonenh} > 1$, the dye molecules on the gold show increased fluorescence, if $I_{enh}/I_{nonenh} = 1$, there is no effect of the gold on the fluorescence and, finally, if $I_{enh}/I_{nonenh} < 1$, a quenching effect occurs.

Rearranging (23) and using (20) yields a definition for I_{enh}:

$$I_{enh} = \frac{(B_{dye}^{Au} - B_{nodye}^{Au} - B_{dye}^{noAu} + B_{bg})}{A_{obj}} + \frac{(B_{dye}^{noAu} - B_{bg})}{A_{sq}} \tag{24}$$

Likewise, the contribution of the gold autoluminescence, I_{gold}, was defined as

$$I_{gold} = \frac{(B^{Au}_{nodye} - B_{bg})}{A_{obj}} + \frac{B_{bg}}{A_{sq}}\,. \tag{25}$$

And, finally, the background parameter, I_{bg}, was defined as

$$I_{bg} = \frac{B_{bg}}{A_{sq}}\,. \tag{26}$$

With these definitions at hand, the corrected fluorescence intensities are calculated and presented in the next section.

Corrected fluorescence intensities of the different luminescence mechanisms. For B^{Au}_{dye} and B^{Au}_{nodye}, the intensities of twenty individual particles were analyzed; for B^{noAu}_{dye} and B_{bg}, the intensities of twenty spots without particles on the surface were taken. The mean intensities were taken for further analysis and the calculations have been done with the following experimental data (Table 1). The indicated errors represent the statistical errors of the measured values. The variation coefficients represent the percental error independent of the value, thus, offering a comparable indication of the statistical error.

parameter	brightness B / counts	variation coefficient	areas / μm^2
B^{Au}_{dye}	105,633 ± 5,999	5.68 %	$A_{sq} = 0.2343$
B^{Au}_{nodye}	86,515 ± 4,170	4.82 %	
B^{noAu}_{dye}	35,211 ± 588	1.67 %	$A_{obj} = 0.1385$
B_{bg}	33,275 ± 507	1.53 %	

Table 1: Experimental data for the resonance case (short axes, 180 nm structure).

By proper referencing according to the method described in the previous section, the individual contributions of the nonenhanced dye, I_{nonenh}, the background, I_{bg}, the gold, I_{gold}, and the enhanced dye, I_{enh}, were determined. The results are shown in Table 2. The indicated errors are obtained by error propagation of the data given in Table 1.

The resulting enhancement factor I_{enh}/I_{nonenh} is 16, i.e. the intensity of the dye on top of a nanostructure, I_{enh}, is 16 times higher than the intensity of a dye on glass.

parameter	180 nm short axes, corrected fluorescence / counts/μs
I_{enh}	160 ± 57
I_{nonenh}	10 ± 2
I_{gold}	638 ± 96
I_{bg}	172 ± 140
I_{enh}/I_{nonenh}	16

Table 2: Corrected fluorescence intensities of the different luminescence mechanisms for the short axes of the 180 nm ellipses.

4.2.2 Excitation of the long axes of 180 nm nanostructures

In order to prove that it is the resonance-enhanced electrical near-field of the metal structure which causes the signal enhancement, the investigation of an off-resonance case is inevitable. For this purpose, nanostructures with a plasmon resonances at a wavelength higher than 790 nm were designed. Under the applied experimental conditions, only the dye should be excited with the incident laser light. Hence, the metal structure should not show an effect on the fluorescence. The first examined off-resonant case forms the excitation of the long axes of the elliptic nanostructures described above. As the long axes exhibit a resonance at 1300 nm after coating, this resonance should not be excited by the Ti:Sa laser. As a result, no fluorescence enhancement is expected.

Fig. 24 shows the reflectivity (a.), the linear fluorescence (b.), the nonlinear fluorescence (c.) of the dye-covered sample and the signal of the gold structure without dye (d.). In all images, the light is polarized along the long axis of the elliptic structure. Fig. 24 a., b. and c. show the same spot on the sample surface, whereas Fig. 24 d. was recorded before dye deposition and, thus, represents a different area of the sample.
As in the previous subchapter, the ellipses' positions are determined with the reflectivity image (Fig. 24 a.), and they appear as dark spots on the image of the linear emission (Fig. 24 b.), indicating quenching. The two-photon induced signals with (Fig. 24 c.) and without dye (Fig. 24 d.) reappear as bright spots. Nevertheless, it cannot directly be determined which signal is higher.
Remarkably, in both images, every ellipsis generates two signals at its edges. This pattern corresponds to the electric near-field distribution of the long axis. Therefore, as the size of this axis is in the range of the resolution limit of the microscope, it is presumed that it is possible to directly image the electric near-field of the nanostructure. It should be emphasized that this measurement is very sensitive to the normal position of the focus, a little defocusing directly causes merging of the two spots.

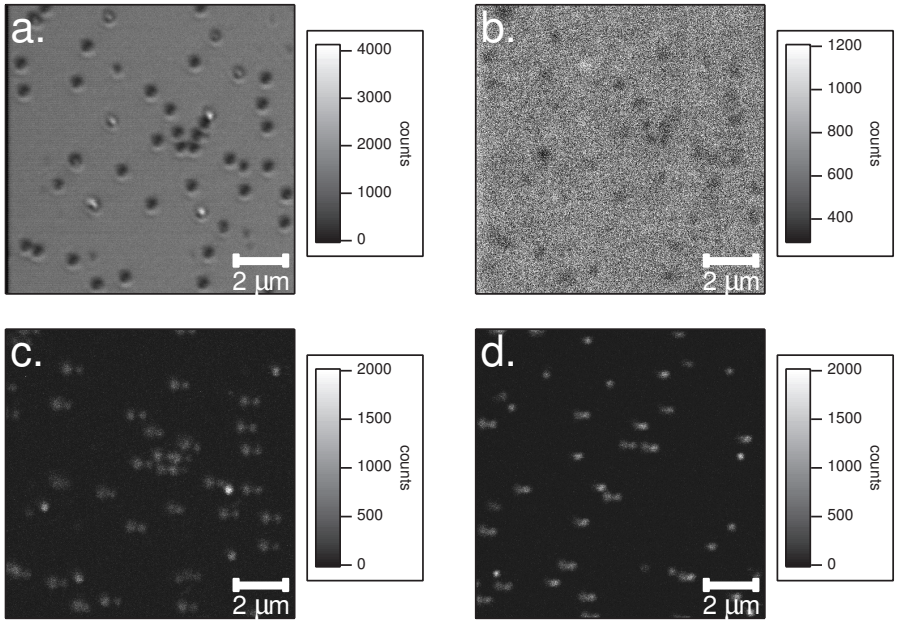

Figure 24: 180 nm ellipses, long axes: a. Reflectivity at λ_{ex}=488 nm, b. linear fluorescence at λ_{ex}=458 nm, and c. two-photon induced fluorescence at λ_{ex}=790 nm of one spot on the sample. d. Autoluminescence signal of the gold at λ_{ex}=790 nm on a different spot on the sample. The light is polarized along the long axes of the ellipses in all images.

Corrected fluorescence intensities of the different luminescence mechanisms. Again, twenty different particles were analyzed, yielding the experimental data stated in Table 3.

parameter	brightness B / counts	variation coefficient	areas / μm^2
B_{dye}^{Au}	93,600 ± 2,817	3.60 %	A_{sq} = 0.4357
B_{nodye}^{Au}	90,450 ± 4,432	4.90 %	
B_{dye}^{noAu}	65,025 ± 611	0.94 %	A_{obj} = 0.1385
B_{bg}	61,875 ± 254	0.31 %	

Table 3: Experimental data for the off-resonance case (long axes, 180 nm structure).

By proper referencing the contributions of the dye, the background, the gold and the enhanced dye are obtained (Table 4).

Apparently, the autoluminescence of the gold is decreased by one third in this polarization direction; nevertheless, the signal is still very strong. The signal of the enhanced dye, I_{nonenh}, equals the one of the nonenhanced dye, I_{nonenh}. The obtained enhancement factor is I_{enh}/I_{nonenh}=1. Hence, the two-photon effect behaves as anticipated from a perfect structure, whereas the autoluminescence cannot be switched off by a polarization change. Possibly, the autoluminescence is evoked by microcracks or similar irregularities on the gold structure which are excited by the incident laser light independent

parameter	180 nm long axes, corrected fluorescence / counts/μs
I_{enh}	9 ± 5
I_{nonenh}	9 ± 4
I_{gold}	422 ± 90
I_{bg}	172 ± 1
I_{enh}/I_{nonenh}	1

Table 4: Corrected fluorescence intensities of the different luminescence mechanisms for the long axes of the 180 nm structure.

of the polarization. The roughness of the gold can lead to local scattering processes, which may couple incident radiation to a resonance with perpendicular polarization. Such scattering processes may be strongly enhanced due to the increased photonic mode density which is a signature of plasmonic resonances. [28,69]

4.2.3 Excitation of the long axes of 500 nm nanostructures

The second off-resonant case is a structure which does not support any resonance at the illumination wavelength. Therefore, a similar elliptic structure but with a size of 0.5 µm × 2 µm was fabricated (Fig. 25). The resonance wavelengths of both axes lay in the infrared, thus, neither of them is excited by the laser light.

There is a subtle difference to the off-resonant excitation of the ellipses with light polarized perpendicular to the resonance dipole as discussed in Chapter 4.2.2. For an ideal object, the response of the dye fluorescence would be similar to the response of the long axes of the 180 nm structure. In the real world, though, imperfect samples are rough. As explained in Chapter 4.2.2, this can cause coupling of the excitation light to the resonance perpendicular to the applied polarization. In the case of the 500 nm particles, this coupling should not be possible due to the lack of a resonance at the incident wavelength.

Fig. 26 is arranged as the previous cases. The reflectivity image (a.) reveals the positions of the gold structures. Again, the gold causes a quenching of the linear fluorescence (Fig. 26 b.). The two-photon induced fluorescence and the autoluminescence of the gold (Fig. 26 c. and d., respectively) show low intensities compared to the signal of the long axes of the smaller structure.[xix] This is attributed to the fact that none of

[xix] Note the different scalings of the colorbars.

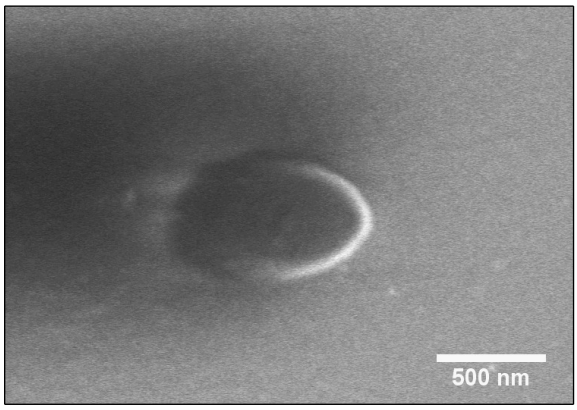

Figure 25: Scanning electron microscope image of gold ellipses prepared with a colloidal mask of 500 nm in diameter.

the resonance wavelengths of the gold structure coincides with the applied laser wavelength.

In addition, the same double-spot pattern is observed, as seen in Fig. 26 (c. and d., 44). The spacing between the spots correlates with the size of the nanostructure. These findings confirm the assumption that with the well-defined systems applied in these studies, the direct mapping of the electrical near-field distribution is possible.

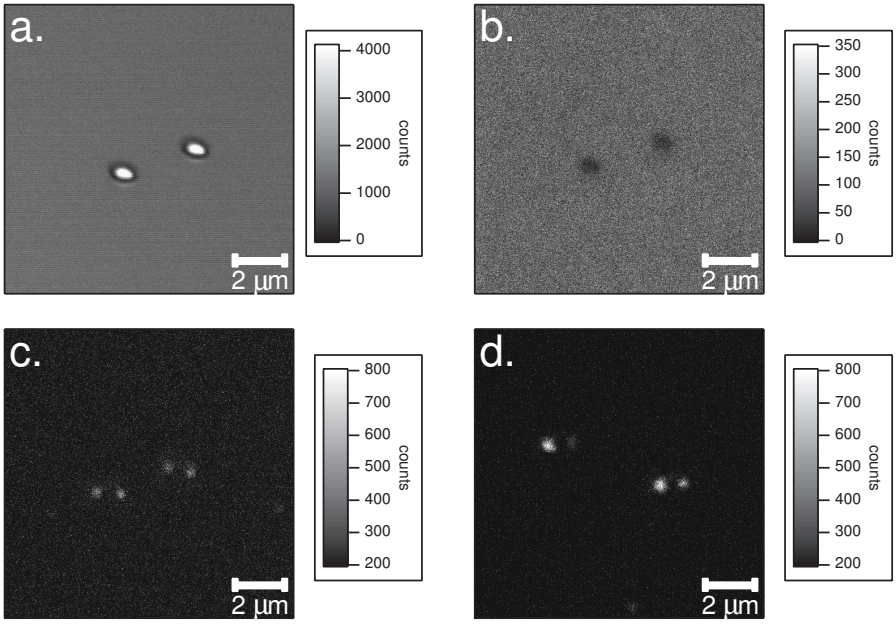

Figure 26: 500 nm ellipses: a. Reflectivity at λ_{ex}=488 nm, b. linear fluorescence at λ_{ex}=458 nm, and c. two-photon induced fluorescence at λ_{ex}=790 nm of one spot on the sample. d. Autoluminescence signal of the gold at λ_{ex}=790 nm on a different spot on the sample. The light is polarized along the long axes of the ellipses in all images.

Corrected fluorescence intensities of the different luminescence mechanisms. The experimentally obtained intensities can be found in Table 5.

parameter	brightness B / counts	variation coefficient	areas / μm^2
B_{dye}^{Au}	504,000 ± 7,056	1.40 %	$A_{sq} = 3.0981$
B_{nodye}^{Au}	488,000 ± 8,638	1.77 %	
B_{dye}^{noAu}	462,400 ± 1,618	0.35 %	$A_{obj} = 1.6010$
B_{bg}	435,200 ± 740	0.17 %	

Table 5: Experimental data for the off-resonance case (long axes, 500 nm structure).

The individual contributions of the dye, the background, the gold and the enhanced dye are calculated as described before(Table 6).

parameter	500 nm long axes, corrected fluorescence / counts/μs
I_{enh}	2 ± 2
I_{nonenh}	11 ± 1
I_{gold}	210 ± 2
I_{bg}	170 ± 1
I_{enh}/I_{nonenh}	0.2

Table 6: Corrected fluorescence intensities of the different luminescence mechanisms for the long axes of the 500 nm structure.

A lower autoluminescence of the gold for this structure is observed, but it is still a significant part of the signal. Apparently, local scattering processes occur on this sample, supporting the assumption that this effect is caused by irregularities on the surface of the nanostructure. The enhancement factor results as I_{enh}/I_{nonenh} =0.2. Here, the ratio of both intensities is less than 1, which indicates a dominating quenching effect.

Table 7 summarizes the corrected fluorescence intensities of all presented structures.

In the case of the excitation along the long axes of 180 nm ellipses, the observed fluorescence enhancement is zero (as the factor I_{enh}/I_{nonenh} equals 1). For the 500 nm ellipses, a quenching is found (I_{enh}/I_{nonenh} is less than 1). This shows that crosstalk between different polarizations is negligible for fluorescence.
Interestingly, the gold contribution I_{gold} is smallest for the 500 nm samples. This may point to a polarization crosstalk effect which plays a role for the gold autoluminescence.

parameter	in resonance, fluorescence / counts/μs	off-resonance, fluorescence / counts/μs	off-resonance, fluorescence / counts/μs
I_{enh}	160 ± 57	9 ± 5	2 ± 2
I_{nonenh}	10 ± 2	9 ± 4	11 ± 1
I_{gold}	638 ± 96	422 ± 90	210 ± 2
I_{bg}	172 ± 140	172 ± 1	170 ± 1
I_{enh}/I_{nonenh}	16	1	0.2

Table 7: Comparison of the corrected fluorescence intensities of the different luminescence mechanisms.

4.3 Conclusions and Outlook

The two-photon induced fluorescence on defined metal structures has been investigated. The experimental procedure allows to identify, separate and quantify the different contributions to the fluorescence signal. An enhancement of the fluorescence signal by a factor of almost 20 for dyes in the near-field of the nanostructure compared to those dye molecules which are positioned outside the near-field regime is detected. Theoretical calculations prove that the dye layer is positioned within the near-field regime of the nanostructure. It is shown that a significant contribution to the signal is due to the two-photon excited autoluminescence of the gold nanostructure. Under the applied dye concentration, the nonenhanced dye only gives a weak two-photon induced fluorescence signal, but in close vicinity of a gold nanostructure, its fluorescence signal achieves the same range as the autoluminescence.
When the plasmon resonances of the ellipses do not coincide with the excitation laser wavelength, no fluorescence enhancement is detected, in spite of a considerable gold autoluminescence.

The described method might be relevant for biological applications as the dye can be used for direct protein labeling and the polymer spacing protects the biological samples from potential toxic effect of the metal. As the images originate from an area 40 nm above the nanostructure, also studies of cells and cell organelles are feasible.

When the dimensions of the metal nanostructures are in the range of the resolution limit of the microscope or bigger, a direct visualization of the shape of the electric near-field by detection of the two-photon induced luminescence of the gold structure is achieved.

A systematic change of the spacer thickness between the metal structure and the dye

layer is presented in Chapter 5, demonstrating an experimental exploration of the range of the electrical near-field. An analysis of the distance-dependent enhancement factors gives an insight into the optimum position of the dye relative to the metal structure.

Chapter 5

Maximizing two-photon induced Fluorescence Enhancement on Plasmonic Nanostructures

5.1 Introduction

The electric near-fields of noble metal nanostructures are able to enhance the emission intensity of fluorescent dyes in close proximity. [34–36] In recent years, these enhancement effects have also been studied with two-photon excitation. As the absorption transition probability scales to the power of 4 with the electrical field, a main advantage of the two-photon approach is the increased detectable signal compared to an equivalent one-photon experiment. Glass et al. reported on an increased two-photon excited fluorescence of Rhodamine B on silver metal islands [57], and Gryczynski and coworkers found an enhanced multiphoton-excited fluorescence of Rhodamine B on silver islands. [70] Cohanoschi et al. studied the two-photon absorption of organic dyes in aqueous gold colloid suspensions. [58,71] More recently, Jung and coworkers used the two-photon excited fluorescence enhancement on gold nanopatterns for ultrasensitive DNA detection. [72]

In two-photon excitation, several luminescence signals contribute to the overall emission. However, the emission signal is mainly determined by the fluorescence of the dye and the autoluminescence of the metal. In the previous chapter, it has been demonstrated how these contributions can be separated allowing a precise investigation of the real dye fluorescence signal. However, all possible quenching effects have been neglected, although quenching of the one-photon excited fluorescence was observed.

The underlying quenching mechanism is the electromagnetic non-radiative de-excitation via decay channels introduced by the metal interface (see Chapter 2.3.4). As some electrons reach the ground state by these non-radiative de-excitation channels, the fraction of radiative and thus detectable transitions is diminished. Moreover, including instrument-specific detection efficiencies leads to further reduction of the detectable signal.
As explained in Chapter 2.3.3, the excitation rate of a dye can be enhanced close to a metal interface. However, this enhanced excitation must be related to the possibility of a detectable emission to explain and predict the measured fluorescence enhancement.

The surface enhanced luminescence strongly depends on the electrical near-field and thus on the material of the nanoparticle. [19,73,74] It has been shown theoretically that at a given geometry silver exhibits a higher electric near-field than gold. [75] Still, a thorough comparative study of the different effects of gold and silver on the fluorescence in the same experimental setup has not yet been described in literature. Additionally, the shape plays an important role on the strength of the electrical near-field. [19,20] Especially at sharp tips, the electric near-field is strongly enhanced, usually referred to as antenna effect. It has been shown theoretically that gold crescents have a fivefold higher field enhancement than gold ellipses. [76] Due to the higher electrical near-field, the effect on the fluorescence intensity enhancement should be increased compared to simpler structures with lower field enhancement. Up to now, research mainly focused on the fabrication of new advanced nanoparticles, and many sophisticated structures could be achieved, e.g. nanorods [77], triangles [78], bowties [79], cubic structures [80], and others [81–83]. Anyhow, these complex structures were primarily investigated regarding their inherent optical properties, and not regarding their influence on other molecules, such as fluorophores. Defined measurements of the effect of differently shaped nanostructures are absent in current research.

Here, an experimental exploration of the electrical near-field by distance-dependent studies of the fluorescence enhancement for gold and silver ellipsoids, as well as for gold crescent-shaped nanoparticles is presented. This approach allows a detailed investigation of both the material and the shape effect on the fluorescence intensity of a fluorophore in close proximity of the nanostructure. Applying nanosphere lithography in combination with a well-defined spacer geometry gives precise control over the structure design. A theoretical discussion on the surface enhanced excitation and the surface induced quenching allows for an improved conclusion on the composition of the experimentally obtained fluorescence enhancement.

5.2 Results and Discussion

5.2.1 Distance-Dependent Fluorescence Enhancement on Gold Elliptic Nanostructures

The fluorescence intensity of the commercially available dye Atto425 (Atto425-NHS ester, Attotec, Germany) in dependency of the distance to gold elliptic nanostructures with average dimensions of approximately 180 nm × 245 nm was investigated. Therefore, the thickness of a polymer spacer attached to the substrate was varied, adjusting

the distance between the gold structure and the dye. The nanostructure supports a resonance at 790 nm, the applied excitation wavelength. Fig. 27 shows the extinction spectrum of the short axes of the gold ellipses.

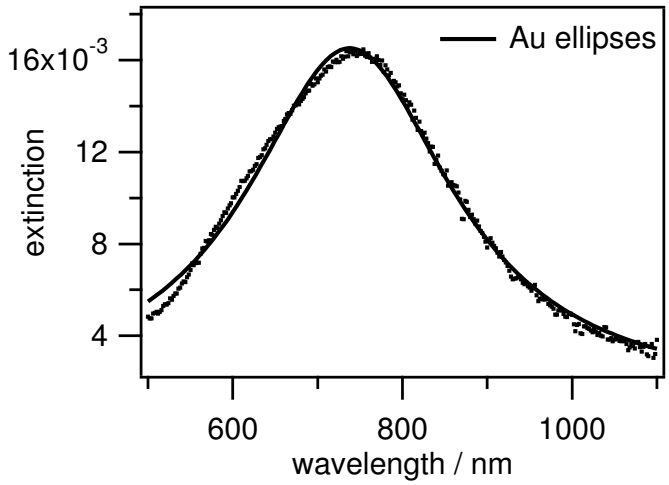

Figure 27: Extinction of gold ellipses before deposition of polyelectrolyte bilayers recorded with light polarized along the short axes of the structures. The curve is fitted with a Lorentz function.

Two-photon induced fluorescence was studied on six different samples, all of them featuring a different thickness of the polymer spacer. The real distance has been investigated by Vasilev et al. using surface plasmon resonance spectroscopy [84], and by Bocchio et al., applying atomic force microscopy [85]. Fig. 28 shows the two-photon excited fluorescence and the autoluminescence of gold ellipses coated with two polyelectrolyte bilayers, which is the distance where maximum enhancement occurs.

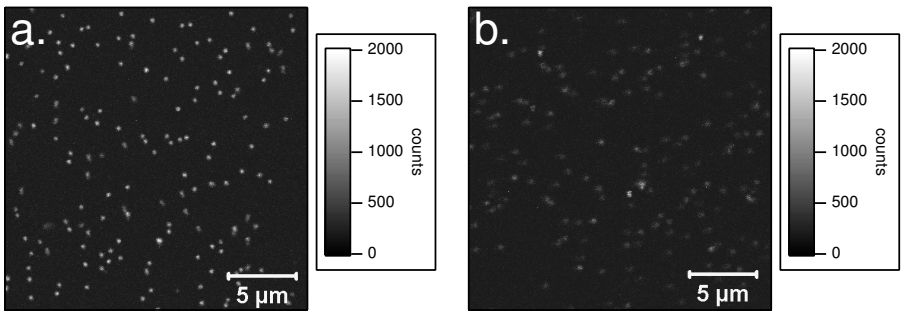

Figure 28: Gold ellipses coated with two polyelectrolyte bilayers: a. two-photon induced fluorescence at λ_{ex}=790 nm of one spot on the sample, b. autoluminescence signal of the gold at λ_{ex}=790 nm on a different spot on the sample. The light is polarized along the short axes of the ellipses in all images.

The bright spots in the two-photon excited fluorescence image (Fig. 28 a.) can be attributed to areas where the nanostructures are located (by analysis of a reflection

image as described in Chapter 4). The autoluminescence signal is clearly lower in intensity than the fluorescence signal. Thus, a big contribution to the signal detected in Fig. 28 a. must be the fluorescence of the dye. As described in the previous chapter, twenty different spots on and far away of the nanostructure were analyzed. Table 8 contains the experimental data. The indicated errors represent the statistical errors of the measured values.

parameter	brightness B / counts	variation coefficient	areas / μm^2
$B_{dye}^{Au}(1)$	274,950 ± 13,909	5.06 %	$A_{sq} = 0.4357$
$B_{dye}^{Au}(2)$	339,300 ± 18,313	5.40 %	
$B_{dye}^{Au}(3)$	310,725 ± 38,538	12.40 %	$A_{obj} = 0.1385$
$B_{dye}^{Au}(4)$	301,950 ± 31,736	10.51 %	
$B_{dye}^{Au}(5)$	287,550 ± 21,741	7.56 %	
$B_{dye}^{Au}(6)$	282,375 ± 14,745	5.22 %	
B_{nodye}^{Au}	218,025 ± 27,883	12.79 %	
B_{dye}^{noAu}	61,875 ± 2,687	4.34 %	
B_{bg}	67,500 ± 1,033	1.53 %	

Table 8: Experimental data for the gold ellipses.

The obtained emission signals were corrected by the gold autoluminescence, the background and the fluorescence of the nonenhanced dye molecules, according to the method described in Chapter 4. An enhancement factor was calculated for each sample, representing the ratio between the enhanced fluorescence intensity and the nonenhanced fluorescence intensity, I_{enh}/I_{nonenh}. The calculated enhancement factors of the gold ellipses for the different spacer thicknesses are listed in Table 9. A graphic illustration can be found in Fig. 36.

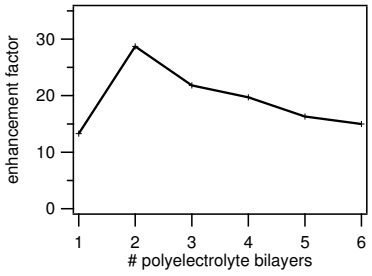

Figure 29: Fluorescence intensity of the dye Atto425 in dependence of the distance to gold elliptic nanostructures.

number of polyelectrolyte bilayers	enhancement factor I_{enh}/I_{nonenh}
1	13.3
2	28.7
3	21.8
4	19.7
5	16.3
6	15.0

Table 9: Calculated fluorescence enhancement factors of gold ellipses for different amounts of polyelectrolyte spacer bilayers.

The sample with a spacer thickness of two polyelectrolyte bilayers, according to a real distance of 8 nm, yields the strongest fluorescence enhancement factor of almost

30. This means, the fluorescence of the dyes placed on the gold is 30 times higher than the fluorescence signal of the dyes positioned far away of the gold. With increasing distance between the dye and the gold the enhancement factor decreases, pointing to the evanescent nature of the electrical field of the nanostructure. For the smallest distance of 4 nm (one bilayer), a fluorescence enhancement factor of 13 is found. This average net enhancement indicates that most probably two competing processes occur simultaneously, namely the quenching and enhancement. Apparently, even for very small distances between the dye and the metal, the enhancement effect is dominating over the quenching process, impeding complete erasure of the fluorescence.
As explained in Chapter 2.3.4, the observed quenching is caused by non-radiative decay channels introduced by the metal interface. This decreases the radiative fraction of the total de-excitation.
Hence, the detectable fluorescence intensity depend not only on the excitation rate and on the detection efficiency, but also on the extent of the detectable fraction of the de-excitation (see Chapter 2.3.4 for details).

The excitation rate of the dye molecules can be increased when brought in the electrical near-field of a metal nanostructure. In contrast, the detectable de-excitation can decrease, as the metal may insert additional non-radiative decay channels.
The concomitance of these two factors – enhancement and quenching – is reflected in the course of the enhancement factors plotted in Fig. 9.

5.2.2 Distance-Dependent Fluorescence Enhancement on Silver Elliptic Nanostructures

The stronger electrical near-field of silver compared to gold should lead to a stronger effect on absorption and fluorescence of organic dyes placed close to silver nanoparticles compared to dye molecules positioned next to identical gold structures. Here, a well-defined system geometry is used to perform quantitative studies of the material effect in near-field mediated fluorescence enhancement.

The fluorescence intensity of the dye Atto425 (Atto425-NHS ester, Attotec, Germany) in dependency of the distance to silver elliptic nanostructures with average dimensions of 197 nm × 324 nm is studied. Fig. 30 shows a scanning electron microscope image of the silver elliptic nanostructures.

As silver has different optical properties than gold, distinct resonance frequencies are obtained for equal structures except for the material. To compare the experimental

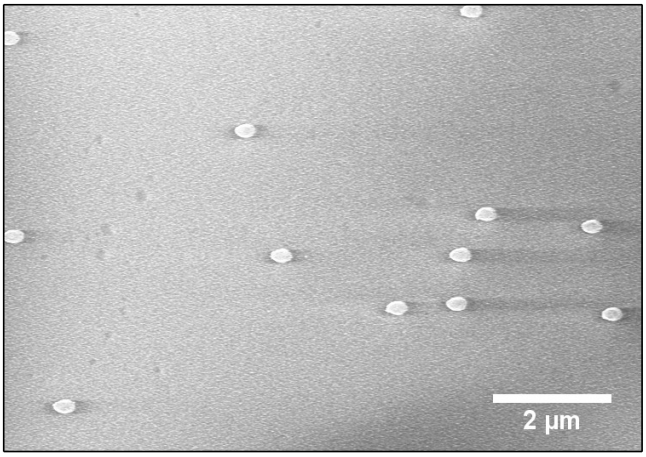

Figure 30: Scanning electron microscope image of bare silver ellipses on a glass substrate.

data obtained for silver nanostructures with those of the gold structure, the size of the silver nanostructure had to be increased in order to match the resonance frequency of the gold analog. Both the gold and the silver elliptical nanostructures show a high extinction around 800 nm. Fig. 31 shows the extinction spectra of the investigated uncoated samples.

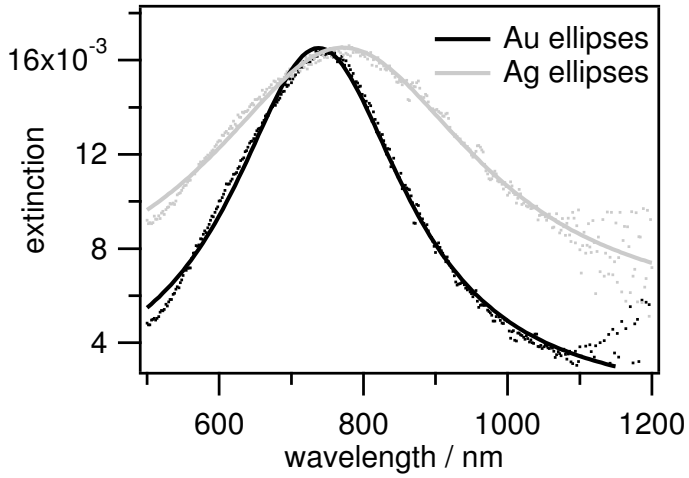

Figure 31: Extinction of gold (black curve) and silver (gray curve) ellipses before deposition of polyelectrolyte bilayers recorded with light polarized along the short axes of the structures. The curves are fitted with Lorentz functions.

Two-photon induced fluorescence was studied on six different samples with silver elliptic nanostructures, all of them featuring a different thickness of the polymer spacer. Fig. 32 shows the nonlinear fluorescence of the dye-covered sample with two polyelectrolyte bilayers and the autoluminescence of the bare silver structure. Although the

autoluminescence signal of the silver (Fig. 32 b.) is a significant contribution, yet compared to the gold, silver autofluorescence seems to be less intense.

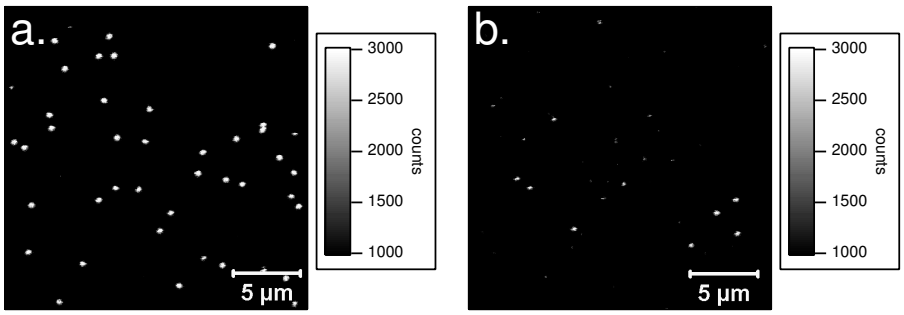

Figure 32: Silver ellipses coated with two polyelectrolyte bilayers: a. two-photon induced fluorescence at λ_{ex}=790 nm of one spot on the sample, b. autoluminescence signal of the silver at λ_{ex}=790 nm on a different spot on the sample. The light is polarized along the short axes of the ellipses in all images.

Again, different spots were analyzed and their mean intensities were taken for further analysis. Table 10 shows the experimental results.

The corrected emission signals were used to calculate the distinct enhancement factors

parameter	brightness B / counts	variation coefficient	areas / μm^2
$B_{dye}^{Ag}(1)$	279,568 ± 17,886	6.40 %	$A_{sq} = 0.4357$
$B_{dye}^{Ag}(2)$	336,905 ± 20,815	6.18 %	
$B_{dye}^{Ag}(3)$	282,697 ± 18,497	6.54 %	$A_{obj} = 0.201$
$B_{dye}^{Ag}(4)$	257,245 ± 26,866	10.44 %	
$B_{dye}^{Ag}(5)$	245,604 ± 24,482	9.97 %	
$B_{dye}^{Ag}(6)$	235,115 ± 41,744	17.75 %	
B_{nodye}^{Ag}	216,096 ± 31,537	14.59 %	
B_{dye}^{noAg}	66,600 ± 2,004	3.01 %	
B_{bg}	60,525 ± 2,549	4.21 %	

Table 10: Experimental data for the silver ellipses.

for the different samples. The obtained values are presented in Table 11.

As observed for the analog gold structure, the maximum fluorescence enhancement for the silver ellipses is reached at a distance of approximately 8 nm (two polyelectrolyte bilayers) with a factor of 42. For the smallest distance of 4 nm, an enhancement factor of 22 is calculated. As discussed for the gold structure, the quenching effect is superimposed by the competing fluorescence enhancement process, leading to an average net enhancement. With increasing distance between the dye and the metal, the enhancement factor diminishes.

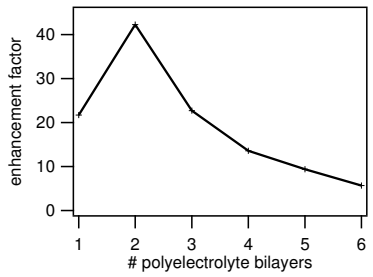

Figure 33: Fluorescence intensity of the dye Atto425 in dependence of the distance to silver elliptic nanostructures.

number of polyelectrolyte bilayers	enhancement factor I_{enh}/I_{nonenh}
1	21.7
2	42.3
3	22.7
4	13.6
5	9.4
6	5.7

Table 11: Calculated fluorescence enhancement factors of silver ellipses for different amounts of polyelectrolyte spacer bilayers.

In comparison to the analog gold structures, the course of the curve for the silver structures is similar, but higher emission intensities and, hence, higher enhancement factors are yielded. The maximum enhancement gives a factor of 30 for gold, whereas, under the same conditions, silver reaches a factor of 42. This is in good agreement with theoretically predicted behavior due to the different electrical near-field distributions of silver and gold ellipses.

5.2.3 Distance-Dependent Fluorescence Enhancement on Gold Crescent-Shaped Nanostructures

Gold elliptic nanostructures exhibit a near-field enhancement of a factor of 6 (Chapter 4), i.e. the incident field is enhanced by the factor 6 in close proximity of the nanostructure. More sophisticated structures, featuring sharp edges or tips, however, give rise to much stronger field enhancements. Crescent-shaped metal nanoparticles for example, offer multiple resonances. [43] The electrical field is strongly confined to the tips, with an electrical near-field enhancement of 30 for gold. [76] Thus, the electronic transitions in an excited dye molecule should be utterly affected by the presence of gold nanocrescents.

The fluorescence intensity of the dye Atto425 (Atto425-NHS ester, Attotec, Germany) on gold nanocrescents is investigated. Due to their two symmetry axes, elliptical structures possess two resonances. The more complex crescent-shaped structures occupy multiple resonances, also including higher order harmonics. The dimension of the nanocrescents had to be adjusted in order to match the resonance wavelength of the above discussed elliptical structures. It is known from literature that gold crescent-shaped nanoparticles fabricated with a colloidal mask with a diameter of 100 nm occupy

a resonance at 800 nm. [86] The crescents had the following dimensions: tip-to-tip distance 83 nm, width of the balk 60 nm, and diameter 114 nm. The resulting surface area is 0.0296 µm^2. Fig. 34 shows a scanning electron microscope image of a crescent-shaped nanoparticle.

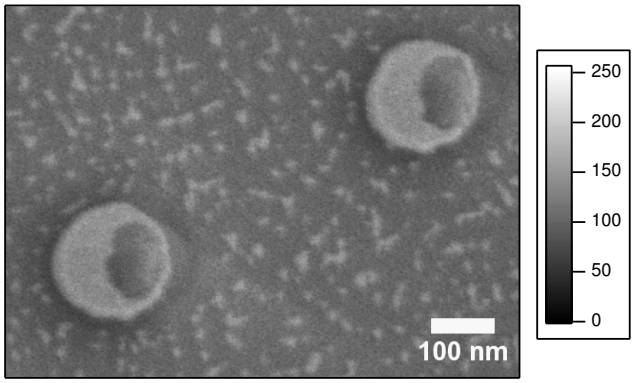

Figure 34: Scanning electron microscope image of a gold crescent-shaped nanoparticle on a glass substrate.

The sample is coated with different numbers of polyelectrolyte bilayers, yielding distinct thicknesses of the polymer spacer. On each sample, the two-photon induced fluorescence was studied (Fig. 35 a.). The autoluminescence signal of the gold crescents is shown in Fig. 35 b.. Similarly to the experiments with the elliptic structures, high emission is detected on top of the nanostructure, while the nonstructured areas appear dark.

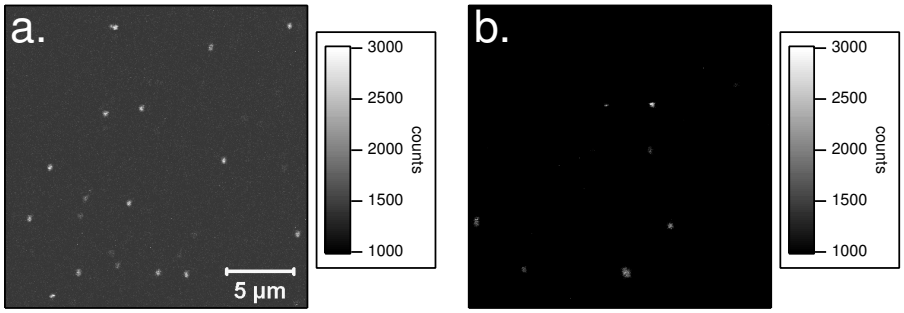

Figure 35: Gold crescents coated with three polyelectrolyte bilayers, U_1 resonance: a. two-photon induced fluorescence at λ_{ex}=790 nm of one spot on the sample, b. autoluminescence signal of the gold at λ_{ex}=790 nm on a different spot on the sample.

The experimentally obtained data can be found in Table 12.

Again, the enhancement factors for each spacer thickness were calculated from the experimental values. The results are listed in Table 13.

parameter	brightness B / counts	variation coefficient	areas / μm^2
$B_{dye}^{Au}(1)$	72,851 ± 6,981	9.58 %	$A_{sq} = 0.1936$
$B_{dye}^{Au}(2)$	75,145 ± 4,045	5.38 %	
$B_{dye}^{Au}(3)$	102,133 ± 10,658	10.44 %	$A_{obj} = 0.030$
$B_{dye}^{Au}(4)$	66,445 ± 4,566	6.87 %	
$B_{dye}^{Au}(5)$	65,056 ± 1,767	2.72 %	
$B_{dye}^{Au}(6)$	64,894 ± 3,004	4.63 %	
$B_{dye}^{Au}(7)$	64,075 ± 4,477	6.99 %	
$B_{dye}^{Au}(8)$	63,450 ± 3,613	5.69 %	
B_{nodye}^{Au}	61,600 ± 9,283	15.06 %	
B_{dye}^{noAu}	29,600 ± 897	3.03 %	
B_{bg}	27,500 ± 249	0.91 %	

Table 12: Experimental data for the gold crescents.

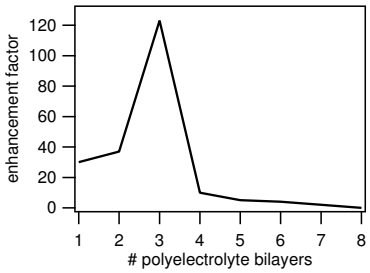

Figure 36: Fluorescence intensity of the dye Atto425 in dependence of the distance to gold crescent-shaped nanostructures.

number of polyelectrolyte bilayers	enhancement factor I_{enh}/I_{nonenh}
1	30.2
2	37.2
3	122.9
4	9.9
5	5.1
6	4.5
7	2.3
8	0.2

Table 13: Calculated fluorescence enhancement factors of gold crescents for different amounts of polyelectrolyte spacer bilayers.

For the gold crescent-shaped nanostructure, the maximum enhancement is observed at a distance of 12 nm (three polyelectrolyte bilayers). Here, a fluorescence enhancement factor of 123 for those dyes placed on the nanostructures compared to the dyes far away of the structure is found. This is a fourfold increased enhancement compared to the gold ellipses. These findings can be explained by theoretical calculations performed earlier which show that the electric near-field of gold crescents is approximately five times higher than the electrical near-field of gold ellipses. [76] The stronger near-field of the crescents causes a higher excitation rate of the dyes, leading to a higher fluorescence on gold crescents than on gold ellipses.

Although the strengths of the electrical near-fields of gold crescents and ellipses differ by a factor of 5, the fluorescence enhancement only reveal a difference of the factor 4. On the one hand, this discrepancy could arise due to the described quenching.

However, as the dye concentration in the polymer layer is very low, and the electrical near-field at the crescents' tips is extremely high, fast bleaching of the dye is an important issue. Recording a single two-photon excited fluorescence image already causes irreversible photodamage of the investigated area. Therefore, it is rather suggested that the mentioned discrepancy is caused by fast bleaching processes on the crescents' surface, leading to a lower fluorescence enhancement than theoretically predicted.

The further course of the graph shows a strong incline. Hence, the enhancement factors increase much stronger than those of the elliptical structures. This indicates a higher quenching effect than for elliptical structures, which overlays the enhancement process. Still, the gold crescents show a higher fluorescence enhancement for small distances than the gold ellipses at their maximum. Interestingly, the values decline fast with further distances. Nonetheless, they remain in a range comparable to the values of the elliptical structures at long distances.

Fig. 37 shows all enhancement factors of the gold and silver ellipses, and the gold crescent-shaped nanoparticles, obtained from the corrected emission values plotted against the distance between the dye and the different nanostructures investigated.

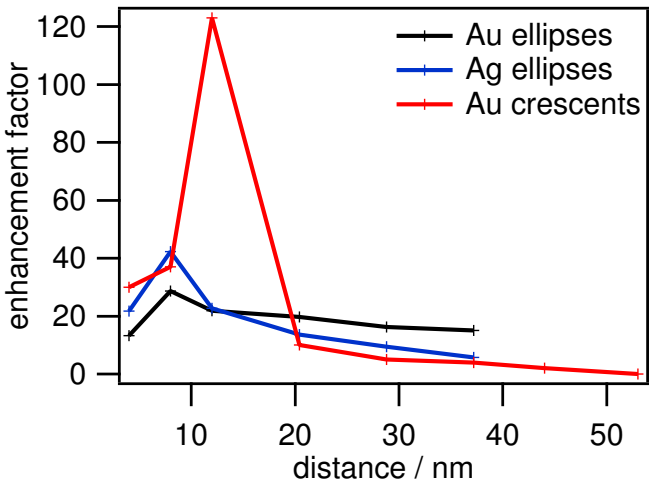

Figure 37: Fluorescence intensity of the dye Atto425 in dependence of the distance to gold and silver elliptic and gold crescent-shaped nanostructures.

All obtained enhancement factors are underestimated in double respect: first, the quenching is not taken into account and, second, for easier reference the whole surface areas of the structures are used for the calculations, although the electrical near-fields are confined to the edges of the structures.

5.3 Conclusions and Outlook

Plasmonic nanostructures with similar resonance frequencies are fabricated from two different materials (silver and gold). Thus, a direct quantitative comparison of the different effects on the two-photon excited fluorescence intensity of a dye in close proximity is feasible. Additionally, differently shaped nanostructures with the same resonance frequency but with distinct near-field enhancements are used in equivalent experimental setups. Hence, the effect of the material and of the shape of a nanostructure on the fluorescence enhancement is shown.
Gold elliptical nanostructures show the best fluorescence enhancement if the dye is placed in a distance of 8 nm to the metal. Here, the enhancement factor almost reaches the value 30. At short distances, no complete quenching is observed, but a mean enhancement. This alludes the existence of two competing processes: quenching and enhancement. Apparently, the enhancement is still dominating over the quenching, thus, leading to a net enhancement of the fluorescence.

Silver ellipses show best fluorescence enhancement at a distance of 8 nm, too. The overall enhancement factor is higher than for the gold equivalent and reaches the factor of 42 at the maximum. The course of the enhancement factors with respect to the distance is comparable to the gold ellipses, only being displaced to higher values. Again, no complete quenching of the fluorescence is observable at short distances, pointing to a superposition of quenching and enhancement processes. Additionally, lower autoluminescence of the silver is detected than for gold.

Gold crescents have a strong effect on the fluorescence. In spite of fast bleaching, still a maximum enhancement of 123 reached. This enhancement is found at a distance of 12 nm. The assumption that quenching and enhancement occur simultaneously is supported: for the nanocrescents with their sharp tips, the quenching effect is higher than for the elliptical structures due to the strongly confined electrical field. Thus, the maximum enhancement moves to a higher distance, where the quenching is negligible and the enhancement dominates.

It could be shown that the competing processes enhancement and quenching are both present at short separation distances between the dye and the metal. The enhancement is mainly caused by an increase of the excitation rate of the dye. The quenching mechanism, however, is based on non-radiative de-excitation of the dye molecules.

Overall, a detailed investigation of the effects of material and shape of the nanos-

tructure on the specific fluorescence enhancement is presented. It is shown that the maximum enhancement factors correlate with the strength of the electrical near-fields of the nanostructures.

Chapter 6

Near-Field mediated Fluorescence Correlation Spectroscopy

6.1 Introduction

Fluorescence correlation spectroscopy (FCS) is a powerful tool to investigate the diffusion of fluorescent species in various environments. [87] It is based on the measurement of the fluctuations of the fluorescence emitted by the tracer molecules passing through the observation volume. The method was first described and experimentally realized in the early seventies by Madge, Elson and Webb. [39–41] Amongst others, Madge et al. measured the diffusion coefficient of Rhodamine 6G in aqueous solution, yielding a value that is still accepted as standard and often used in FCS calibration experiments. This pioneer study led to intense research applying fluorescence correlation spectroscopy especially in biological systems. Initially, the main drawback was the poor signal-to-noise ratio due to low detection efficiency and insufficient background supression. These problems could be overcome by the introduction of confocal illumination and detection in fluorescence correlation spectroscopy by Rigler et al., leading to an enhanced efficiency of the FCS technique. [88]
In recent years, fluorescence correlation spectroscopy has experienced widespread applications in many research areas, especially in biology. The application of FCS to study cells even in vivo has given significant insight into cellular processes. [89–92] As generally all physical parameters that give rise to fluorescence fluctuations are accessible via FCS, it also became a powerful tool for physicists and material scientists. Conformation of polymers in different solvents [93,94], diffusion in polymer melts [95] or in cross-linked networks [96–99] could be exploited and became subjects of extensive investigations. Nowadays, fluorescence correlation spectroscopy is one of the standard tools for high-throughput screening due to its short data aquisition times combined with the straightforward analysis.

Only recently, the field of plasmonics was successfully adopted to fluorescence correlation spectroscopy, establishing the near-field FCS scheme. Estrada et al. used the electrical near-field of gold colloids to reduce the effective observation volume by four orders of magnitude. [100] A correlation of the dye Rose Bengal in a concentration of

150 µM using the near-field FCS setup was shown, which is a strong evidence for the proposed volume reduction.

This pioneer study of Estrada et al. suffers from some drawbacks. For easier theoretical modeling and analysis, they use spherical particles. Spherical particles, however, belong to the most unefficient nanoparticles in terms of strength of the electrical near-field. Moreover, metal nanoparticle colloidal suspensions often show high polydispersity and roughness due to the wet-chemical synthesis. This leads to different results for each particle. Third, gold often induces strong quenching of linearly excited fluorescence instead of an enhancement. This is dye-dependent and, thus, the method is not versatile for different systems.
In this chapter, an improved approach is introduced. The use of nanodisks instead of spherical particles with higher electrical near-fields should allow for slightly stronger effects. Using nanostructures fabricated by colloidal lithography, a defined geometry is obtained. Combined with the improved roughness, this should allow for reproducible results. By using silver instead of gold, the quenching should be overcome in the majority of cases. The following results are a first approach, serving as a proof of principle.

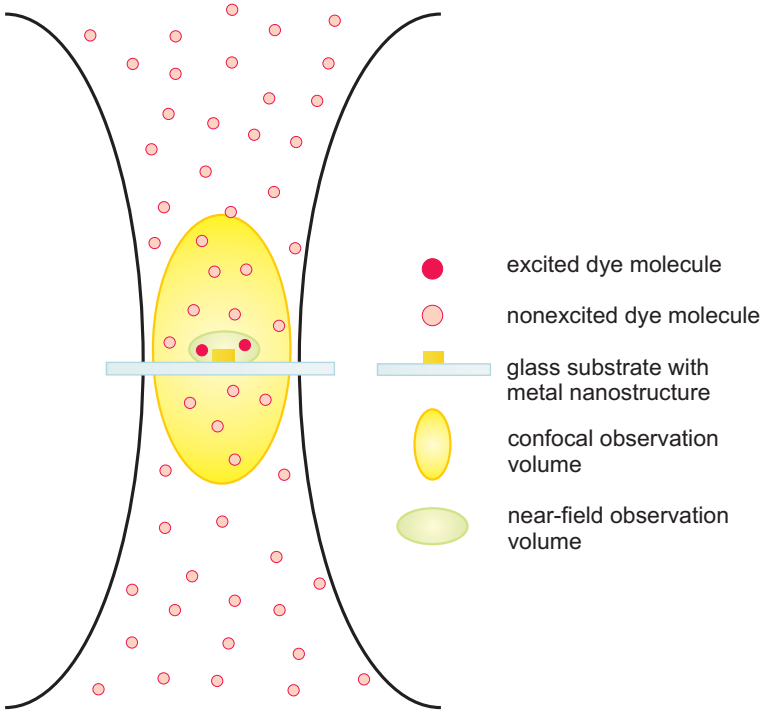

Figure 38: Schematic illustration of the effective observation volume in near-field fluorescence correlation spectroscopy.

Fig. 38 is a schematic illustration of the confocal near-field FCS model. The focused light beam in combination with a confocal pinhole gives rise to a ellipsoidal confocal

volume (yellow). A glass-supported plasmonic nanostructure (blue) is placed in the focus. Excitation of the plasmon resonance leads to a new effective observation volume (green), which corresponds to the electrical near-field of the nanostructure. Hence, at low excitation intensities, the dominating part of the fluorescence signal originates from the near-field volume (at best, only the dye molecules (red circles) in the near-field observation volume would be excited and fluoresce (filled red circles)).

6.2 Results and Discussion

Silver disks with an average lateral diameter of 100 nm were prepared by colloidal lithography as described in Chapter 3.1.1 (p. 19). Due to the symmetric shape, the disks exhibit one resonance upon irradiation. It is found to be at λ=494 nm in air with UV/vis spectroscopy (Fig. 39).

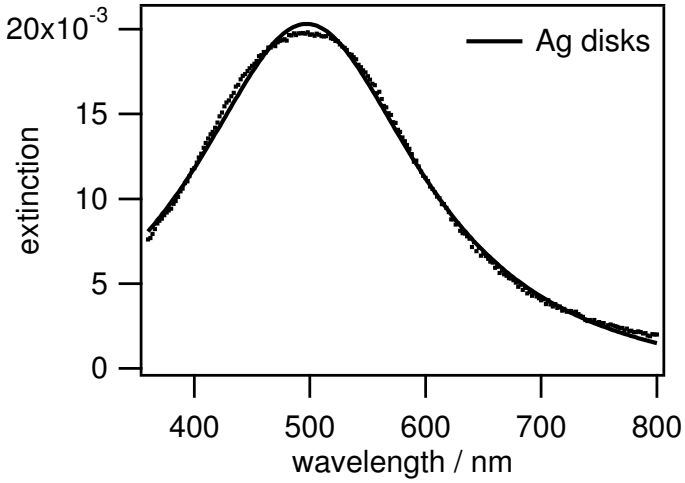

Figure 39: Extinction spectrum of silver disks at air with a Lorentzian fit (black curve).

The commercially available fluorophore Alexa488 was chosen, as it is soluble in aqueous solutions, and exhibits a high stability. Furthermore, it offers a high fluorescence quantum yield.

As the diffusion time of Alexa488 in pure water is too short to examine any possible effects at short timescales caused by the nanostructure, solvents with higher viscosities were applied. The use of aqueous glycerol solutions slows down the diffustion of the dye, which allows to see short timescale effects more pronounced.

Fluorescence correlation spectroscopy of the dye Alexa488 is measured on the surface of the substrate according to the procedure explained in Chapter 3.7 (p. 28). The

dye is dissolved in two aqueous solutions containing 30 vol. % and 80 vol. % glycerol, respectively. The dye concentration is 24 nM in both cases.
Since the measurements were recorded at the surface, the signals comprise a high amount of reflections of the excitation light. To achieve reasonable correlations, the curves have been corrected prior to analysis. By applying a pulsed excitation laser and time-correlated single photon counting, the fluorescence can be separated from the reflected light and other possible background noise. This procedure was perfomed using the software SymPhoTime®. However, this method of course leads to lower effective countrates, as a major part of the signal is eliminated.

The correlation curves at the glass interface of the dye without nanostructure serve as references. Fig. 40 a. shows the normalized autocorrelation curves of the dye Alexa488 in a 30 % glycerol solution, measured in the solution (red curve), and on the glass interface (black curve). The curves resemble each other. The slight discrepancies may arose from marginal different diffusion behavior, or, most likely, the occur due to the fact that on the glass surface, the effective excitation volume is not Gaussian, but still it is fitted with the very same fit function as the curve recorded in solution.
Fig. 40 b. shows the normalized autocorrelation curves of the dye Alexa488 on a glass surface covered with a 30 % and an 80 % glycerol solution, respectively. The curve for the 80 % glycerol solution is shifted to longer timescales compared to the curve for the 30 % glycerol solution. Hence, the diffusion of the dye in the lower concentrated glycerol solution is clearly faster. This is a result of the higher viscosity of the glycerol compared to water.

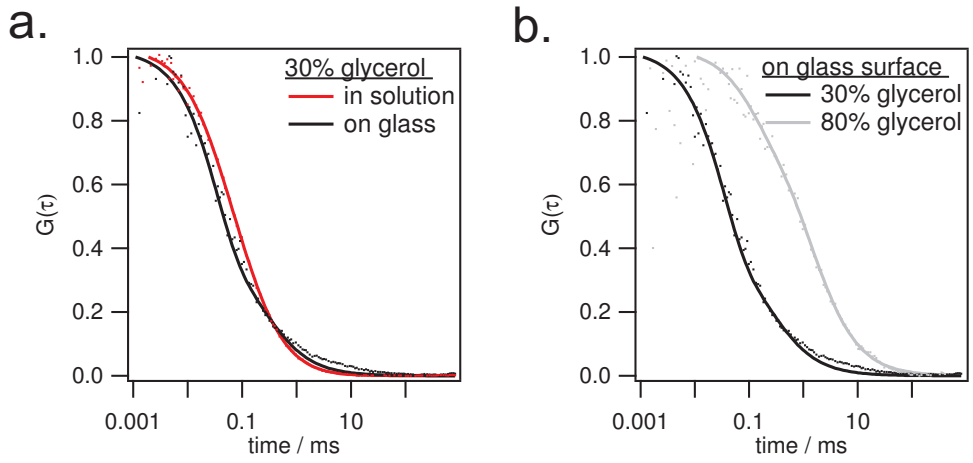

Figure 40: a. Autocorrelation curves of Alexa488 in 30 % glycerol in solution and on the glass surface. b. Autocorrelation curves of Alexa488 in 30 % and in 80 % glycerol on the glass substrate. The dots represent the experimentally obtained data, the lines the corresponding fits.

6.2.1 Alexa488 in a 30 % aqueous glycerol solution

Fig. 41 shows the lifetime-corrected autocorrelation curve of the dye in 30 % glycerol. The green curve represents the measurement recorded on the glass surface without nanostructure, while the blue one has been recorded on a silver disk. The blue curve is shifted to shorter timescales compared to the green curve.

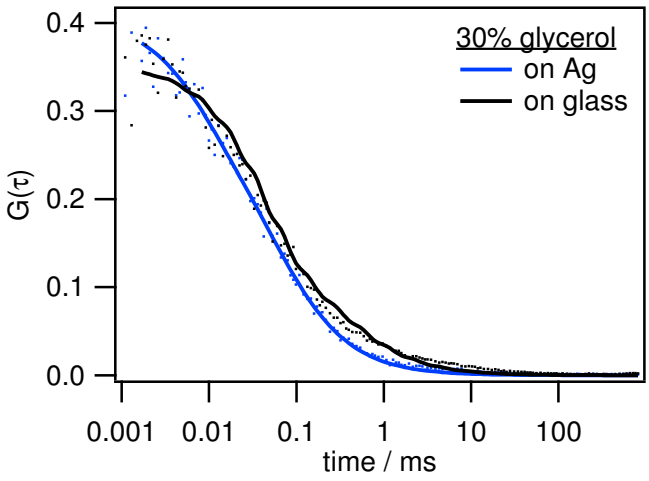

Figure 41: Autocorrelation curves of the dye Alexa488 in 30 % glycerol on a silver disk and on glass. The dots represent the experimental data, the lines the according fits.

Both measurements were recorded on the same sample, hence, the concentration of both the dye and the glycerol content are identical. Since no further changes in the system were carried out prior measuring on the silver disk, there are two possible reasons for the observed shift.

First, a changed diffusion coefficient is conceivable. In liquids, the diffusion coefficient is given by the Stokes-Einstein relation.[xx] As neither the temperature, nor the viscosity, nor the hydrodynamic radius should be affected by any changes, it is unlikely that the diffusion coefficient underlies a modification. If due to the presence of the metal adsorbing processes arise, this would become apparent in two different diffusion times in the fit. As this is not the case for the presented experiments, this effect is neglected, and a constant diffusion time is assumed.

Thus, it is more likely that another mechanism is the reason for the shift of the curves. This could be a change in the effective size of the observation volume. If the volume is smaller, the fluorescent particles need less time to cross it, hence, the correlation time is shifted to shorter times. This effect can be adopted very well to the applied system,

[xx] $D = \frac{k_B T}{6\pi \eta R_0}$, with the diffusion coefficient D, the Boltzman constant k_B, the temperature T, the viscosity of the solvent η, and the hydrodynamic radius R_0.

as the electrical near-field of the silver disks may reduce the observation volume as depicted in Fig. 38. Therefore, this assertion is adopted to explain the observed shifts in the correlation times.

The nanodisks' plasmon resonance is excited by the incident laser. Hence, an electrical near-field is formed around the nanostructure. If one assumes that the electrical near-field laterally extends over the whole nanostructure (100 nm), and that it extents 50 nm in z-direction, a near-field volume of 0.003 µm^3 is calculated. These assumptions are crude approximations and definitively overestimate the extension of the near-field, especially in lateral dimensions. Nevertheless, the resulting observation volume is already in the attoliter regime. The inherent confocal volume of the microscope with lateral dimensions of approximately 250 nm, and a z-component of 2 µm, yields an observation volume of approximately 0.696 µm^3. Since the experiments are performed at the surface, only half of the ellipsoidal volume is taken into account. This leads to an effective confocal observation volume of 0.348 µm^3. Assumed that in presence of the electrical near-field the excitation is enhanced, and, thus, most excitation processes occur in the near-field regime, the effective observation volume is strongly reduced by more than two orders of magnitude.
However, it should be kept in mind that there exists also a low contribution of those dye molecules inside the confocal volume to the fluorescence signal.

The curves have been fitted with a single diffusing component using the fit function given in Chapter 2.4 (p. 15). The fits in Fig. 41 appear appropriate at first sight, but upon a closer look, some difficulties with the standard fitting method arise.
The confocal observation volume on the surface of the substrate is only half of the complete observation volume when measured in solution. Hence, only the dyes in the upper part of the confocal observation volume depicted in Fig. 38 can be excited. Nevertheless, the shape corresponds to a Gaussian profile, and as in FCS the main contribution is the lateral diffusion, it can be fitted with the standard Gaussian correlation function. The fit including the triplet state yields a diffusion time of 0.05 ms.

The shape of the electrical near-field differs from a Gaussian profile. Without including the triplet state, however, the fit seems to be reasonable, yielding a diffusion time of 0.02 ms. Thus, the diffusion time is reduced by more than half with respect to the value obtained without nanostructure.
Although a detailed investigation of the process requires a modulated correlation function, the presented results indicate the validity of the proposed excitation model.

6.2.2 Alexa488 in an 80 % aqueous glycerol solution

Fig. 42 shows the autocorrelation curves of Alexa488 in 80 % glycerol on the glass and on a silver disk. Again, shorter diffusion times can be observed on the silver disks.

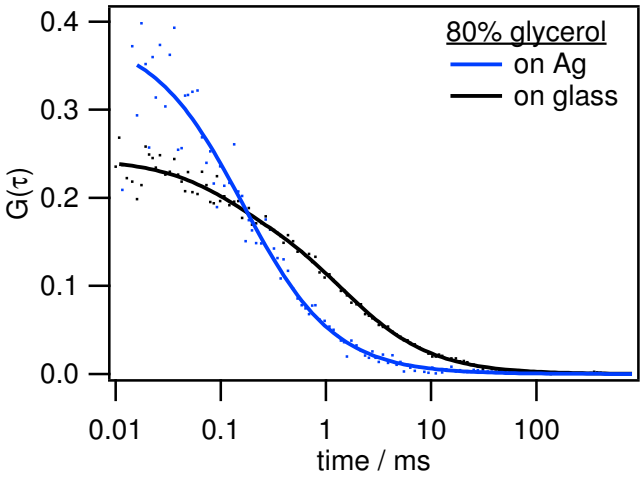

Figure 42: Autocorrelation curves of the dye Alexa488 in 80 % glycerol on a silver disk and on glass. The dots represent the experimental data, the lines the according fits.

The fit on the glass surface yields a correlation time of 1.34 ms. The fitting on the nanostructure results in a diffusion time of 0.162 ms ± 0.210 ms. As the applied model for the fit is not appropriate for the investigated system, these values are not exact and can only offer comparative statements. Nonetheless, the graphs as well as the fitting results illustrate the trend towards shorter correlation times in close proximity of a silver nanodisk. As explained in the previous section, this is a strong hint for the reduction of the observation volume.

6.3 Conclusions and Outlook

It has been shown that the observation volume for fluorescence correlation spectroscopy can be drastically reduced by performing the measurements in the near-field regime of plasmonic nanostructures. This offers the opportunity to measure at higher concentrations, or to observe events on a single molecule level like for example protein binding processes.

However, to ensure that the investigated processes are not affected by the presence of the metal, a protecting layer would be beneficial. The nanostructured surface could

for example be covered with a silicium dioxide layer of approximately 10 nm thickness. Like this, the fluorophores would perceive a glass-like surface everywhere on the sample. Nevertheless, the dye molecules would still experience the strength of the electrical near-field of the nanostructures, as the decay length is clearly higher. Additionally, this procedure would most likely suppress many undesired quenching processes, as there is no direct contact between the fluorophores and the metal.

Nonetheless, to obtain quantitative information, a detailed investigation of the underlying mechanisms requires an adjusted correlation function which considers an adequate shape of the observation volume.

Chapter 7

Plasmon Hybridization in Stacked Double Crescents

7.1 Introduction

Interparticle coupling typically leads to energy shifts and splitting into degenerate modes. [101] This effect has been shown for regularly ordered arrays of nanoparticles, [102] which can be used as efficient substrates for surface enhanced Raman spectroscopy. [103,104] Recently, these structures have been termed metamaterials, as they can occupy unique properties not occuring in nature; the most prominent example is certainly negative refraction. [105,106] The possibility of negative refraction indeces has been anticipated by Veselago long before the actual realization of such structures.
It has been shown that split-ring resonators are functional building blocks to fabricate such metamaterials. This can be explained by the excitation of a circulating current in the structures induced by the incident light, leading to local magnetic dipole moments. These local fields can antagonize the magnetic field of the exciting light, thus leading to negative permeability, which is one prerequisite for negative refraction besides negative permittivity. [106–108] Major efforts have been ventured to design efficient nanostructures in two and three dimensions, mainly applying electron beam lithography and focused ion beam milling. Hence, effective metamaterials have been produced showing negative refraction at different wavelengths approaching the visible regime. [4,105,109–112]

However, the employed methods hold certain drawbacks that inhibit extensive applications, both in industry and in academic research. First, expensive equipment is necessary which is not readily available at every facility. Second, the patterning of large areas is almost impossible due to time-consuming fabrication steps. And, finally, the quality of the noble metals used is reduced due to contaminations enriched during the process. As the optical properties of the structures strongly depend on their composition, contaminations generally compromise their quality as well as their reproducibility for different batches.

The application of nanosphere lithography exhibits a simple, yet powerful alternative for the fabrication of nanostructures. Although the use of colloids limits the variety of possible shapes, it overcomes the above described problems of serial processing.

Nonetheless, a huge variety of sophisticated processes has been established allowing fabrication of complex structures such as nanotriangles [113–115], disks [42], rings [101], and crescents [43,116]. The latter occupy multiple resonances [43,86] and can thus be considered as an equivalent to split-ring resonators. Without expensive equipment, large areas can be structured quickly with the parallel nanosphere lithography process. Moreover, the noble metals are deposited by vacuum evaporation, thus, contaminations can be reduced to a minimum level.

Stacking crescent-shaped nanoparticles with an insulating material between the layers has been realized by Retsch et al., however, only the mutual orientation of the crescents could be controlled. [117] Here, the precise vertical alignment with respect to the underlying layer using a colloidal lithography approach is presented. The three-dimensional alignment in combination with short separation distances introduce intriguing changes in the optical spectra, alluding a strong coupling between the structures. A theoretical plasmon hybridization model has been established to explain analog effects for nanoparticle dimers, and recently, it has been adapted to split-ring resonators to describe the fundamental plasmon mode. Here, a complete analysis of all plasmon resonances is presented. This gives insight into the entire coupling process and leads to a fundamental understanding of the interaction between individual nanoparticles.

7.2 Results and Discussion

The described fabrication technique leads to the formation of densely packed layers of metal nanocrescents, bringing the tips in close proximity without allowing any contact due to the integrated silicon dioxide separation layer. Fig. 43 shows a scanning electron microscope image during the fabrication process. The upper row shows top- and side-views of the sample after the first gold deposition. In a., the colloids have already been detached, whereas in b. they are still visible. The bottom row shows top- and side-view images of the complete stacked double crescent structures. The red arrows indicate the separating silicium dioxide layer between the metal layers. This perfect vertical alignment leads to strong interparticle coupling of the individual resonators.

To understand the optical properties of the stacked double crescents, UV/vis-NIR spectroscopy, using linearly polarized light, was applied. Fig. 44 shows the extinction spectra of single and double crescents, both spatially separated and in arrays. In accordance with literature, the resonances will be termed U and C, depending on the polarization of the incident light (Fig. 45 a.).

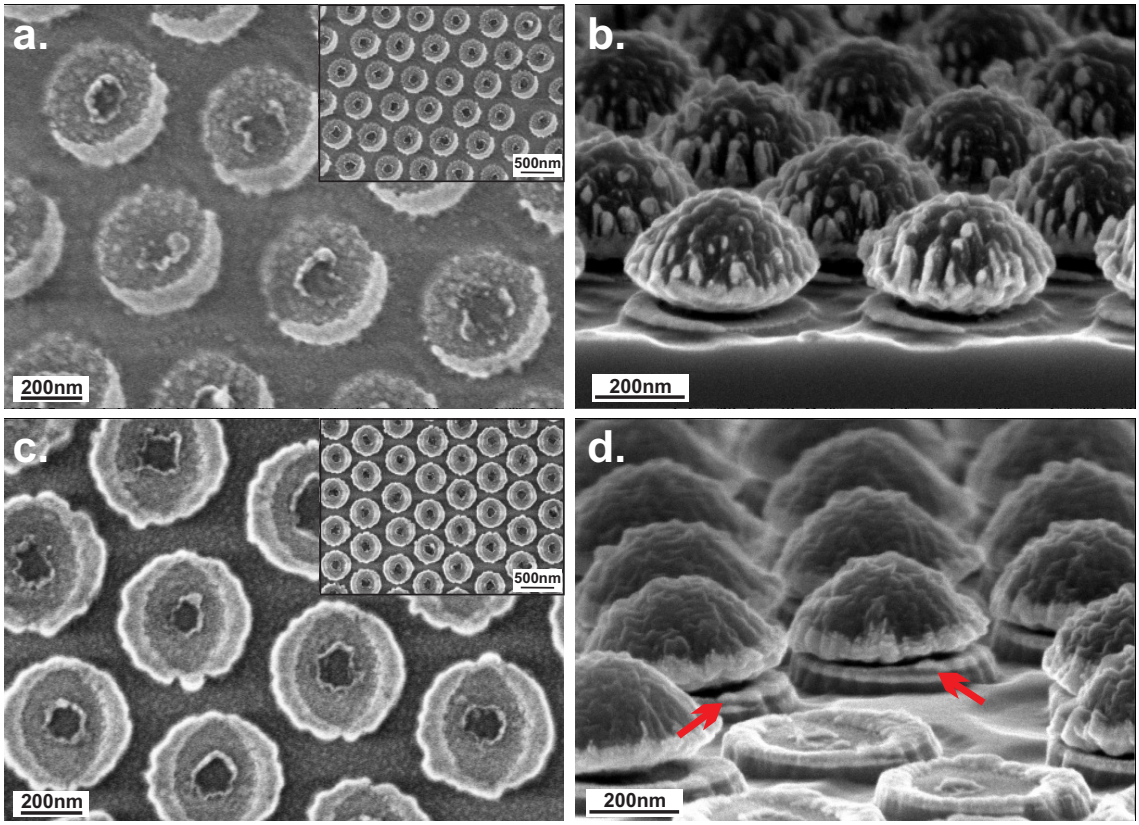

Figure 43: Scanning electron image of stacked double crescents during the fabrication process. Top row: single crescent structures (a. top-view, b. side-view, with colloids), bottom row: stacked double crescent structures (a. top-view, b. side-view). The black arrows highlight the separating layer of silicum dioxide between the two individual crescents.

Fig. 44 a. shows the characteristic resonances of spatially separated single crescents. In C-polarization, the main resonance appears at 2460 nm which is attributed to the fundamental plasmon mode (C1). In U-polarization, a resonance at 1446 nm is visible, attributed to the first harmonic (U1). In both spectra, however, a peak at 658 nm arises. This corresponds to the balk resonance, earlier termed pp for particle plasmon, as it roughly matches the resonance observed for small gold particles.

The stacked double crescents show a peak at 2004 nm in C-polarization, being blueshifted by approximately 450 nm compared to the single crescents. U-polarization reveals a resonance at 2324 nm, being 850 nm redshifted with regard to the single structures. In total, the energetic order of the resonances is inverted compared to the parent resonances of the single crescents.

The spectra of the arrays resemble those of the spatially separated objects. The main optical properties are retained, including the resonance shift upon introduction of the second crescents. Nevertheless, these shifts are smaller than those of the separated particles. This fact could be due to slight differences in the thickness of the interme-

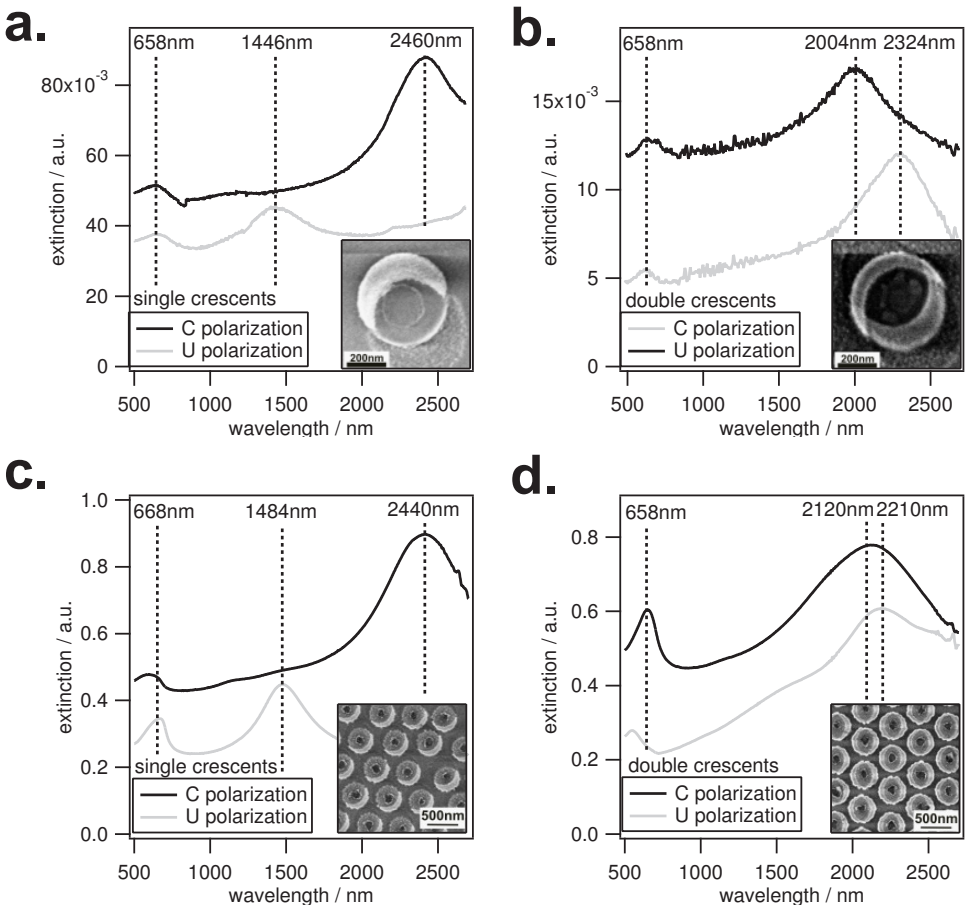

Figure 44: Polarization-dependent extinction spectra of single and double crescent structures. Top row: spatially separated single (a.) and double crescent (b.) structures, bottom row: arrays of single (c.) and double crescent (d.) structures.

diate silicon dioxide layer. The broadening of the peaks in the spectra of the arrays is assigned to an increased inhomogeneity introduced in the shrinking process of the colloidal mask. The extinction is significantly higher for the arrays, reflecting the higher surface coverage.

The striking differences in the optical properties of the single and the double crescents can be understood from plasmon hybridization theory. The plasmon resonances of the individual nanostructures undergo a coupling process when brought in close proximity to each other. Hence, the superpositions of the original resonances give rise to new resonances. This model can be understood as an electromagnetic analog to molecular orbital theory, where the wavefunctions of the individual atoms overlap in a molecule, forming a binding and an antibinding molecular orbital. Here, the two resonators are equivalent to the atoms, forming together a "plasmonic molecule".
The formation of the hybridization modes for both resonances is shown in Fig. 45. In both cases, a symmetric mode, C+ and U+, respectively, and an antisymmetric mode,

C- and U-, arise. The symmetric mode shows an in-phase oscillation of the two crescents, the antisymmetric one an out-of-phase oscillation. The energy of the symmetric mode is elevated compared to the initial energy level, whereas the latter is lowered.
In C-polarization, the symmetric hybrid mode C+ possesses an enhanced dipole moment compared to the single crescents. Consequently, it can be detected in the optical spectrum. As the C+ mode is higher in energy than the single mode, the resonance appears blueshifted. The C- mode, however, leads to an electric field distribution with no effective net dipole, representing a so-called dark mode, as it cannot be excited by the external field and, thus, does not appear in the spectrum.
In U-polarization, the situation is inverted due to the different symmetry of the U1 mode. Here, the U+ mode does not show a net dipole and does not appear in the spectrum. But the antisymmetric mode does feature an electric dipole and can thus be excited by the U-polarized light. For the energy level being lower, the resonance is redshifted with respect to the single mode. The coupling efficiency is sufficiently strong to induce a crossover of the plasmon resonances leading to an inverted energy landscape.
The experimental data support the theory of the hybridization model. Moreover, it is in good agreement with investigations on double split ring resonators fabricated by electron beam lithography, where plasmon hybridization was observed for the fundamental mode of the split-rings.

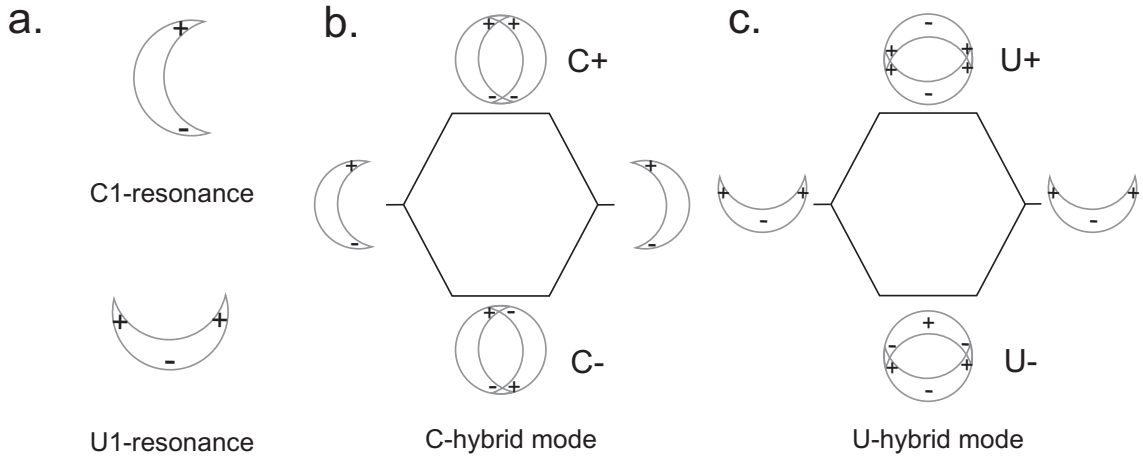

Figure 45: a. Schematic illustration of the C- and U-resonance. Coupling schemes for C-resonance (b.), and for U-resonance (c.).

To demonstrate the double crescents being separated indeed, connected crescents forming ring-like structures were prepared and investigated in terms of their optical properties. Fig. 46 shows the UV/vis-NIR spectra of the rings.

Two resonances are excited, one at 692 nm, the other one at 2436 nm, none of them dependent on the polarization of the incident light. This reflects the symmetry of the

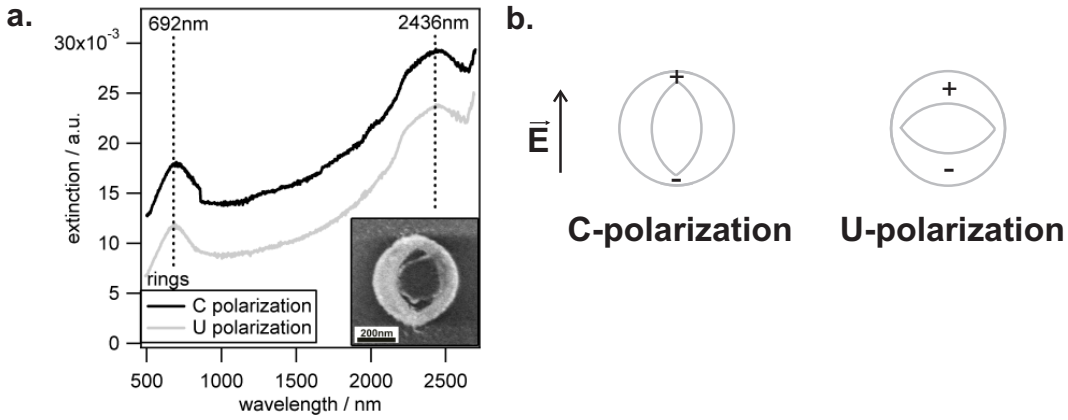

Figure 46: a. Plasmon resonances of rings. b. Charge distribution of both resonances.

ring structure. The peak at 2436 nm is ascribed to the fundamental ring resonance (Fig. 46 b.). The high energy peak at 692 nm is assigned to the pp-resonance perpendicular to the ring contour. As the spectra differ fundamentally from those of the double crescents, it is obvious that in the latter the tips are not connected. This finding is in good agreement to the scanning electron microscope characterization discussed above.

7.3 Theoretical evaluation

Computer simulations of single and double crescents were performed to validate the obtained experimental data.[xxi] For the simulations the code JCMwave was used, which is based on a finite element method. The geometries of the different structures were captured from the electron microscope images.

7.3.1 Optical properties of the C1 and the U1 modes

Fig. 47 shows the simulated extinction spectra for single and double crescents in C- and U-polarization. The single structures show three resonances in C-polarization. The C1 mode appears at 2176 nm, resembling the experimental value with a blueshift of 200 nm. Furthermore, the C2-resonance is visible at 960 nm. This mode is not resolved experimentally, most likely due to insufficient intensity. Lastly, the pp mode emerges at 550 nm. In U-polarization the single crescents show the U1-resonance at 1265 nm, which is blueshifted by 200 nm compared to the experimental data.
The spectrum of the double crescents in C-polarization feature one peak at 1690 nm,

[xxi] All theoretical simulations presented in this chapter were performed by XXX.

being blueshifted by 300 nm compared to the experiment. This peak corresponds to the hybrid C+ mode. It is strongly blueshifted compared to the simulated C1-resonance of the single crescent. Hence, the plasmon hybridization model is supported.
A shoulder at 910 nm indicates the presence of the hybrid analog of the C2-resonance. The behavior of this mode is discussed in detail further below.
In U-polarization, the double crescents hold one resonance at 1750 nm, a value that is again blueshifted in comparison to the experimental findings. Again, the simulations support the hybridization model as it reveals the hybrid resonance U- redshifted with regard to the simulation of the single reference. Furthermore, the experimentally observed crossover of the two fundamental resonances is also realized in the simulations.

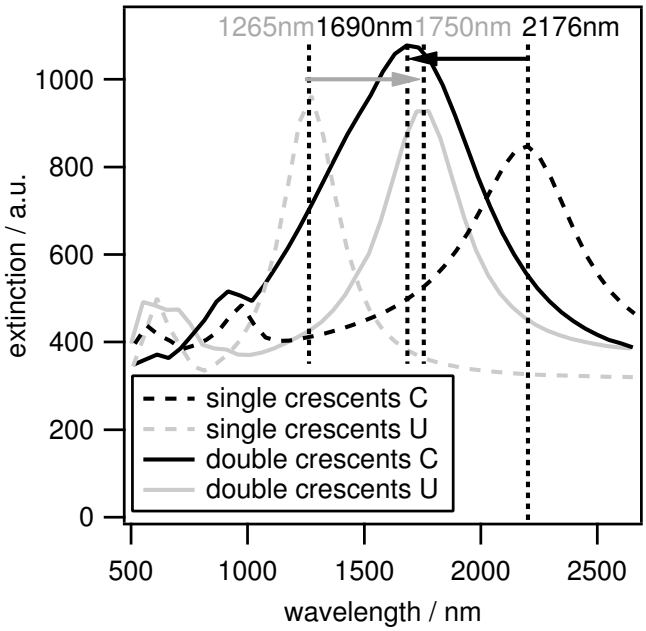

Figure 47: Simulated extinction spectra for single and stacked double crescents.

Altogether, the simulated shifts of the resonances are in good agreement with the experimental findings. The quantitative blueshift of the simulated spectra compared to the measured data are ascribed to the following differences: First, roughness in the structures can cause significant shifts in the plasmon resonances. [118,119] Second, the determination of the exact geometry of the double crescent structure is difficult as the bottom crescent is partially hidden by the top crescent. This also holds for the thickness of the gold and silicon dioxide layers. Additionally, both the gold and the silicon dioxide layer diminish towards the wings and tips as they follow the shape of the colloid. This was not taken into account for the simulation. Adapting more precise models for the crescents, such as gold and silicon dioxide layers with non-constant thicknesses, the quantitative agreement between simulation and experiment could be improved.

Lastly, no refinements of the simulation parameters, e.g. for the gold permittivity, were performed, as the simulations reflect all essential features of the experimental data.

7.3.2 Optical properties of the C2 mode

The C2-resonance only appears in the calculated spectra, hence, it was examined in further detail by means of simulations. The C2-resonance occupies a charge distribution with two nodes (Fig. 50 c.). Upon hybridization, the mode splits up into a symmetric and an antisymmetric one, C2+ and C2-, respectively. Only the C2+ mode shows a net dipole moment which can be excited by the external field. As it is higher in energy than the parent resonance, it appears blueshifted in comparison to the single crescents' resonances.
Interestingly, this hybrid C2+ mode is strongly dependent on the overlap of the two crescents, whereas both the C1 and the U1 mode are not affected. The spectra have been simulated for overlaps of 40 nm and 120 nm and are plotted in Fig. 48 (the overlap of 40 nm corresponds to the data depicted in Fig. 47).

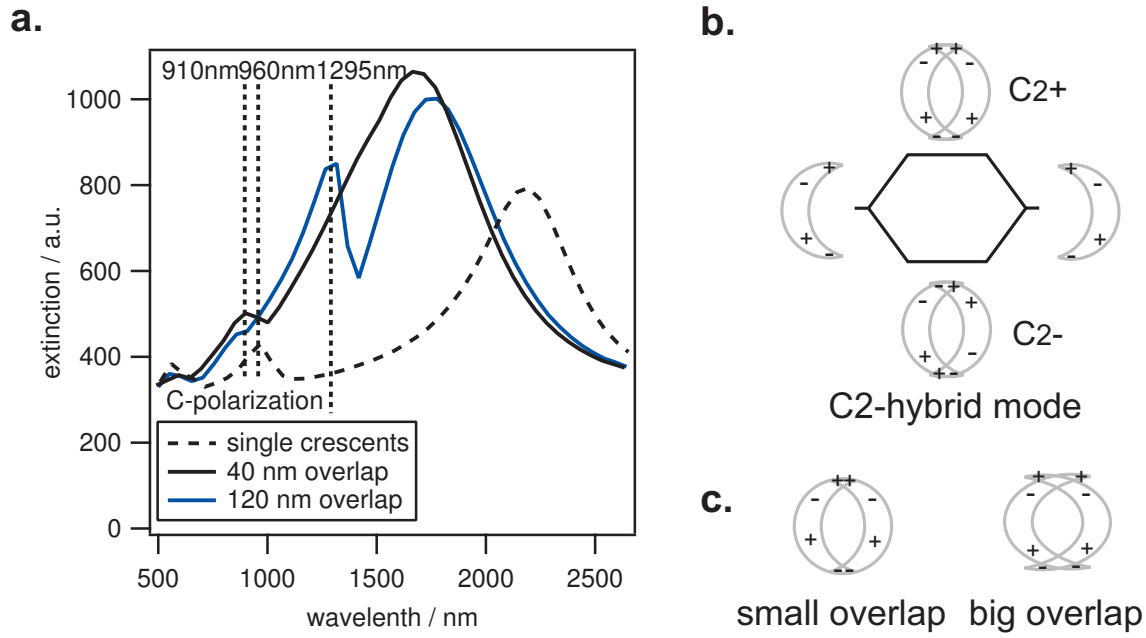

Figure 48: Hybrid plasmon mode arising from coupling of the C2-resonance. a. Simulated spectra of stacked double crescents with varying overlap region. b. Model of plasmon hybridization for the C2-resonance. Linear superposition of the resonances lead to two hybrid modes termed C2+ and C2- with C2+ being higher in energy. c. Schematic representations of the charge distribution of the C2+ mode for a small and a big overlap of the crescents.

For an overlap of 40 nm, the peak shifts from 960 nm to 910 nm upon hybridization.

However, if the overlap region is increased to 120 nm, a strong redshift is observed, resulting in a peak at 1295 nm. Remarkably, the different overlap distances cause shifts in opposite directions. As a redshift indicates a decrease in energy, it is proposed that with increasing overlap the tip charges cross the first node and get closer to the region with opposite charges located in the wings of the crescents (Fig. 48 c.). The C1 mode, however, does not possess any charges in the wings and, hence, does not show different spectra upon variations of the overlap.
As the U1 mode does not possess any charges in the wings either, it is also not sensitive to changes in the overlap of the tips (Fig. 49).

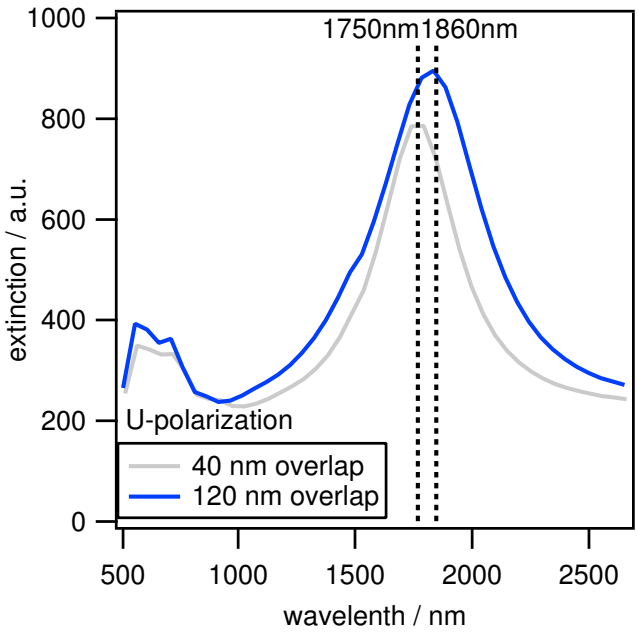

Figure 49: Effect of crescent overlap on the resonance excited in U-polarization.

7.3.3 Illustrations of the electrical near-fields

A mapping of the electrical near-field was performed to gain knowledge about the charge distributions of the double crescents for the distinct hybridization modes (Fig. 50).

The upper part of Fig. 50 shows the field distribution for the C+, the U-, and the C2+ modes in the xy-plane, cut through the dimer center. Essentially, the charge distribution behaves as predicted by the hybridization model (Fig. 44 e. and f.). The lower part illustrates a cut through the xz-plane at the gaps between the tips (the plane is indicated by the dotted line in the upper images). In the C+ mode, a strong field can be observed in the tip region, representing areas with higher electron density as

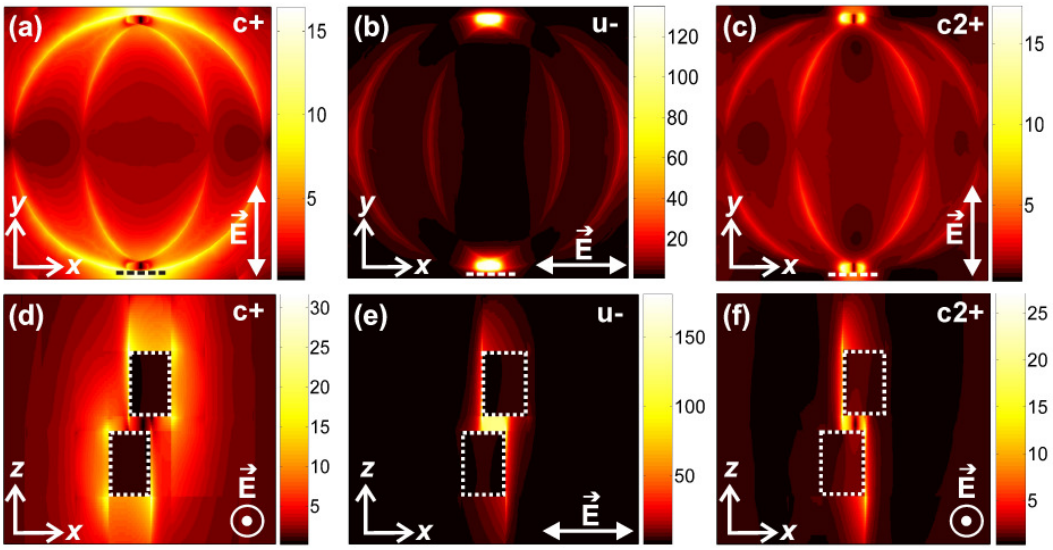

Figure 50: Near-field distributions of the stacked double crescents at the resonance wavelengths. Top row: electrical near-fields in the xy-plane through the middle of the silicium dioxide layer separating the two crescents (the cutting plane is indicated by the dotted line). Bottom row: electrical near-fields in the xz-plane, cutting the structure in the tip region (the tips are encircled with a dotted line for better visibility).

predicted by the hybridization model. The node in the middle of the two crescents is also visible. In the gap between the tips, no field is existent as the tips have the same charge. As postulated by the hybridization theory, the U- mode shows a high field enhancement at the tips of the crescents, as well as a minor enhancement in the center of the structure. At the wings, the field diminishes, indicating the existence of the two nodes of the wavefunction. In the gap between the tips a strong field enhancement is visible, which is due to the opposite charges of the two tips.
For the C2+ mode, the xy-cut reveals a field distribution with three nodes. In the middle of the gap, no electrical field is present, reflecting the similar charges at the tips. However, an enhancement of the field is visible at the edges of the gap. This visualizes the proximity of the tip charges to the opposite charges at the wings of the crescents. Thus, the suggested model for the C2-resonance is supported by the simulations.

7.4 Conclusions and Outlook

A novel technique to fabricate vertically aligned quasi three dimensional stacked double crescents using a sophisticated colloidal lithography approach is introduced. The nanoscale objects are precisely arranged on the nanometer scale, providing access to

the understanding of fundamental aspects regarding the coupling process between the interacting nanostructures. Polarization-dependent UV/vis-NIR spectroscopy was used to reveal the influence of the second crescent in close proximity on the optical properties. The presence of the second structure caused a blueshift of the fundamental plasmon mode, as well as a significant redshift of the first harmonic mode. These effects even led to an inversion of the two resonances. Plasmon hybridization theory was applied to explain the striking differences in the resonance positions. Symmetry considerations showed that for each polarization only one of the formed hybrid nodes has a net dipole leading to a visible signal in the extinction spectrum. The symmetry situation is reversed for the two resonances, thus, the different directions of the shifts are readily explained. Computational simulations reproduce all essential optical features, supporting the plasmon hybridization model.

The established fabrication process allows for parallel and cheap patterning of large areas. Several parameters can be used to vary the resulting structures and, thus, their inherent resonance frequencies. By choosing different sized colloids, distinct sizes of the nanostructures can be obtained. In the case of the arrays, the etching degree can be increased to adjust the lattice spacing in the non-close-packed monolayer. Moreover, the separation distance given by the height of the silicon dioxide layer permits finetuning of the coupling efficiency and, thus, gives access to tailor-made plasmon resonances. The overlap of the two crescents can be tuned with the evaporation angle of the gold. Finally, different symmetries can be realized by changing the azimuthal angle used for the second gold evaporation. Here, an angle of 180° is realized.
The resulting structures show drastic differences in their optical spectra compared to their single analogs due to the strong coupling interaction between the tips. Furthermore, the symmetry of the structures gives rise to so-called dark modes, i.e. resonances without a dipole moment. These dark modes can be used for negative refraction materials, as they occupy negative values for the permeability.

The tuning possibilities cease in the three dimensional space. This restriction arises from the use of colloids for the nanostructure fabrication, as they provide limited space in their shadow region. Thus, the stacking of multiple nanostructures is hindered and can only be achieved with bigger colloids. Sacrificing extended three dimensional design, perfect vertically aligned nanostructures are attained, a feature not yet accomplished by colloidal lithography. The obtained structures are valuable as "plasmonic molecules" and, moreover, hold great promise for application as novel metamaterials.

Chapter 8

Sophisticated Nanolithography – Opposing Double Crescents with Tuneable Resonances

8.1 Introduction

The field of plasmonics has experienced significant progress during the last years. A big variety of nanostructures has been synthesized, starting from cubes, [120] over rods, [77] up to star-like particles produced by a wet-chemical approach, [121,122] or crescent-shaped structures obtained by colloidal lithography [43]. These structures have been extensively studied with regard to the tunability of their inherent plasmon resonances. As these resonances crucially depend on the particle size, shape, and the dielectric environment, they can be easily tuned by slight variations of these parameters. Nowadays, size adjustments and tuning the dielectric environment can be performed straightforward. [123–129] Due to the variety of available nanoparticle shapes, resonances in a broad spectral range can be achieved. [4] However, the response of metal nanoparticles upon minute shape modifications has only been analyzed in selected publications. In [86] for example, the plasmon resonance of crescent-shaped nanoparticles in course of crescent opening was investigated.

Nowadays, nanotechnology heads towards building more and more sophisticated nanostructures like for example core-shell particles [130,131] or stacked layers of nanostructures [117,132,133]. Especially quasi three-dimensional nanostructures could only be produced by techniques such as electron beam lithography or focused ion beam milling for a long time. These processes hold several drawbacks, amongst them the high costs associated with the equipment for the aforementioned techniques, the lack of a fast parallel process, as well as the comparatively low quality of the noble metals employed due to contaminations. As the optical properties of the nanostructures strongly depend on their composition, high quality compounds are desirable.

In the previous chapter, it has been shown that stacked double crescent structures can also be obtained by colloidal lithography, a technique that overcomes the disadvantages listed above. The main idea that makes colloidal lithography a powerful tool to synthesize sophisticated structures is to use one colloid for multiple manufacturing steps.

In the first part of this chapter, a modified fabrication process for crescent-shaped nanoparticles is established. This novel technique allows for precise shape-induced tuning of the plasmon frequency. It furthermore leads to an extended understanding of plasmon resonances.

In the second part of this chapter, a similar method as described in Chapter 7 is applied to obtain opposing double crescent structures in one layer, with the tips facing each other. The close proximity of the crescents' tips leads to an overlap of the electrical near-fields excited in the structures. This overlap causes denaturation of the plasmon modes which becomes evident in dramatic changes in the optical resonances. This behavior has first been observed and explained by Nordlander et al. for the fundamental plasmon modes. [134] In Chapter 7, the model has been extended to higher harmonics. Here, shifts due to shape-induced effects and coupling processes overlap. It is shown how these parameters can be separated and used for precise control over the plasmon resonance.

8.2 Results and Discussion[xxii]

8.2.1 Tuning resonances of single crescent-shaped nanoparticles

A novel technique to fabricate crescent-shaped nanoparticles has been established. This method allows for precise control over the resonance frequency of the structure, as it holds tuneable parameters which can be adjusted accordingly.

As explained in Chapter 7, the crescent nanostructures support multiple resonances upon irradiation, corresponding to the excitation parallel and perpendicular to the crescents' axes. In the following, they will be termed U- and C-resonance, respectively, due to their shape with regard to the external electrical field (Fig. 51 f.), analog to [85,86,135]. They can be measured with UV/vis-NIR spectroscopy. Fig. 51 shows the polarization-dependent extinction spectra of five different single crescent structures, prepared with different etching angles (45° to 65° tilting relative to the ion source; see Chapter 3.1.6, p. 22, for details of the fabrication procedure). The insets show the particular scanning electron microscope images.[xxiii] The black curves represent the C-polarized spectra, whereas the gray ones correspond to U-polarization.

Obviously, the U-resonance undergoes a redshift of approximately 775 nm with

[xxii] The experiments shown in this chapter were done in cooperation with XXX.
[xxiii] All SEM images shown in this chapter were made by XXX.

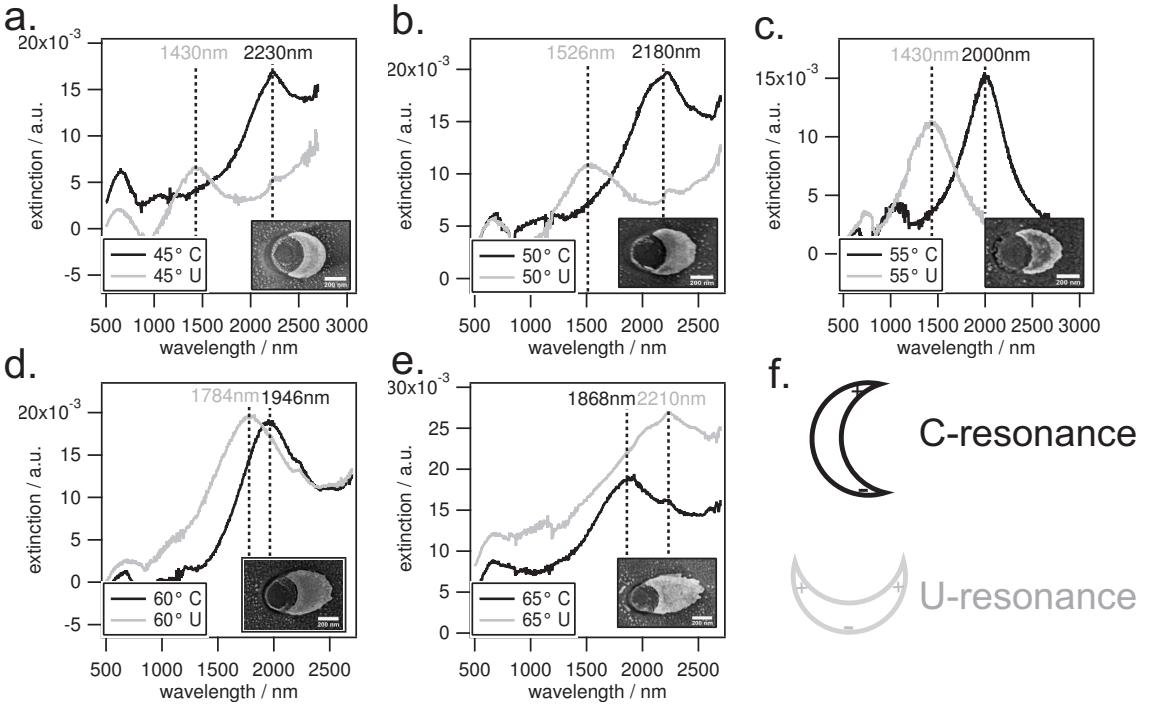

Figure 51: Extinction spectra of single crescents with different geometries. The insets show the scanning electron microscope images.

increasing etching angle and, thus, increasing divergence from the perfect "new moon" crescent shape. In contrast, the C-resonance experiences a blueshift of almost 360 nm. Fig. 52 shows the peak positions for both resonances plotted against the etching angle.

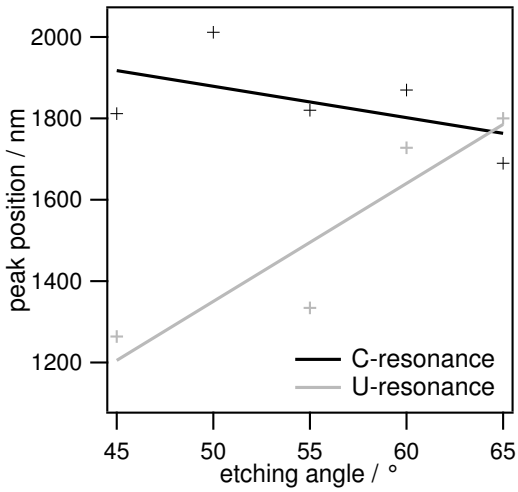

Figure 52: Resonance peak position for the applied etching angles. The black curve represents the C-resonance, the gray curve the U-resonance.

The C-resonance blueshifts linearly with increasing etching angle, whereas the U-resonance shows a redshift. For the latter, however, especially the value for the etching angle of 55° seems to be an outlier and, thus, makes the statistical analysis difficult.

To explain these striking shifts in the optical spectra, correlations between the peak positions and certain geometrical dimensions of the structures were analyzed.
For the U-resonance, a linear dependence of the resonance maximum on the crescent width is found (Fig. 53 a.). With increasing width, the peak shifts to lower energies. This finding can be explained by a simple model. Fig. 53 b. depicts the charges present in the U-resonance. If the width of the crescent increases, the separation of the charges also increases which leads to the decrease in energy. A linear dependence of the peak position on the cresent width is found. The fit function is given in Fig. 53 a.

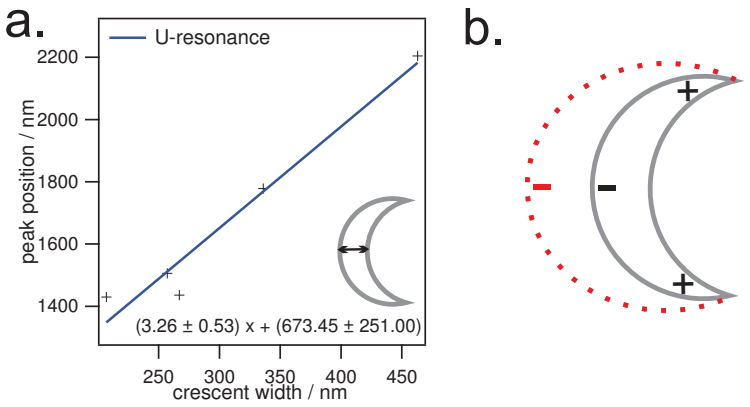

Figure 53: a. Dependence of the U-resonance on the crescents' width, b. charge distribution in the crescent at U-resonance.

In contrast, the maximum of the C-resonance correlates with the contour length of the crescent. Fig. 54 a. shows the plot of the peak position of the C1-resonance versus the contour length. This parameter defines the distance between the two charges (Fig. 54 b.). Upon increasing distance, the peak shifts to lower energies, as it defines the spacing between the charges. A linear dependence of the peak position on the cresent contour length is found. The fit function is given in Fig. 54 a.

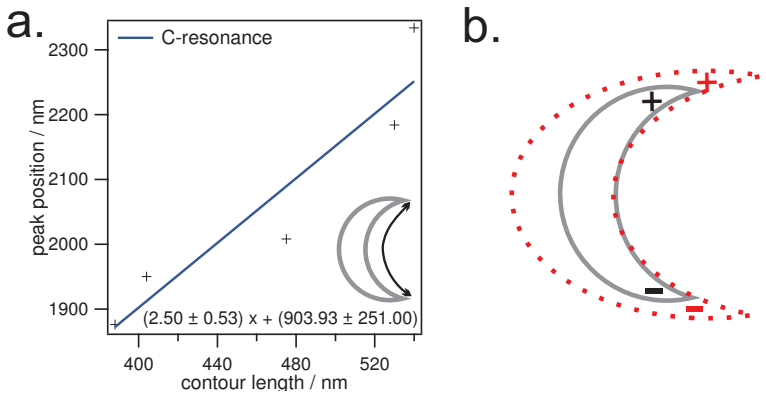

Figure 54: a. Dependence of the C-resonance on the crescents' contour length, b. charge distribution in the crescent at C-resonance.

These simple models for both resonances allow for explaining and predicting the shifts of the plasmon resonance upon minute changes in the shape of the nanostructure. The fit functions can be used to calculate the peak positions for both the C- and the U-resonance of any crescent-shaped nanostructure with known shape by simply replacing the factor x by the width or the contour length, respectively.

The experimental findings were verified with theoretical simulations of the optical properties of identically shaped crescents.[xxiv] Fig. 55 shows the calculated extinction spectra.

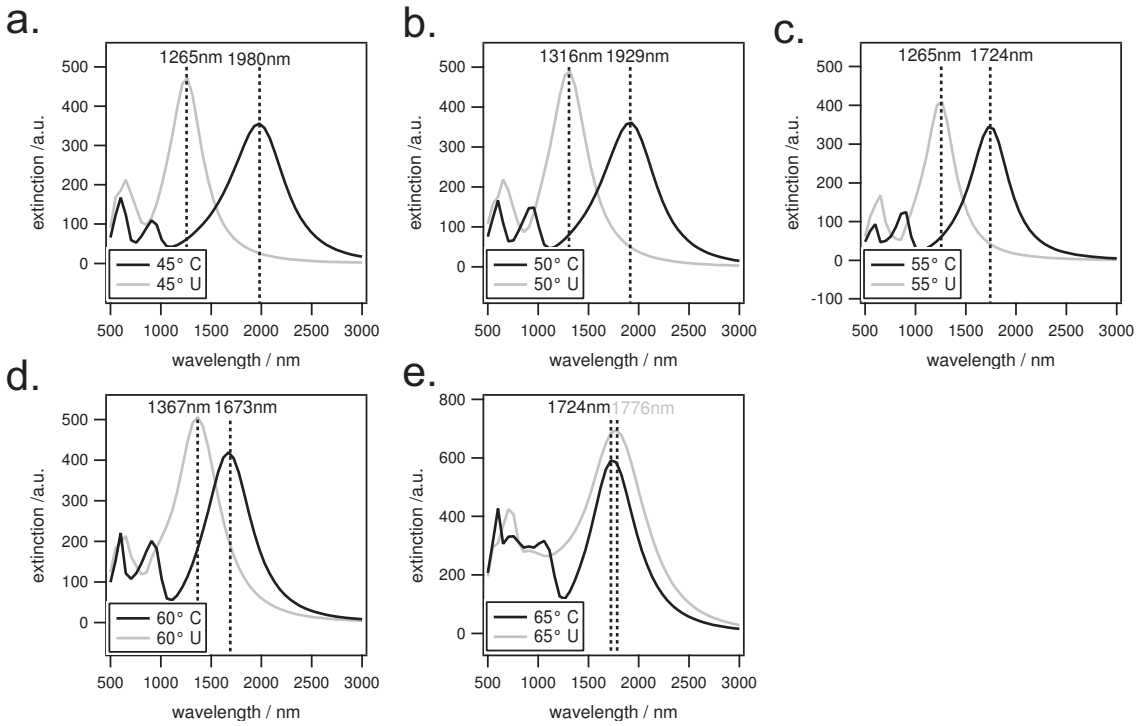

Figure 55: Simulated extinction spectra of the single crescents with different geometries.

The simulated spectra qualitatively resemble the experimentally obtained data. However, all simulations yield smaller wavelengths than the experiment. This effect has also been observed for the simulations of the stacked double crescents in Chapter 7. As explained on p. 76, the differences between simulation and experiment can be ascribed to the roughness of a real sample, and geometry and thickness variations. As before, the simulation parameters, in particular the gold permittivity, have not been refined either, as the simulations reflect all essential features of the experimental data.

The resonance wavelengths obtained from the calculations depend on the etching angle, as seen for the experimentally obtained spectra. In Fig. 56, the simulated and

[xxiv] All theoretical simulations presented in this chapter were performed by XXX.

the experimental curves are juxtaposed. Altogether, the qualitative features of the calculated shifts are in good agreement with the experiment.

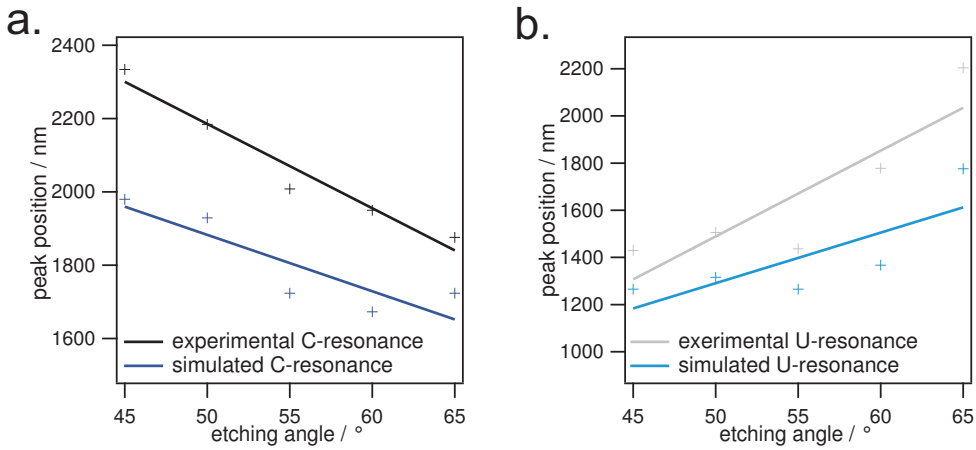

Figure 56: a. Calculated resonance peak position for the applied etching angles. The black curve represents the C-resonance, the gray curve the U-resonance. b. Experimental and calculated resonance maxima.

The shifts in the calculated spectra also correlate with the crescent width in case of the U-resonance, and on the contour length in case of the C-resonance. Fig. 57 shows the corresponding curves for the C- and the U-resonance. For comparison, the experimental data is included in the particular graphs.

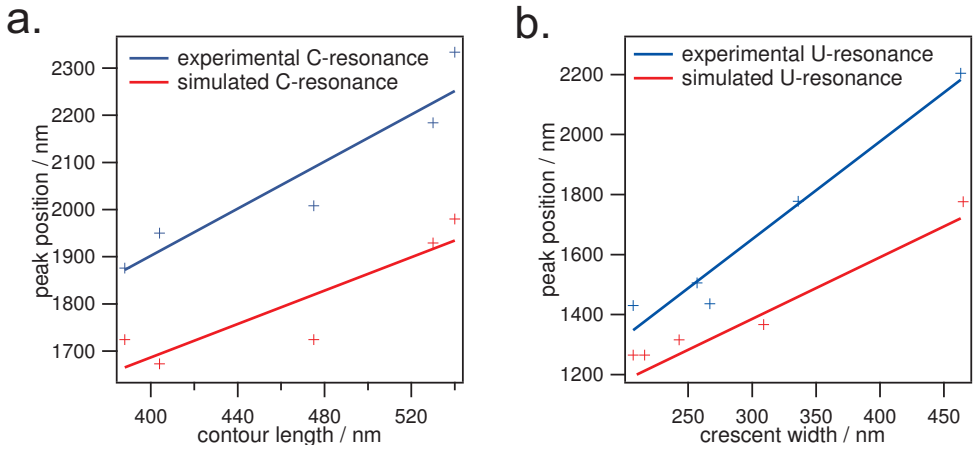

Figure 57: a. Dependence of the simulated and measured U-resonance on the crescents' contour length, b. dependence of the simulated and measured C-resonance on the crescents' width.

8.2.2 Plasmon hybridization in opposing double crescent structures

The stacked double crescents presented in Chapter 7 show a very strong coupling caused by the overlap of the electrical fields of the individual crescents. However, due to the

stacking the resulting structure is not completely symmetric, as one crescent is on top of the other one. A structure with higher symmetry would be valuable to study the dark modes, i.e. resonances without a net dipole.
Hence, the presented single crescents were also prepared as double crescent structures in the same plane with the tips facing each other, giving rise to an additional mirror symmetry axis compared to the stacked double crescents presented in Chapter 7. Fig. 58 illustrates this additional symmetry axis (red).

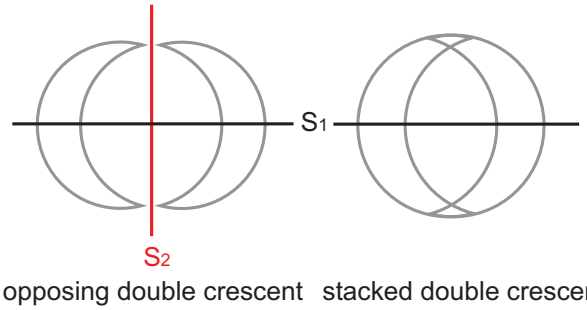

Figure 58: Mirror symmetry axes in the opposing and stacked double crescent structures.

As the tips are in close proximity, the electrical near-fields of the individual crescents should overlap, leading to hybridization of the plasmon resonances. Fig. 59 shows the extinction spectra of the opposing double crescents as measured by UV/vis-NIR spectroscopy.

Both the C-resonance and the U-resonance are blueshifted compared to the single crescent references. The peak positions of the single and the double crescents' resonances are plotted versus the etching angle in Fig. 60. Both curves for the double crescent structures are shifted to lower wavelengths compared to the single structures.

However, due to the fabrication process of the double crescents including the "blind" etching step for the first crescent shown in Fig. 14 (p. 23), differences to the single crescent structures may arise.[xxv] The SEM images reveal that the shapes of the double crescents indeed differ slightly from those of the single crescents (SEM insets in Fig. 51 and Fig. 59).
As established in Chapter 8.2.1, the resonances are very sensitive to minute changes of their shape. Hence, the resonances of the double crescents cannot directly be compared to the single structures, but rather have to be analyzed in terms of their inherent geometric properties first. Only then it is possible to reveal the underlying shifts which are caused by the introduction of a second crescent in close proximity.

[xxv] Amongst others, the metal thickness, the etching time and angle, as well as the rotation between the etching steps can underly certain variations for different samples.

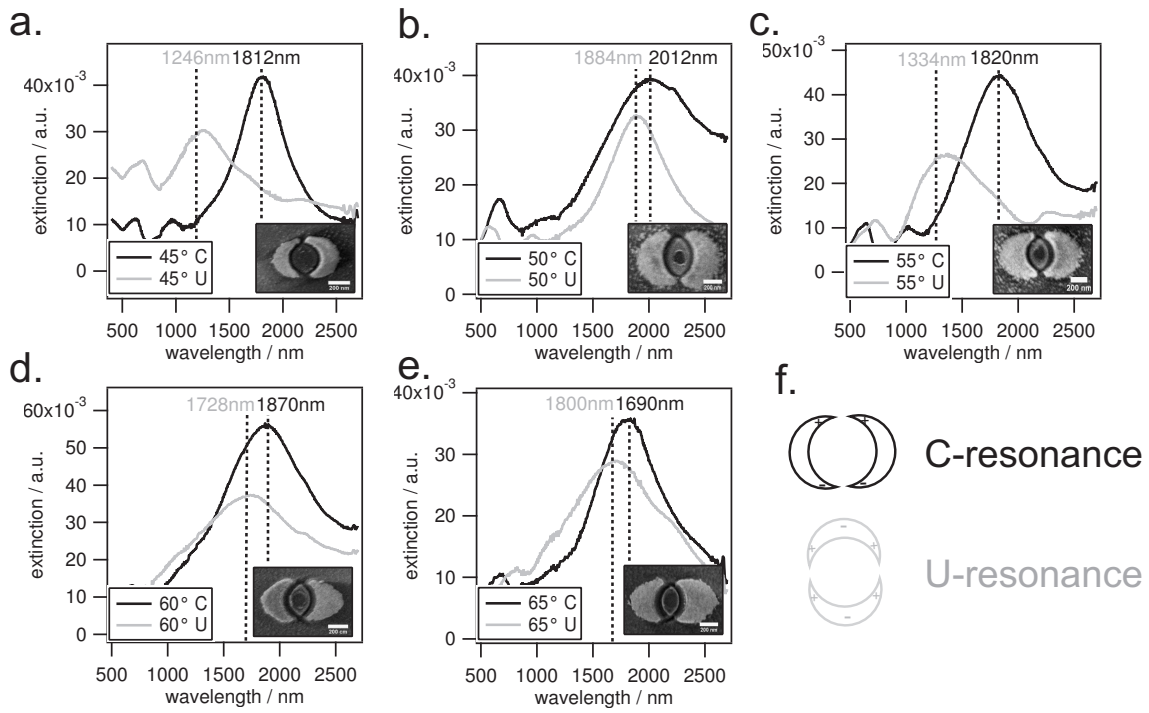

Figure 59: Extinction spectra of opposing double crescents with different geometries. The insets show the scanning electron microscope images.

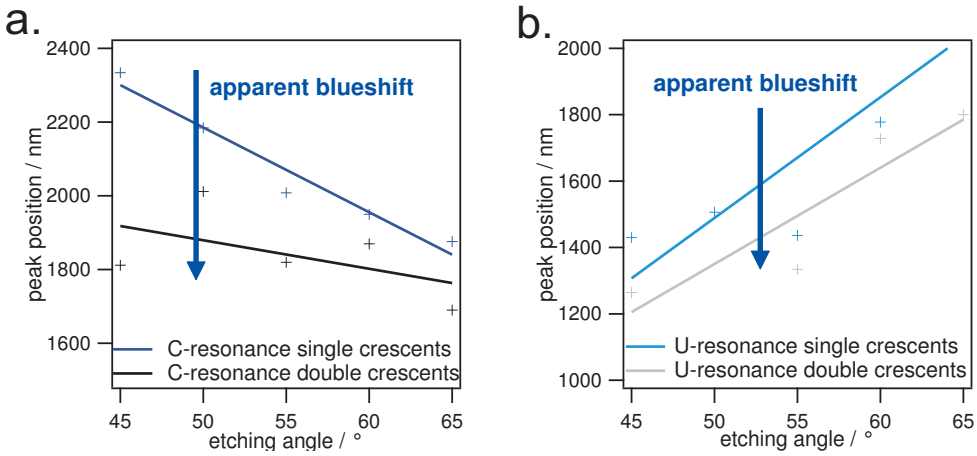

Figure 60: Experimental shifts of the C- and the U-resonance of opposing double crescents.

Therefore, the mean geometric data of the individual crescents are taken and inserted in the fit function obtained from the single crescent references. In detail, the mean crescent width of the double crescents is inserted in the equation for the U-resonance (Fig. 53), namely $3.26\,x + 673.45$, where x is replaced by the particular crescent width. To obtain the C-resonance, the mean contour length is inserted in the fit function of the singles' C-resonance, $2.50\,x + 903.93$ (Fig. 54), where x is replaced by the particular contour length.

This yields the theoretical resonances for single crescents with exactly the geometries

of the fabricated double crescents. It also corresponds to the resonance of the double crescents, if no coupling took place. Hence, in the following it is termed uncoupled resonance.

To obtain the coupling-induced shifts of the double crescents, the experimentally obtained values are compared to the calculated uncoupled values. The results reveal the shifts which arise due to the plasmon coupling. Fig. 61 shows the experimentally obtained resonances, and the shape-corrected values for the C- and the U-resonance.

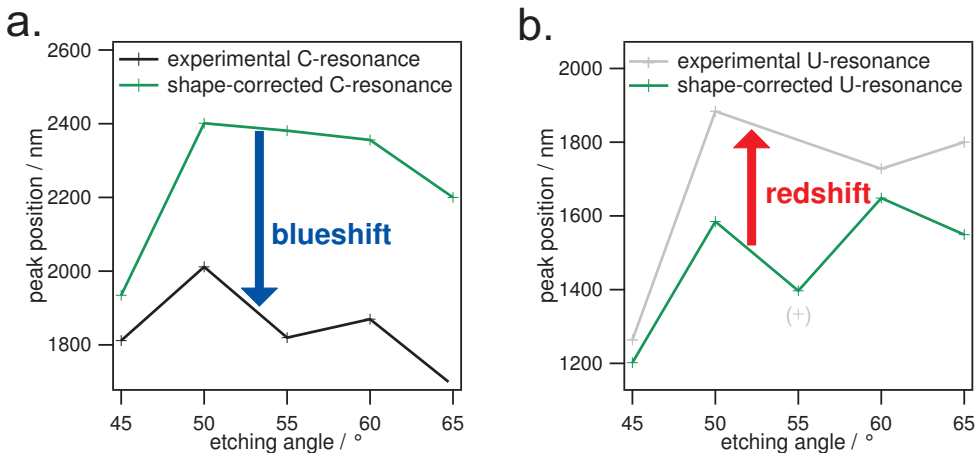

Figure 61: Coupling-induced shifts of the resonances in opposing double crescents. The green curves represent the shape-corrected data, the C-resonance is plotted in black, the U-resonance in gray.

The experimental values of the C-resonance are shifted to lower wavelengths compared to the shape-corrected data. Hence, there is a blueshift which arises upon introduction of a second crescent in close proximity.
In contrast, the U-resonance experiences a redshift, as all measured values are located at higher wavelengths than the shape-corrected ones. Only the datapoint of the 55° sample forms an exception; most probably, this value is an outlier.

These findings are supported by the plasmon hybridization model presented in Chapter 7. This theory is based on the existence of a coupling process between the resonances of the individual nanostructures. Due to the superpositions of the original resonances, new resonances arise. The formation of the hybrid modes due to the coupling process is illustrated in Fig. 62. In both cases, a symmetric and an antisymmetric mode is formed. The symmetric mode is higher in energy compared to the parent resonance, whereas the antisymmetric mode exhibits a lower energy level.

In C-polarization, only the symmetric hybrid mode C+ shows a net dipole, hence, only this mode is visible in optical spectra. Due to the higher energy, the resulting

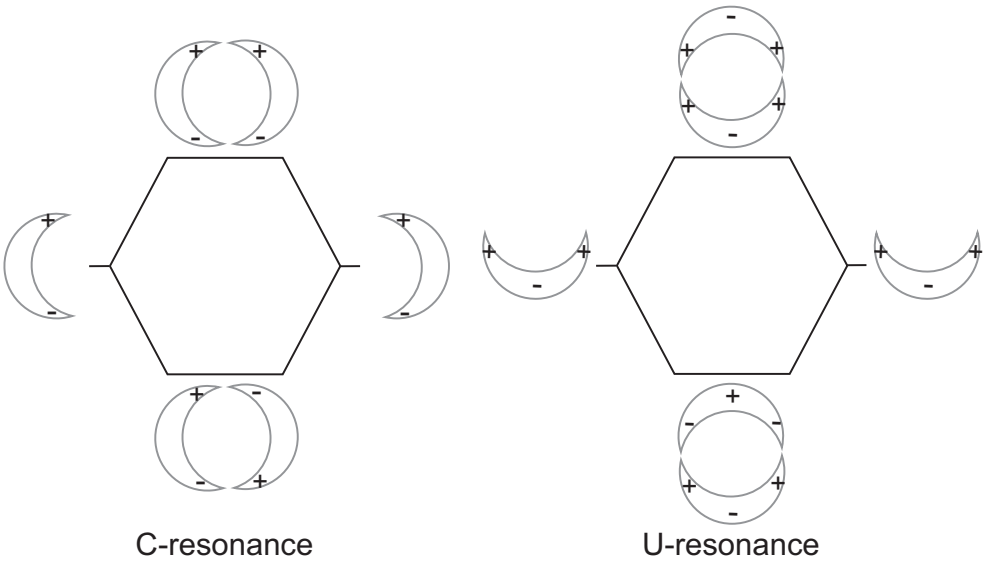

Figure 62: Scheme of the plasmon hybridization model.

resonance appears blueshifted. The antisymmetric mode C- does not feature a net dipole and, thus, is a so-called dark mode.
In U-polarization, the situation is vice versa. Here, only the antisymmetric mode U- exhibits a net dipole and can thus be excited in the optical spectra. The symmetric hybrid U+, however, is a dark mode and does not appear in the spectra. As the energy of the antisymmetric U- hybrid is lower than the energy of the single structure, the resonance appears redshifted compared to the parent resonance of the individual crescents.

Although the shifts between the double crescent spectra and the shape-corrected double crescent spectra possess the same features, i.e. the U-resonance is redshifted, and the C-resonance is blueshifted, the individual values differ quite strongly from each other. This could be due to differences in the separation of the tips of the two crescents. As apparent in the SEM images in Fig. 59, the tip separations vary, and for some samples, the distance is not equal for both sides. If the tips are further apart from each other, the overlap of the electrical fields is diminished. As a result, the coupling is less strong. These variations of the tip separation distances may cause the differences in the shifts for the different samples.

8.3 Conclusions and Outlook

A modified fabrication procedure for crescent-shaped nanoparticles is presented. This method allows for precisely adjusting the shape of the nanostructure. Since the plasmon

resonance is associated to the shape, fine-tuning of the optical properties becomes feasible. Correlations between the geometric parameters and the plasmon resonances have been performed, revealing a strong influence of the crescent width on the U-resonance, and of the inner contour length on the C-resonance, respectively. Theoretical simulations support the experimental findings.

Bringing two individual crescents in close proximity, their electrical near-fields overlap, hence, new resonances arise. However, the resonances of opposing double crescents experience certain shifts as a result of two distinct reasons. First, the individual shape of the structures causes a specific shift. These shape-induced shifts cloak the effects caused by the coupling of the plasmon resonances. By correction of the shape-induced shifts, the shifts evoked by the coupling process can be revealed. These shifts behave as predicted by plasmon hybridization theory.

The established fabrication technique provides the opportunity to use the shape and the coupling efficiency as tuning parameters for precise adjustment of the plasmon resonances. Both the geometry of the structure, and the separation between the crescents are easily accessible. In combination with tuning via dielectric environment and size adjustments, a broad spectral range can be covered.
Due to the high symmetry, these nanostructures hold great potential to be valuable structures for studying the dark modes which arise during the coupling. These modes are not easily addressable. By breaking the symmetry, e.g. by positioning a colloid in one gap between the tips via atomic force microscopy manipulation, these dark modes could be detected.

Appendix

8.4 Achieving defined fluorescence signals

For reasonable investigations of the fluorescence intensity, a uniform distribution of the dye must be assured. Therefore, a drop-coating technique is not suitable as it leads to an uneven dye distribution on the surface (Fig. 63).

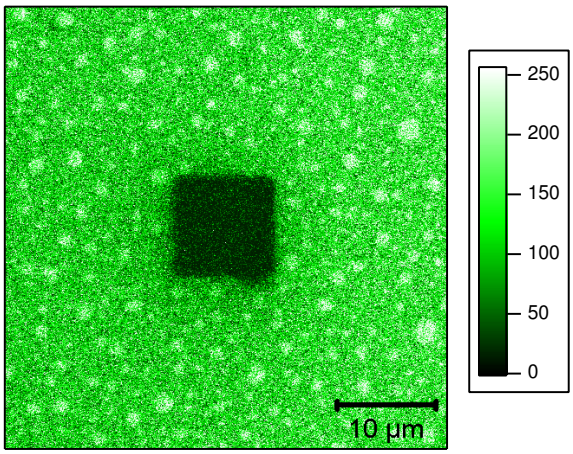

Figure 63: Linear fluorescence at λ_{ex}=488 nm of a sample with the dye Alexa488 prepared with the drop-coating technique. The black square in the center was bleached using a high laser intensity.

The amount of dye molecules on the surface cannot be estimated either. Thus, a more precise coating method was established. Before coating, the dye is covalently bound to the polyelectrolyte PAH by a simple one-step reaction (Fig. 15 on p. 24). The synthesis is based on the reaction of the active succinimidyl ester group of the dye molecule with the free amino group of the polymer. The dye-labeled polymer can then directly be attached to the surface via the polyelectrolyte bilayer formation process described in Chapter 3.2.

Consequently, the dye is evenly distributed on the surface, only located in the defined extension of the top PAH layer. As described in Chapter 3.2, statistically only one of 10,000 amino groups in the polymer is functionalized with the fluorophore, hence, avoiding the formation of aggregates which often leads to shorter fluorescence lifetimes.

Fig. 64 shows a fluorescence microscope image of an analog sample as shown in Fig. 63, however, having attached the dye to the polymer before deposition.

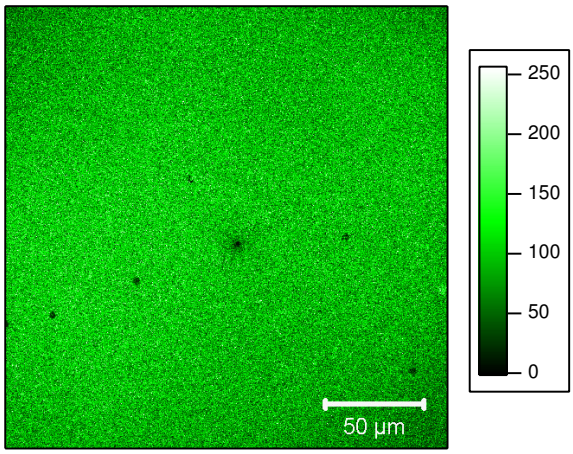

Figure 64: Linear fluorescence at λ_{ex}=488 nm of a sample with the dye Alexa488 prepared with the polymer-functionalization technique.

8.5 Bleaching effects

Fast bleaching of the fluorescence is a big problem when working in close proximity of metal nanoparticles. The electrical near-field is extremely high at sharp tips or edges of a nanostructure; this energy confinement can easily lead to irreversible damage of the fluorescent molecules. Especially when working with thin layers of low dye concentration, this effect has to be overcome. Therefore, investigations on bleaching stability in different surrounding media were performed.

The dye-covered substrates were irradiated with laser light of the appropriate wavelength. Several squared areas of 10 µm^2 were written by raster scanning. Both intensity (from 1 µW to 45 µW) and scan speed (from 1 ms to 8 ms) were varied.

Fig. 65 shows the fluorescence microscope image of the sample with the dye Atto425 after the square bleaching. The highest emission intensities are obtained in air and nitrogen atmosphere.

Fig. 66 shows the fluorescence microscope image of the dye Atto 390 after the square bleaching. This dye shows the highest intensity in an air atmosphere.

The fluorescence intensities were extracted, and a power dose was calculated ac-

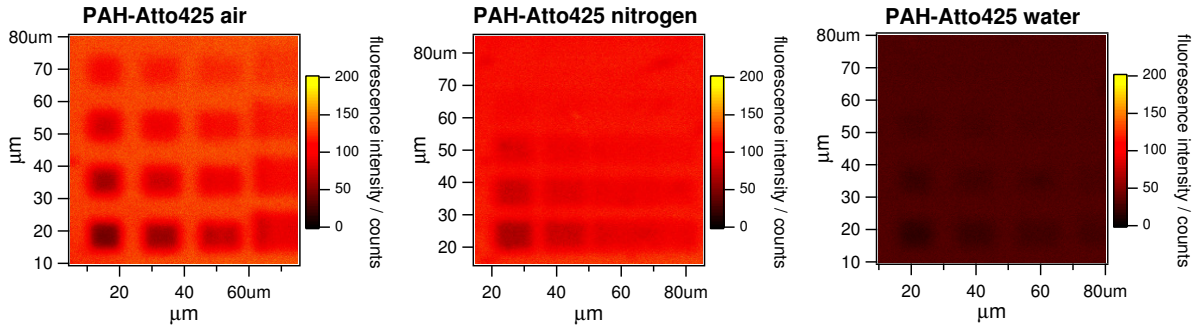

Figure 65: Fluorescence bleaching study of the dye Atto425.

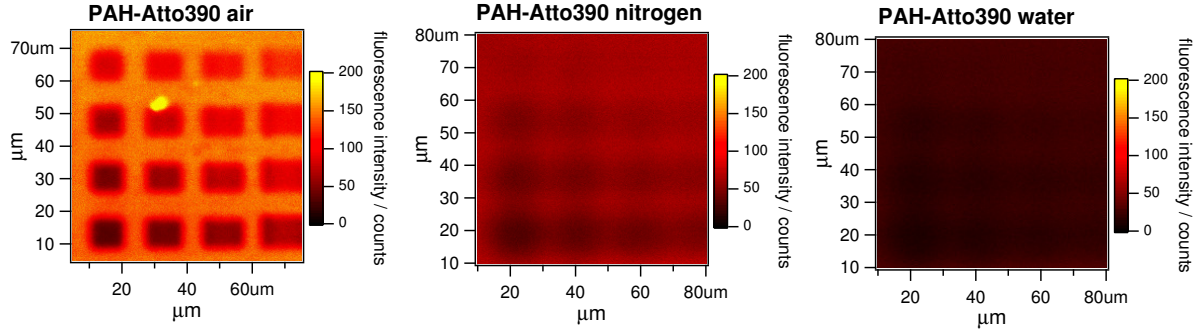

Figure 66: Fluorescence bleaching study of the dye Atto390.

cording to Equation (27).

$$D = I_{bleach} \cdot v_{scan} \,/\, A \tag{27}$$

D: power dose I_{bleach}: bleaching intensity
v_{scan}: scan speed A: pixel area

Fig. 67 shows the bleaching curves for the dyes in the different surrounding media. Obviously, the use of a liquid medium leads to a significant loss in emission intensity. The exposure to an air or nitrogen atmosphere, however, yields comparable intensities at least four times higher than for an aqueous surrounding. Therefore, air was selected as medium instead of nitrogen due to simplicity in the setup and yet high emission intensity.

Possibly, the fluorescence is quenched by radiationless transitions of the excited molecules in the ground state by emitting energy via collisions with the solvent molecules as explained in Chapter 2.1.1.

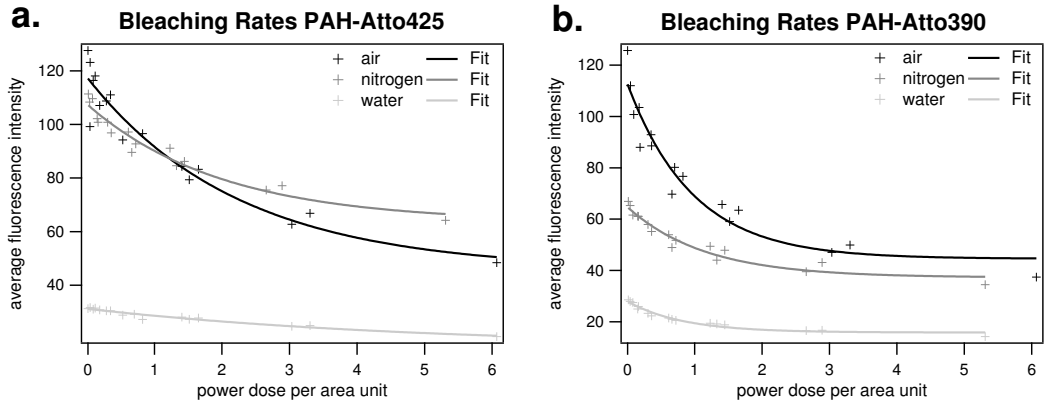

Figure 67: Bleaching curves of the dyes Atto425 (a.) and Atto390 (b.).

8.6 Two-photon excitation of Atto425

For the ongoing study, the dye Atto425 was chosen, as it shows high intensity and a good stability upon laser treatment. The one-photon absorption maximum is at 436 nm. A two-photon excited fluorescence intensity study was performed to obtain the maximum intensity for two-photon excitation. Therefore, several equally sized squares of the sample were scanned with different excitation wavelengths, from 780 nm to 820 nm. Each square was only scanned once to avoid bleaching. The fluorescence intensities of these areas was analyzed and compared. As with increasing wavelength the power of the laser beam decreases, the obtained fluorescence intensities were normalized with respect to the excitation power. Fig. 68 shows the two-photon absorption spectrum of the dye Atto425. The maximum is obtained around 790 nm, thus, this wavelength was used for two-photon induced fluorescence excitation.

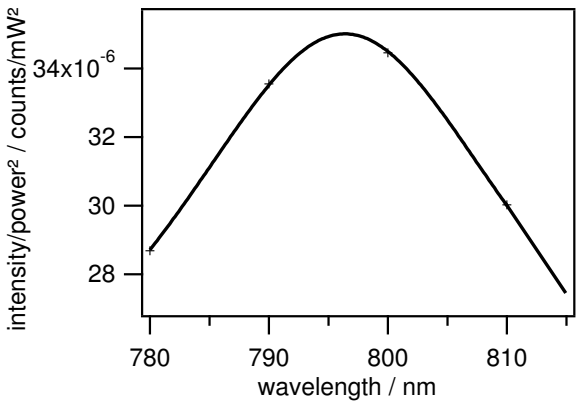

Figure 68: Two-photon absorption spectrum of the dye Atto425.

Usually, two-photon absorption spectra are performed with more precise methods. However, this approach offers an insight into the two-photon excitation process. To

estimate the optimum wavelength for excitation, it is suitable and readily available at every confocal setup with a two-photon excitation facility.

Bibliography

[1] M. Faraday. The Bakerian lecture - On the experimental relations of gold (and other metals) to light. *Philosophical Transactions of the Royal Society of London*, 147:145, 1857.

[2] G. Mie. Beiträge zur Optik trüber Medien, speziell kolloidaler Metallösungen. *Annalen der Physik*, 25(3):377, 1908.

[3] R. Gans. Über die Form ultramikroskopischer Goldteilchen. *Annalen der Physik*, 342(5):881, 1912.

[4] W. A. Murray and W. L. Barnes. Plasmonic materials. *Advanced Materials*, 19(22):3771, 2007.

[5] W. Demtröder. *Molecular Physics*. Wiley-VCH, Weinheim, 2005.

[6] F. Petzke. Optische Molekülspektroskopie, 2004.

[7] D. Wöhrle, M. W. Tausch, and W.-D. Stohrer. *Photochemie*. Wiley-VCH, Weinheim, 2005.

[8] M. Göppert-Mayer. *Über Elementarakte mit zwei Quantensprüngen*. PhD thesis, Universität Göttingen, 1931.

[9] M. Göppert-Mayer. Über Elementarakte mit zwei Quantensprüngen. *Annalen der Physik*, 401:273, 1931.

[10] W. Kaiser and C. G. B. Garrett. Two-photon excitation in CaF_2:Eu^{2+}. *Physical Review Letters*, 7:229, 1961.

[11] W. Denk, J. H. Strickler, and W. W. Webb. Two-photon laser scanning fluorescence microscopy. *Science*, 248:73, 1990.

[12] J. R. Lakowicz. *Topics in fluorescence spectroscopy vol. 5: Nonlinear and two-photon-indued fluorescence*. Springer, 1997.

[13] A. Diaspro. *Confocal and two-photon microscopy: foundations, applications, and advances*. Wiley, Liss, 2002.

[14] A. Diaspro. Introduction to two-photon microscopy. *Microscopy Research and Technique*, 47:163, 1999.

[15] P. R. Callis. Two-photon-induced fluorescence. *Annual Review of Physical Chemistry*, 48:271, 1997.

[16] J. R. Lakowicz. *Principles of Fluorescence Spectroscopy*. Springer Science+Business Media, LLC, 2006.

[17] N. W. Ashcroft and N. D. Mermin. *Solid State Physics*. Harcourt College Publishing, Saunders College, Philadelphia, 1976.

[18] C. Kittel. *Introduction to Solid State Physics*. John Wiley & Sons, New York, 1996.

[19] U. Kreibig and M. Vollmer. *Optical Properties of Metal Clusters*. Springer-Verlag, Berlin, 1995.

[20] L. Novotny and B. Hecht. *Principles of Nano-Optics*. Cambridge University Press, 2006.

[21] C. Sönnichsen. *Plasmons in metal nanostructures*. PhD thesis, Ludwig-Maximilians-Universität München, 2001.

[22] C. Sönnichsen. *Plasmons in metal nanostructures*. Cuviller Verlag, Göttingen, 2001.

[23] C. F. Bohren and D. R. Huffmann. *Absorption and Scattering of Light by Small Particles*. Wiley-VCH, Berlin, 1998.

[24] W. Nolting. *Grundkurs Theoretische Physik, Band 3: Elektrodynamik*. Friedrich Vieweg und Sohn Verlagsgesellschaft, Braunschweig, 1997.

[25] W. Greiner. *Theoretische Physik, Band 3: Klassische Elektrodynamik*. Verlag Harri Deutsch, Fulda, 1991.

[26] P. Debye. Der Lichtdruck auf Kugeln von beliebigem Material. *Annalen der Physik*, 335(11):57, 1909.

[27] J. C. Maxwell. A dynamical theory of the electromagnetic field. *Philosophical Transactions of the Royal Society of London*, 155:459, 1865.

[28] W. L. Barnes. Fluorescence near interfaces: the role of photonic mode density. *Journal of Modern Optics*, 45:661, 1998.

[29] C. Girard, O. J. F. Martin, and A. Dereux. Molecular lifetime changes induced by nanometer-scale optical-fields. *Physical Review Letters*, 75:3098, 1995.

[30] M. Fleischmann, P. J. Hendra, and A. J. McQuilla. Raman spectra of pyridine adsorbed at a silver electrode. *Chemical Physics Letters*, 26:1638, 1974.

[31] D. L. Jeanmaire and R. P. vanDuyne. Surface Raman spectroelectrochemistry Part 1. Heterocyclic, aromatic, and aliphatic amines adsorbed on the anodized silver electrode. *Journal Of Electroanalytical Chemistry*, 84:1, 1977.

[32] K. Kneipp, Y. Wang, H. Kneipp, L. T. Perelman, I. Itzkan, R. Dasari, and M. S. Feld. Single molecule detection using surface-enhanced Raman scattering. *Physical Review Letters*, 78:1667, 1997.

[33] A. M. Nie and S. R. Emery. Probing single molecules and single nanoparticles by surface-enhanced Raman scattering. *Science*, 275:1102, 1997.

[34] A. M. Glass, P. F. Liao, J. G. Bergmann, and D. H. Olson. Interaction of metal particles with absorbed dye molecules - absorption and luminescence. *Optics Letters*, 5(9):368, 1980.

[35] D. A. Weitz, S. Garoff, J. I. Gersten, and A. Nitzan. The enhancement of Raman-scattering, resonance Raman-scattering, and fluorescence from molecules adsorbed on a rough silver surface. *Journal of Chemical Physics*, 78(9):5324, 1983.

[36] A. Wokaun, H. P. Lutz, A. P. King, U. P. Wild, and R. R. Ernst. Energy-transfer in surface enhanced luminescence. *Journal of Chemical Physics*, 78(1):5324, 1983.

[37] K. H. Drexhage. Influence of a dielectric interface on fluorescence decay time. *Bulletin of the American Physical Society*, 14:873, 1969.

[38] K. H. Drexhage. Influence of a dielectric interface on fluorescence decay time. *Journal of Luminescence*, 1-2:693, 1970.

[39] D. Madge, E. Elson, and W. W. Webb. Thermodynamic fluctuations in a reacting system – measurement by fluorescence correlation spectroscopy. *Physical Review Letters*, 29(11):705, 1972.

[40] E. Elson and D. Madge. Fluorescence correlation spectroscopy. I. Conceptual basis and theory. *Biopolymers*, 13:1, 1974.

[41] D. Madge, E. Elson, and W. W. Webb. Fluorescence correlation spectroscopy. II. An experimental realization. *Biopolymers*, 13:29, 1974.

[42] P. Hanarp, M. Kåll, and D. S. Sutherland. Optical properties of short range ordered arrays of nanometer gold disks prepared by colloidal lithography. *Journal of Physical Chemistry B*, 107(24):5768, 2003.

[43] J. S. Shumaker-Parry, H. Rochholz, and M. Kreiter. Fabrication of crescent-shaped optical antennas. *Advanced Materials*, 17(17):2131, 2005.

[44] M. Retsch, Z. C. Zhou, S. Rivera, M. Kappl, X. S. Zhao, U. Jonas, and Q. Li. Fabrication of large-area, transferable colloidal monolayers utilizing self-assembly at the air/water interface. *Macromolecular Chemistry and Physics*, 210(3-4):230, 2009.

[45] G. Decher, J. D. Hong, and J. Schmitt. Buildup of ultrathin multilayer films by a self-assembly process: Iii. consecutively alternating adsorption of anionic and cationic polyelectrolytes on charged surfaces. *Thin Solid Films*, 210:831, 1992.

[46] N. Horn and M. Kreiter. Plasmon spectroscopy: Methods, pitfalls, and how to avoid them. *Plasmonics*, 2010. DOI:10.1007/s11468-010-9148-5.

[47] J. Pomplun, S. Burger, L. Zschiedrich, and F. Schmidt. Adaptive finite element method for simulation of optical nano structures. *Phys. Status Solidi B*, 224(10):3419, 2007.

[48] P. B. Johnson and R. W. Christy. Optical constants of the noble metals. *Physical Review B*, 6(12):4370, 1972.

[49] K. Weisshart, V. Juengel, and S. J. Briddon. The lsm 510 meta confocor 2 system: An integrated imaging and spectroscopic platform for single-molecule detection. *Current Pharmaceutical Biotechnology*, 5(2):135, 2004.

[50] M. Álvarez, A. Best, S. Pradhan-Kadam, K. Koynov, U. Jonas, and M. Kreiter. Single-photon and two-photon induced photocleavage for monolayers of an alkyltriethoxysilane with a photoprotected carboxylic ester. *Advanced Materials*, 20:4563, 2008.

[51] W. Denk, J. P. Strickler, and W. W. Webb. Patent no. us5034613 (a): Two-photon laser microscopy, 1991.

[52] A. Kramer, W. Trabesinger, B. Hecht, and U. P. Wild. Optical near-field enhancement at a metal tip probed by a single fluorophore. *Applied Physics Letters*, 80(9):1652, 2002.

[53] T. Nakamura and S. Hayashi. Enhancement of dye fluorescence by gold nanoparticles: Analysis of particle size dependence. *Japanese Journal of Applied Physics Part 1-Regular Papers Brief Communications & Review Papers*, 44(9A):6833, 2005.

[54] J. Zhu, K. Zhu, and L. Huang. Using gold colloid nanoparticles to modulate the surface enhanced fluorescence of Rhodamine B. *Physics Letters A*, 372(18):3283, 2008.

[55] G. Schneider, G. Decher, N. Nerambourg, R. Praho, M. H. V. Werts, and M. Blanchard-Desce. Distance-dependent fluorescence quenching on gold nanoparticles ensheathed with layer-by-layer assembled polyelectrolytes. *Nano Letters*, 6(3):530, 2006.

[56] P. Anger, P. Bharadwaj, and L. Novotny. Enhancement and quenching of single-molecule fluorescence. *Physical Review Letters*, 96(11):113002, 2006.

[57] A. M. Glass, A. Wokaun, J. P. Heritage, J. G. Bergman, P. F. Liao, and D. H. Olson. Enhanced 2-photon fluorescence of molecules adsorbed on silver particle films. *Physical Review B*, 24(8):4906, 1981.

[58] I. Cohanoschi and F. E. Hernández. Surface plasmon enhancement of two- and three-photon absorption of hoechst 33 258 dye in activated gold colloid solution. *Journal of Physical Chemistry B*, 109(30):14506, 2005.

[59] O. G. Tovmachenko, C. Graf, D. J. van den Heuvel, A. van Blaaderen, and H. C. Gerritsen. Fluorescence enhancement by metal-core/silica-shell nanoparticles. *Advanced Materials*, 18(1):91, 2006.

[60] B. Valeur. *Molecular Fluorescence: Principles and Applications*. Wiley-VCH, Berlin, 2001.

[61] A. Pomozzi. *Fluorescence close to Dielectric Interfaces*. PhD thesis, Johannes Gutenberg Universität Mainz, 2008.

[62] M. Lindrum, A. Glismann, J. Moll, and S. Daehne. Energy migration phenomena in j-aggregates: 1. fluorescence lifetime measurements and hole burning experiments on j-aggregates of a benzimidocarbocyanine dye. *Chemical Physics*, 178:423, 1993.

[63] V. Ghukasyan, C. Hsu, C. Liu, F. Kao, and T. Cheng. Fluorescence lifetime dynamics of enhanced green fluorescent protein in protein aggregates with expanded polyglutamine. *Journal of Biomedical Optics*, 15:016008, 2010.

[64] A. Mooradian. Photoluminescence of metals. *Physical Review Letters*, 22(5):185, 1969.

[65] G. T. Boyd, Z. H. Yu, and Y. R. Shen. Photoinduced luminescence from the noble-metals and its enhancement on roughened surfaces. *Physical Review B*, 33(12):7923, 1986.

[66] P. J. Schuck, D. P. Fromm, A. Sundaramurthy, G. S. Kino, and W. E. Mörner. Improving the mismatch between light and nanoscale objects with gold bowtie nanoantennas. *Physical Review Letters*, 94(1):017402, 2005.

[67] M. R. Beversluis, A. Bouhelier, and L. Novotny. Continuum generation from single gold nanostructures through near-field mediated intraband transitions. *Physical Review B*, 68(11):115433, 2003.

[68] A. Bouhelier, R. Bachelot, G. Lerondel, S. Kostcheev, P. Royer, and G. P. Wiederecht. Surface plasmon characteristics of tunable photoluminescence in single gold nanorods. *Physical Review Letters*, 95:267405, 2005.

[69] M. Kreiter, S. Mittler, W. Knoll, and J. R. Sambles. Surface plasmon-related resonances on deep and asymmetric gold gratings. *Physical Review B*, 65:125415, 2002.

[70] I. Gryczynski, J. Malicka, Y. B. Shen, Z. Gryczynski, and J. R. Lakowicz. Multiphoton excitation of fluorescence near metallic particles: Enhanced and localized excitation. *Advanced Materials*, 22(23):2542, 2002.

[71] I. Cohanoschi, Y. Sheng, K. D. Belfield, and F. E. Hernández. Effect of the concentration of organic dyes on their surface plasmon enhanced two-photon absorption cross section using activated au nanoparticles. *Journal of Applied Physics*, 101:086112, 2007.

[72] J. M. Jung, H. W. Yoo, F. Stellacci, and H. T. Jung. Two-photon excited fluorescence enhancement for ultrasensitive dna detection on large-area gold nanopatterns. *Advanced Materials*, 22(23):2542, 2010.

[73] U. Kreibig and L. Genzel. Optical absorption of small metallic particles. *Surface Science*, 156:678, 1985.

[74] J. J. Mock, Barbic M., D. R. Smith, D. A. Schultz, and S. Schultz. Shape effects in plasmon resonance of individual colloidal silver nanoparticles. *Journal of Chemical Physics*, 116(15):6755, 2002.

[75] F. Wang and Y. R. Shen. General properties of local plasmons in metal nanostructures. *Physical Review Letters*, 97:206806, 2006.

[76] A. Unger. *Refractive index sensing with localized plasmonic resonances - theoretical description and experimental verification.* PhD thesis, Universität Mannheim, 2010.

[77] B. Nikoobakht and M. El-Sayed. Preparation and growth mechanism of gold nanorods (nrs) using seed-mediated growth method. *Chemistry of Materials*, 15:1957, 2003.

[78] Y. Sun and Y. Xia. Triangular nanoplates of silver: Synthesis, characterization, and use as sacrificial templates for generating triangular nanorings of gold. *Advanced Materials*, 15(9):695, 2004.

[79] D. P. Fromm, A. Sundaramurthy, P. J. Schuck, G. Kino, and W. E. Mörner. Gap-dependent optical coupling of single bowtie" nanoantennas resonant in the visible. *Nano Letters*, 4(5):957, 2004.

[80] A. R. Siekkinen, J. M. McLellan, J. Chen, and Y. Xia. Rapid synthesis of small silver nanocubes by mediating polyol reduction with a trace amount of sodium sulfide or sodium hydrosulfide. *Chemical Physics Letters*, 432:491, 2006.

[81] L. Y. Wu, B. M. Ross, and L. P. Lee. Optical properties of the crescent-shaped nanohole antenna. *Nano Letters*, 9(5):1956, 2009.

[82] R. Jin, Y. W. Cao, C. A. Mirkin, K. L. Kelly, G. C. Schatz, and J. G. Zheng. Photoinduced conversion of silver nanospheres to nanoprisms. *Science*, 294:1901, 2001.

[83] M. Liu and P. Guyot-Sionnest. Synthesis and optical characterization of Au/Ag core/shell nanorods. *Journal of Physical Chemistry B*, 108:5882, 2004.

[84] K. Vasilev, W. Knoll, and M. Kreiter. Fluorescence intensities of chromophores in front of a thin metal film. *Journal of Chemical Physics*, 120:3439, 2004.

[85] N. L. Bocchio. *Noble-metal nanoparticles produced with colloidal lithography: fabrication, optical properties and applications.* PhD thesis, Johannes Gutenberg Universität Mainz, 2008.

[86] H. Rochholz, N. Bocchio, and M. Kreiter. Tuning resonances on crescent-shaped noble-metal nanoparticles. *New Journal of Physics*, 9(53), 2007.

[87] R. Rigler and E. S. Elson. *Fluorescence Correlation Spectroscopy. Theory and Applications.* Springer-Verlag, Berlin, 2001.

[88] R. Rigler, Ü. Mets, J. Widengren, and P. Kask. Fluorescence correlation spectroscopy with high count rate and low background – analysis of translational diffusion. *European Biophysics Journal*, 22:169, 1993.

[89] Y. Takahashi, N. Bark, M. Kinjo, and R. Rigler. Fluorescence correlation spectroscopy (fcs) analysis of human red blood cell system. *Optical Review*, 10:596, 2003.

[90] P. Schwille, J. Korlach, and W. W. Webb. Fluorescence correlation spectroscopy with single-molecule sensitivity on cell and model membranes. *Cytometry*, 36:176, 1999.

[91] T. Ohrt, J. Muetze, W. Staroske, L. Weinmann, J. Hoeck, K. Crell, G. Meister, and P. Schwille. Fluorescence correlation spectroscopy with single-molecule sensitivity on cell and model membranes. *Nucleic Acids Research*, 36:6439, 2008.

[92] Z. F. Wang, O. Marcu, M. W. Berns, and J. L. Marsh. In vivo fcs measurements of ligand diffusion in intact tissues. In *Multiphoton Microscopy in the Biomedical Sciences IV*, volume 5323 of *Proceedings of the Society of Photo-Optical Instrumentation Engineers (SPIE)*, page 177, 2004.

[93] B. S. Kim, O. V. Lebedeva, K. Koynov, H. F. Gong, G. Glasser, I. Lieberwirth, and O. I. Viogradova. Effect of organic solvent on the permeability and stiffness of polyelectrolyte multilayer microcapsules. *Macromolecules*, 38:5214, 2005.

[94] K. Koynov, G. Mihov, M. Mondeshki, C. Moon, H. W. Spiess, K. Müllen, H. J. Butt, and G. Floudas. Diffusion and conformation of peptide-functionalized polyphenylene dendrimers studied by fluorescence correlation and c-13 nmr spectroscopy. *Biomacromolecules*, 8:1745, 2007.

[95] T. Cherdhirankorn, V. Harmandaris, A. Juhari, P. Voudouris, G. Fytas, K. Kremer, and K. Koynov. Fluorescence correlation spectroscopy study of molecular probe diffusion in polymer melts. *Macromolecules*, 42:4858, 2009.

[96] A. Michelman-Ribeiro, H. Boukari, R. Nossal, and F. Horkay. Structural changes in polymer gels probed by fluorescence correlation spectroscopy. *Macromolecules*, 37:10212, 2004.

[97] M. Gianneli, P. W. Beines, R. F. Roskamp, K. Koynov, G. Fytas, and W. Knoll. Local and global dynamics of transient polymer networks and swollen gels anchored on solid surfaces. *Journal of Physical Chemistry C*, 111:13205, 2007.

[98] G. Modesti, B. Zimmermann, M. Borsch, A. Herrmann, and K. Saalwächter. Diffusion in model networks as studied by NMR and fluorescence correlation spectroscopy. *Macromolecules*, 42:4681, 2009.

[99] R. Zhang, T. Cherdhirankorn, K. Graf, K. Koynov, and R. Berger. Swelling of cross-linked polystyrene beads in toluene. *Microelectronic Engineering*, 85:1261, 2008.

[100] L. C. Estrada, P. F. Aramendia, and O. E. Martinez. 10000 times volume reduction for fluorescence correlation spectroscopy using nano-antennas. *Optics Express*, 16:20597, 2008.

[101] J. Aizpurua, P. Hanarp, D. S. Sutherland, M. Käll, G. W. Bryant, and F. J. G. García de Abajo. Optical properties of gold nanorings. *Physical Review Letters*, 90(5):057401, 2003.

[102] B. Lamprecht, G. Schider, R. T. Lechner, H. Ditlbacher, J. R. Krenn, A. Leitner, and F. R. Aussenegg. Metal nanoparticle gratings: Influence of dipolar particle interaction on the plasmon resonance. *Physical Review Letters*, 84:4721, 2000.

[103] A. Wei, B. Kim, B. Sadtler, and S. L. Tripp. Tunable surface-enhanced Raman scattering from large gold nanoparticle arrays. *European Journal of Chemical Physics and Physical Chemistry*, 2:743, 2000.

[104] P. L. Stiles, J. A. Dieringer, N. C. Shah, N. C. Shah, and R. P. van Duyne. Surface-enhanced Raman spectroscopy. *Annual Review of Analytical Chemistry*, 1:601, 2008.

[105] R. A. Shelby, D. R. Smith, and S. Schultz. Experimental verification of a negative index of refraction. *Science*, 292 (5514):77, 2001.

[106] D. R. Smith, J. B. Pendry, and M. C. K. Wiltshire. Metamaterials and negative refractive index. *Science*, 305 (5685):788, 2004.

[107] J. B. Pendry, A. J. Holden, D. J. Robbins, and W. J. Stewart. Magnetism from conductors and enhanced nonlinear phenomena. *IEEE Transactions on Microwave Theory and Techniques*, 47(11):2075, 1999.

[108] D. R. Smith, W. J. Padilla, D. C. Vier, S. C. Nemat-Nasser, and S. Schultz. Composite medium with simultaneously negative permeability and permittivity. *Physical Review Letters*, 84(18):4184, 2000.

[109] J. B. Pendry. Negative refraction. *Contemporary Physics*, 45(3):191, 2004.

[110] V. M. Shalaev, W. S. Cai, U. K. Chettiar, H. K. Yuan, A. K. Sarychev, V. P. Drachev, and A. V. Kildishev. Negative index of refraction in optical metamaterials. *Optics Letters*, 30(24):3356, 2005.

[111] V. M. Shalaev. Optical negative-index metamaterials. *Nature Photonics*, 1(1):41, 2007.

[112] C. M. Soukoulis and M. Linden, S.; Wegener. Negative refractive index at optical wavelengths. *Science*, 315(5808):47, 2007.

[113] U. C. Fischer and H. P. Zingsheim. Sub-microscopic pattern replication with visible-light. *Journal of Vacuum Science & Technology*, 19(4):881, 1981.

[114] J. C. Hulteen and R. P. Van Duyne. Nanosphere lithography - a materials general fabrication process for periodic particle array surfaces. *Journal of Vacuum Science & Technology A*, 13(3):1553, 1995.

[115] C. L. Haynes and R. P. Van Duyne. Nanosphere lithography: A versatile nanofabrication tool for studies of size-dependent nanoparticle optics. *Journal of Physical Chemistry B*, 105(24):5599, 2001.

[116] M. C. Gwinner, E. Koroknay, L. W. Fu, P. Patoka, W. Kandulski, M. Giersig, and H. Giessen. Periodic large-area metallic split-ring resonator metamaterial fabrication based on shadow nanosphere lithography. *Small*, 5(3):400, 2009.

[117] M. Retsch, M.; Tamm, N. Bocchio, N. Horn, R. Forch, U. Jonas, and M. Kreiter. Parallel preparation of densely packed arrays of 150 nm gold-nanocrescent resonators in three dimensions. *Small*, 5(18):2105, 2009.

[118] A. Hoffmann, Z. Lenkefi, and Z. Szentirmay. Effect of roughness on surface plasmon scattering in gold films. *Journal of Physics - Condensed Matter*, 10:5503, 1998.

[119] K. M. Byun, S. J. Yoon, and D. Kim. Effect of surface roughness on the extinction-based localized surface plasmon resonance biosensors. *Applied Optics*, 47:5886, 2008.

[120] S. E. Skrabalak, L. Au, X. D. Li, and Y. Xia. dfFacile synthesis of Ag nanocubes and Au nanocages. *Nature Protocols*, 2:2182, 2007.

[121] C. L. Nehl, H. W. Liao, and J.H. Hafner. Optical properties of star-shaped gold nanoparticles. *Nano Letters*, 6:683, 2006.

[122] P. S. Kumar, I. Pastoriza-Santos, B. Rodriguez-Gonzalez, F. J. Garcia de Abajo, and L. M. Liz-Marzan. High-yield synthesis and optical response of gold nanostars. *Nanotechnology*, 19:015606, 2008.

[123] N. G. Khlebtsov. Optics and biophotonics of nanoparticles with a plasmon resonance. *Quantum Electronics*, 38:504, 2008.

[124] K. A. Willets and R. P. Van Duyne. Localized surface plasmon resonance spectroscopy and sensing. *Annular Review of Physical Chemistry*, 58:267, 2007.

[125] T. R. Jensen, M. L. Duval, K. L. Kelly, A. A. Lazarides, G. C. Schatz, and R. P. Van Duyne. Nanosphere lithography: Effect of the external dielectric medium on the surface plasmon resonance spectrum of a periodic array of silver nanoparticles. *Journal of Physical Chemistry B*, 103:9846, 1999.

[126] T. R. Jensen, M. D. Malinsky, C. L. Haynes, and R. P. Van Duyne. Nanosphere lithography: Tuneabel localized surface plasmon resonance spectra of silver nanoparticles. *Journal of Physical Chemistry B*, 104:10549, 2000.

[127] J. Henzie, J. Lee, M. H. Lee, Warefta Hasan, and T. W. Odom. Nanofabrication of plasmonic structures. *Annual Review of Physical Chemistry*, 60:147, 2009.

[128] C. Noguez. Surface plasmons on metal nanoparticles: The influence of shape and physical environment. *The Journal of Physical Chemistry C*, 111:3806–3819, 2007.

[129] N. G. Khlebtsov and L. A. Dykman. Optics and biomedical applicationsof plasmonic nanoparticles. *Journal of Quantitative Spectroscopy & radiative transfer*, 111:1, 2010.

[130] L. Lu, H. Wang, Y. Zhou, S. Xi, H. Zhang, J. Hu, and B. Zhao. Seed-mediated growth of large, monodisperse coreshell goldsilver nanoparticles with ag-like optical properties. *Chemical Communications*, 2:144, 2002.

[131] L. M. Liz-Marzan, M. Giersig, and P. Mulvaney. Synthesis of nanosized gold-silica core-shell particles. *Langmuir*, 12:4329, 1996.

[132] N. Liu, H. Guo, L. Fu, S. Kaiser, H. Schweizer, and H. Giessen. Three-dimensional photonic metamaterials at optical frequencies. *Nature Materials*, 7:31, 2008.

[133] N. Liu, L. Fu, S. Kaiser, H. Schweizer, and H. Giessen. Plasmonic building blocks for magnetic molecules in three-dimensional optical metamaterials. *Advanced Materials*, 20:3859, 2008.

[134] P. Nordlander, C. Oubre, E. Prodan, K. Li, and M. I. Stockman. Plasmon hybridizaton in nanoparticle dimers. *Nano Letters*, 4(5):899, 2004.

[135] H. Rochholz. *Plasmonenresonanzen von sichelförmigen metallischen Nanoobjekten*. PhD thesis, Johannes Gutenberg Universität Mainz, 2005.

List of Figures

List of Tables

Index

Acknowledgments

Curriculum Vitae

Publications

Near-Field-Mediated Enhancement of Two-Photon-Induced Fluorescence on Plasmonic Nanostructures
J. Fischer, N. Bocchio, A. Unger, H.-J. Butt, K. Koynov, and M. Kreiter
Journal of Physical Chemistry C 114, 20968 – 20973 (2010)

Plasmon Hybridization in Stacked Double Crescents Fabricated by Colloidal Lithography
N. Vogel* and J. Fischer*, R. Mohammadi, M. Retsch, H.-J. Butt, K. Landfester, C. Weiss, and M. Kreiter
Nanoletters, accepted

Plasmon Hybridization in Opposing Double Crescents with Tuneable Resonances
J. Fischer* and N. Vogel*, R. Mohammadi, H.-J. Butt, K. Landfester, C. Weiss, and M. Kreiter
in preparation

* Authors contributed equally.